HARVARD UNIVERSITY
Graduate School of Arts and Sciences

DISSERTATION ACCEPTANCE CERTIFICATE

The undersigned, appointed by the

Department of Physics

have examined a dissertation entitled

Interacting quantum materials and their acoustic analogs

presented by Harris Stanley Pirie

candidate for the degree of Doctor of Philosophy and hereby certify that it is worthy of acceptance.

Signature Jennifer Hoffman

Typed name: Professor Jenny Hoffman, Chair

Signature Julia Mundy

Typed name: Professor Julia Mundy

Signature Subir Sachdev

Typed name: Professor Subir Sachdev

Date: December 16, 2021

Interacting quantum materials and their acoustic analogs

A DISSERTATION PRESENTED
BY
HARRIS STANLEY PIRIE
TO
THE DEPARTMENT OF PHYSICS

IN PARTIAL FULFILLMENT OF THE REQUIREMENTS
FOR THE DEGREE OF
DOCTOR OF PHILOSOPHY
IN THE SUBJECT OF
PHYSICS

HARVARD UNIVERSITY
CAMBRIDGE, MASSACHUSETTS
DECEMBER 2021

Thesis advisor: Professor Jennifer E. Hoffman Harris Stanley Pirie

Interacting quantum materials and their acoustic analogs

ABSTRACT

When electrons in solids interact strongly with one another, they often produce unexpected, emergent phases, like high-temperature superconductivity or fractional quantum Hall states. In this thesis, I approach this strongly interacting regime from two directions: by searching for materials with naturally occurring strong interactions, and by developing new strategies to enhance existing interactions.

In the first approach, I focus on lanthanide or actinide metals that host $4f$ or $5f$ magnetic moments, such as SmB_6 or URu_2Si_2. At temperatures of around a few Kelvin, the conduction electrons in these materials coherently screen the magnetic moments, becoming entangled with them. This strong interaction has dramatic consequences. The once-mobile electrons in URu_2Si_2 suddenly struggle to move, appearing as though they have an effective mass nearly a hundred times higher than a free electron does! Whereas in SmB_6, this interaction drives a topological phase transition that yields heavy Dirac states at the material's surface. At milliKelvin temperatures, the interactions between these Dirac states may promote even stranger behavior, like a spontaneously generated quantum anomalous Hall effect, fractionalization, or a phase with non-Abelian quantum statistics. In chapters 1-4 of this thesis, I present the first images of heavy Dirac fermions ever taken, and I describe how atomic-scale defects influence their fate.

In the second approach, I search for ways to decrease an electron's kinetic energy so that its interactions with other electrons play a more prominent role in determining its behavior. One way to slow electrons down is to trap them in certain spatial regions, either by creating a moiré pattern or by using their own destructive wave interference to prevent them from moving away. As it turns out, these methods are just as effective at slowing sound waves as they are at slowing electron waves. A carefully constructed acoustic metamaterial can reshape the flow of sound to closely resemble how electrons move in a solid. Using acoustic metamaterials to mimic electron behavior is certainly appealing: it can take years to find a reliable recipe for growing new quantum materials, whereas a new acoustic metamaterial might take only a few hours to 3D print. In chapters 5-8 of this thesis, I present designs for acoustic metamaterials that exploit topological protection to create a robust logic gate, that mimic generic van der Waals heterostructures, and that can slow sound to a few centimeters per second—only mildly outpacing a garden snail!

If combined, these two approaches could create a platform for engineering designer quantum phases with strong electron interactions, opening a path towards future technology such as custom-built unconventional superconductors, robust quantum computers, and antiferromagnetic spintronic devices for efficient information storage and processing.

Contents

Listing of figures

Citations to previously published work

Chapter 2 appears in its entirety as

[1] Harris Pirie, Yu Liu, Anjan Soumyanarayanan, Pengcheng Chen, Yang He, M. M. Yee, P. F. S. Rosa, J. D. Thompson, Dae-Jeong Kim, Z. Fisk, Xiangfeng Wang, Johnpierre Paglione, Dirk K. Morr, M. H. Hamidian, and Jennifer E. Hoffman, "Imaging emergent heavy Dirac fermions of a topological Kondo insulator." *Nat. Phys.* **16**, 52–56 (2020).

Chapter 3 appears in its entirety as

[2] Christian E. Matt, Harris Pirie, Anjan Soumyanarayanan, Yang He, Michael M. Yee, Pengcheng Chen, Yu Liu, Daniel T. Larson, Wendel S. Paz, J. J. Palacios, M. H. Hamidian, and Jennifer E. Hoffman, "Consistency between ARPES and STM measurements on SmB_6." *Phys. Rev. B* **101** 085142 (2020).

Chapter 4 is based largely on the following preprint

[3] Harris Pirie, Eric Mascot, Christian E. Matt, Yu Liu, Pengcheng Chen, M. H. Hamidian, Shanta Saha, Xiangfeng Wang, Johnpierre Paglione, Graeme Luke, Cyrus Hirjibehedin, J. C. Séamus Davis, Dirk K. Morr, and Jennifer E. Hoffman, "Visualizing the charge puddles around Kondo holes" (in preparation)

Chapter 6 appears in its entirety as

[4] Harris Pirie, Shuvom Sadhuka, Jennifer Wang, Radu Andrei, and Jennifer E. Hoffman, "Topological Phononic Logic" *Phys. Rev. Lett.* **128** 105501 (2022)

Chapter 7 appears in its entirety as

[5] William Dorrell, Harris Pirie, S. Minhal Gardezi, Nathan C. Drucker, and Jennifer E. Hoffman, "van der Waals metamaterials" *Phys. Rev. B* **101** 121103(R) (2020).

Chapter 8 appears in its entirety as

[6] S. Minhal Gardezi, Harris Pirie, Stephen Carr, William Dorrell, and Jennifer E. Hoffman, "Simulating twistronics in acoustic metmaterials" *2D Mater.* **8** 031002 (2021). © IOP Publishing. Reproduced with permission. All rights reserved.

Acknowledgments

My journey through graduate school has been shaped by the people around me. This thesis would not have been possible without their support, enthusiasm, and frankly, hard work.

First of all, I'd like to thank my family for their love and support, particularly during the last two years while I tried to run a scanning tunneling microscope from the other side of the world. My time at Harvard had many ups and downs, but I was lucky to have friends who found a way to make it fun in either case. I'm especially grateful to Keith Krenek and Ciarán O'Neill, who were additionally very good at spotting which of my crazy ideas might actually work. And to Luca Matrà, Emma Thomas, Ben Weidmann, and Kristen Hunter, who all helped me become a better scientist.

At Harvard, I benefited from being part of an open, inquisitive, and friendly lab. Thanks to all who made it such a wonderful place to be. In particular, I'm grateful to Mohammad Hamidian for patiently guiding me through my early data analysis and for introducing me to the STM world; to Tatiana Webb, for teaching me how to stay calm and move forward, even when the walker got really stuck; to Christian Matt, for his enthusiasm, hard work, and unfailing humor; to Richard Liu, for patiently fixing and running everything, especially during these last two years; and to Ben November, for navigating the metamaterials team towards an exciting future. I learned a lot about

STM and MBE from Dennis Huang, Yang He, Jason Hoffman, Maoz Ovadia, Eddie Ji, Jian-Feng Ge, and Pengcheng Chen. Some of the data in this thesis was taken by Anjan Soumyanarayanan, Yang He, and Michael Yee. In addition, I've enjoyed working alongside Dilek Yildiz, Wan-Ting Liao, Alyson Spitzig, Nathan Drucker, Larissa Little, Ruizhe Kang, Kevin Hauser, and Aaron Coe.

Some of my most-rewarding moments at Harvard have come from mentoring undergraduate research projects. I was lucky to work with such talented students, many of whom are now in graduate school themselves. I am especially grateful to Shuvom Sadhuka, whose high school project launched our metamaterials work; Jennifer Wang, whose 100 page/week lab notebooks were downright frightening; William Dorrell, who broke down an ambitious goal and then conquered it; Minhal Gardezi, who wrote an incredible pedagogical thesis; Albert Chien, who drove to Ithaca and back to get data; and Bryce Primavera, who started it all. I've also enjoyed working with Radu Andrei, Fan Du, Walker Gillett, Piper Wysocki, Jiatong Yang, Jeffery Shi, Xirui Wang, Jonathan Goettsch, and Kevin Chen.

I have been fortunate to have collaborated with many brilliant scientists, both at Harvard and beyond. I am especially grateful to Dirk Morr, who has always treated me as an *ad hoc* member of his group at UIC, and to his student Eric Mascot who happily and patiently walked me through many of their theoretical tools. I'd also like to thank Cyrus Hirjibehedin for his guidance and enthusiasm along the way. This thesis features data taken in Séamus Davis' lab, who also provided sound advice on several occasions. The SmB_6 and URu_2Si_2 samples were grown and characterized by the groups of Johnpierre Paglione, Zach Fisk, Priscila Rosa, Joe Thompson, and Graeme Luke. Much of the part on acoustic metamaterials grew out of conversations with Stephen Carr, Alex Kruchkov, Clayton DeVault, Haoning Tang, Katia Bertoldi, Ari Turner, and Eric Mazur.

I'm thankful to many staff in the Physics Department, but especially to Jacob Barandes and Lisa Cacciabaudo, who made me feel welcome and were always there to help. Also to Silke Exner, Barbara Drauschke, Dionne Clarke, and Erica Mantone who made the PhD program easy to navigate.

Finally, I'd like to thank my thesis committee, Subir Sachdev and Julia Mundy, for their support, encouragement, and advice, especially over the last year when my results weren't adding up. Most of all, I'd like to thank my advisor Jennifer Hoffman, for believing in me from the very beginning, for never giving up when things got hard, and for always caring about the people involved. I learned a lot of science from Jenny, but also a lot about how to communicate it to a broad audience and to engage others. I am grateful to have had such a kind and enthusiastic mentor to help me forge what's been a rewarding, yet admittedly unusual, path through graduate school. My time at Harvard could not have been more well spent.

Part I

Unearthing strong interactions

1

Interacting quantum materials

THE ADVENT OF QUANTUM MATERIALS—materials in which the effects of quantum mechanics cannot be ignored—is poised to combat pressing global challenges in energy efficiency and the stagnation of silicon-based electronics. For instance, recently discovered interface-enhanced superconductors provide a new path for low-loss electronics that would greatly reduce power consumption [7, 8]. At the same time, topological superconductors that host non-Abelian quasiparticles may permit fault-tolerant quantum computation [9–11], a revolutionary computing paradigm that may be just around the corner [12]. Harnessing the full potential of quantum materials requires unearthing new systems where topologically protected quasiparticles interact strongly with each other.

1.1 The synergy between interactions and topology

Since the 1950s, lanthanide and actinide metals that host a dense lattice of 4*f* or 5*f* moments have been a fruitful platform to unearth novel interacting quantum states. In these systems, the competition between antiferromagnetic ordering of the local *f* moments and their screening by conduction electrons leads to a rich phase diagram exhibiting quantum criticality [13], unconventional superconductivity [14], and heavy fermions [15, 16]—quasiparticles with effective masses thousands of times that of a bare electron. These heavy fermions appear at low temperatures when the magnetic moments are screened by the formation of a coherent spin-zero many-body ground state, in which the *f*-electron character is entangled with the itinerant carriers (see Fig. 1.1(a)). This phase is characterized by an hybridization gap in the quasiparticle spectrum, leading to an interaction-driven insulating phase if the gap encompasses the Fermi level, called a Kondo insulator (Fig. 1.1(b)). But these Kondo insulators are far stranger than their non-interacting counterparts. Recent experiments repeatedly indicate some form of remnant metallicity in Kondo insulators [17–21], even as the resistance simultaneously diverges [22]. This disparity prompted many intriguing proposals—some that predict exotic new phases [23–26] and some that implicate defects [27–30]. One thing has remained clear throughout this debate: the strongly interacting regime is full of surprises.

The discovery of topological insulators in the last decade has broadened the horizons for new quantum materials, and fundamentally altered the way they are characterized. Rather than relying on Landau's paradigm of broken symmetries to define phases of matter, a topological index keeps track of the ordering of a material's energy bands [31]. In the bulk, materials with inverted ordering

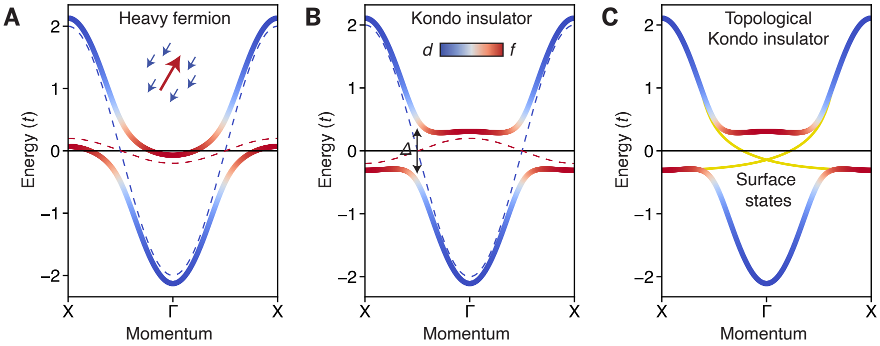

Figure 1.1: Band structures in a Kondo lattice (**A**) The interaction between local *f* moments (red arrow and dashed line) and itinerant conduction electrons (blue) creates a lattice of screened Kondo singlets (inset), leaving behind a heavy-fermion metal with mixed character (solid lines). (**B**) In certain cases, this interaction can open a gap Δ at the chemical potential, driving the system into an insulating phase. (**C**) If this insulating gap encodes a non-trivial topology, heavy Dirac states (yellow) will form at the material's surface.

are indistinguishable from those with normal ordering. But their topology forces the band inversion to unwind at the material's surface, spawning emergent Dirac states that allow dissipationless charge and spin transport (see Fig. 1.1 (c)). However, *a priori*, electron-electron interactions in these systems are too weak to produce the full range of extraordinary phases expected from the topological knotting of quantum-mechanical states. Recent theoretical work is driving in a new direction [32–34], predicting materials whose strong electron interactions spontaneously generate topological phases hosting quasiparticles with fractional spin and charge [35], or with non-Abelian exchange statistics [36, 37], all of which remain undiscovered. Many of the leading platforms for universal topological quantum computation require these novel elements [9], making the search for interacting topological matter not just one of fundamental importance but also paramount for technological innovation.

1.2 EMERGENT MYSTERIES IN SmB$_6$

In the last several years, the search for interacting topological materials has sharply focused on the compound SmB$_6$. In its proposed topological Kondo insulator phase, emergent conducting surface states entangle with interacting *f* electrons [32, 38, 39]. This process is predicted to generate the highest known density of Dirac fermions, with effective masses several orders of magnitudes larger than those in any other system. As a consequence, a strongly interacting liquid of heavy Dirac fermions should form at the surface, capable of harboring exotic topological phases distinct from the bulk [40]. The direct observation of these heavy Dirac states would constitute the discovery of an interaction-driven topological phase whose potential for application is magnified by its accessibility at a material's surface and by its placement at the chemical potential.

Early indications of conducting surface states in SmB_6 were quickly discovered via geometry-dependent transport measurements [41–44]. However, follow-up measurements using either angle-resolved photoemission (ARPES) [45–52], or the de Haas van Alphen (dHvA) effect [19, 53, 54] neither agreed with each other, nor matched the theory. A key difficulty in accurately detecting the topological state in SmB_6 is the quality of the surface, which lacks a natural cleavage plane [55]. In fact, domains of any ordered termination rarely exceed a few tens of nanometers, far smaller than the typical photoemission spot size of a few hundred microns. Accordingly, ARPES measurements average intensity from several polar and non-polar terminations, presumably blurring spectral features that are shifted in energy by polarity-driven band bending. Meanwhile, the three dHvA experiments all interpreted their quantum oscillations differently, claiming they come from either a Dirac surface state two orders of magnitude lighter than theoretical predictions [53], an exotic bulk Fermi surface [19], or aluminum inclusions [54]. The gross discrepancies cast doubt on all these claims; meanwhile the predicted strongly interacting topological surface state remains hidden.

The remainder of this part of the thesis is organized as follows. In chapter 2, I present the first direct observation of the full momentum-space structure of three flatly dispersing Dirac surface bands in SmB_6 with effective masses reaching $410 \pm 20 m_e$ (where m_e is the bare electron mass). In chapter 3, I reconcile the discrepancy between these heavy Dirac states and the light ones measured by ARPES by accounting for polarity-driven band bending on a mixed termination. In chapter 4, I develop a new technique to visualize charge at atomic length scales. This technique reveals metallic puddles around three common defects in SmB_6, with characteristics that match the mysterious 3D Fermi surface seen in dHvA measurements.

This chapter appears as:

Nat. Phys. **16**, *52–56 (2020)*

Harris Pirie, et al.

2

Imaging emergent heavy Dirac fermions of a topological Kondo insulator

The interplay between strong electron interactions and band topology is a new frontier in the search for exotic quantum phases. The Kondo insulator SmB_6 has emerged as a promising platform as its correlation-driven bulk gap is predicted to host topological surface modes entangled with *f* electrons, spawning heavy Dirac fermions [32, 38, 39, 56]. Unlike the conventional surface states of non-interacting topological insulators, heavy Dirac fermions are expected to harbor spontaneously generated quantum anomalous Hall states [40], non-Abelian quantum statistics [36, 37], fractionalization [35], and topological order [35–37]. However, the small energy scales required to probe heavy Dirac fermions have complicated their experimental realization. Here we use high-energy-resolution spectroscopic imaging in real and momentum space on SmB_6. On cooling through 35 K, we observe the opening of an insulating gap that expands to 14 meV at 2 K. Within the gap, we image the formation of linearly dispersing surface states with effective masses reaching $410 \pm 20\ m_e$. Our results demonstrate the presence of correlation-driven heavy surface states in SmB_6, in agreement with theoretical predictions [32, 38, 39, 56]. Their high effective mass translates to a large density of states near zero energy, which magnifies their susceptibility to the anticipated novel orders, and their potential utility.

2.1 A CORRELATION-DRIVEN TOPOLOGICAL INSULATOR

Kondo insulators (KI) are formed when strong interactions within a periodic array of localized moments, usually *f*-electrons, lead to reorganization of the low temperature electronic structure [34]. This process opens an insulating gap Δ, driven by hybridization between renormalized, low-lying localized states and itinerant conduction electrons (Figs. 2.1A-B). The KI SmB_6, in which localized *f* and itinerant *d* states are contributed by Sm atoms (Fig. 2.1A inset), exhibits such a characteristic metal-insulator crossover at $T_{MI} \approx$ 30-50 K [57, 58]. Mysteriously, the resistance plateaus below 5 K [57, 58], signaling the onset of a new conduction channel whose origin has been intensely debated for decades [34]. One resolution to this long-standing problem posits that SmB_6 hosts a novel *topological Kondo insulator* (TKI) ground state [32, 38, 39, 56], whose low temperature conductivity originates from topologically emergent Dirac surface states within the narrow energy window of the

KI gap. Large *f*-electron contributions to these states are predicted to yield the heaviest Dirac states of any known material.

Electronic structure calculations predict SmB_6 to be a TKI [38, 39, 56]. The expected bulk band structure of the associated Kondo lattice model contains two crystal-field-split *f* states and a band of *d* electrons (Figs. 2.1A,B). Quantum mechanical mixing between opposite parity *f* and *d* states vanishes at the high symmetry points $\mathbf{k}^* = \Gamma, X, M, R$ where parity is a good quantum number, thus forcing nodes in the hybridization matrix element, $\langle f| V(\mathbf{k}^*) |d\rangle = 0$ (Fig. 2.1C). Consequently, the parity $\delta(\mathbf{k})$ of the fully hybridized filled states is inverted at three symmetry-equivalent X points in the 3D cubic Brillouin zone. The resulting topological invariant predicts a non-trivial topological phase [32, 56], captured by the index $\nu = \delta_\Gamma \delta_R (\delta_X \delta_M)^3 = -1$, where $\delta_{\Gamma,X,M,R} = \pm 1$ is the parity of filled bands at high symmetry points (red circles Fig. 2.1D). On the SmB_6 Kondo lattice, topologically emergent surface states are predicted to i) lie predominantly within the energy interval of the correlation-driven bulk gap, ii) have a Dirac spectrum, iii) be centered at the $\bar{\Gamma}$ and two $\bar{X}$-points of the 2D surface Brillouin zone, and iv) have distinct band velocities. The last prediction follows intuitively from observing that 3D constant-energy manifolds at the X-points with different relative orientations create inequivalent 2D projections (Fig. 2.1D). Consequently, surface states connecting 2D-projected bulk hybridized bands are expected to have distinct velocities at the $\bar{\Gamma}$ and $\bar{X}$-points (Fig. 2.1D).

Experimentally, temperature-dependent point-contact spectroscopy [42] has shown the SmB_6 bulk electronic structure to be consistent with a KI, while surface conduction channels have been demonstrated by geometry-dependent transport measurements at low temperatures [44, 58]. Magnetothermoelectric studies [59] imply that the (110) surface of SmB_6 may harbor heavy metallic surface states, though their topological nature is not clear. On the other hand, torque magnetometry experiments [53] on the (110) surface measured surface states whose velocities are more than two orders of magnitude larger than expected [39]. In contrast, a separate quantum oscillation mea-

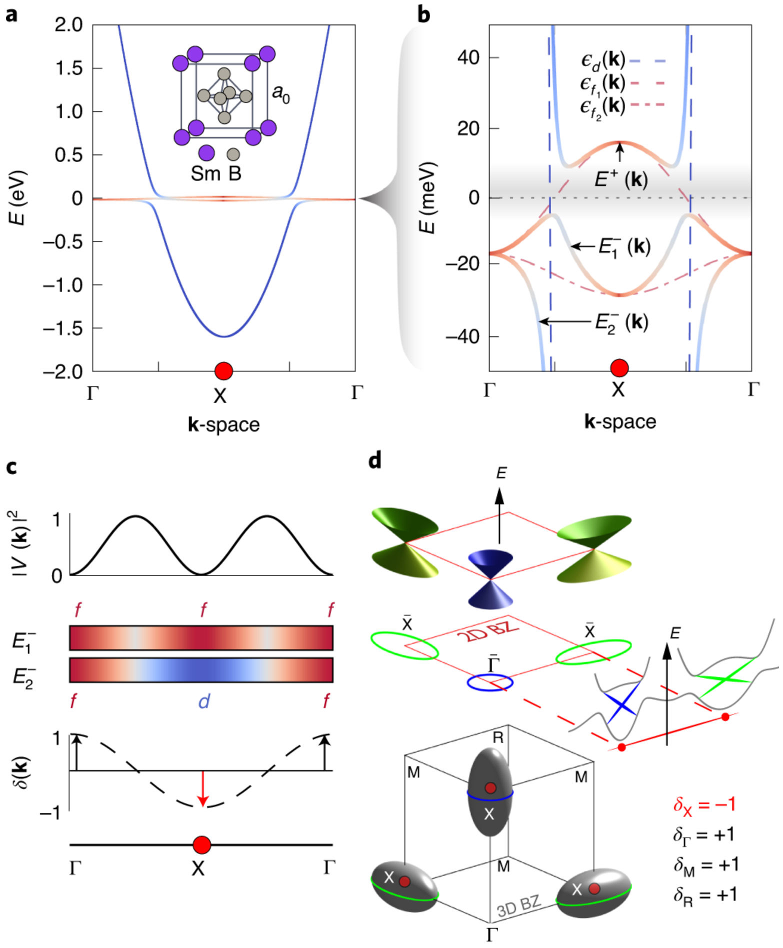

Figure 2.1: **Anticipated topological Kondo insulator electronic structure of SmB$_6$.** (**A**) The Kondo insulator (KI) electronic structure consists of an itinerant d-character band (blue), centered around the X point, which hybridizes with localized f-character (red) states. Both f and d states are contributed by the Sm atoms, which form a cubic unit cell (inset). (**B**) Narrow energy window of the same electronic structure in (A). At low temperatures a d-band (ε_d) and two closely spaced crystal-field-split f-states (ε_{f_1}, ε_{f_2}) hybridize to form three separate bands (E^+, E_1^-, E_2^-) with a gap of several meV. (**C**) The topological invariant for the KI electronic structure is calculated from a product of parity eigenvalues, which are opposite for d and f states. Top: Nodes in the hybridization parameter, $|V(\mathbf{k})|^2$, at the X and Γ points lead to pure f or d character of the hybridized bands at those locations. Middle: The filled bands, E_1^-, E_2^- have full f character at Γ and evolve to either d or f at X. Bottom: Thus, total parity, δ, is reversed only at the X points (marked red circle). (**D**) The cubic topological Kondo insulator (TKI) electronic structure has parity inversion at three X points (red balls) in the 3D Brillouin zone giving a Z_2 topological index $\nu = \delta_\Gamma \delta_R (\delta_X \delta_M)^3 = -1$ that encodes the strong topological state. When projected onto the 2D Brillouin zone, the inversion manifests at the $\bar{\Gamma}$ and two $\bar{X}$ points (red circles) and consequently sets the locations of the predicted 2D Dirac states. These Dirac surface states acquire different velocities from the inequivalent projections of the bulk elliptical constant-energy contours onto the 2D surface Brillouin zone (green ellipses and blue circle).

surement attributed these states to the bulk [19]. Direct energy- and momentum-resolved electronic structure mapping by angle-resolved photoemission spectroscopy (ARPES) [47–49] appeared to show linearly dispersing surface bands with velocities at least an order of magnitude larger than those expected for the Dirac fermions of SmB_6 and with an inferred Dirac point buried far below the bulk gap [39] (Supplementary Table 2 [60]). Because much of the active physics in the ground state resides within a small energy window set by the KI gap, $\Delta \approx$ 8-10 meV, as revealed by transport experiments [44, 61], ARPES mapping of the electronic structure is limited in detecting narrow bandwidth states of a incipient TKI [50]. Furthermore, ARPES measurements typically average over different (polar) surface terminations with relative intensity and chemical potential shifts in their surface states, rendering interpretations difficult [2, 52]. Collectively, these suggestive but controversial experiments have renewed the urgency to discover topological states arising from strong electronic interactions. Ultimately, observation of strongly correlated topological states in SmB_6 requires measurements on a uniform and ordered surface termination, access to filled and empty states at low temperatures, and meV energy resolution in momentum space to disentangle the shallow dispersions of a bulk KI band structure (Fig. 2.1B) and surface heavy Dirac fermions (Fig. 2.1D).

Here we use spectroscopic scanning tunneling microscopy (STM) to directly map the structure and formation of heavy Dirac states on the (001) surface of SmB_6 in two complementary measurements. First, we resolve the energy- and momentum-space structure of two inequivalent Dirac cones from quasiparticle interference (QPI) patterns around atomic defects by measuring spatially resolved differential conductance, $dI/dV(\mathbf{r}, E = eV) \equiv g(\mathbf{r}, E)$. Second, we track the formation of heavy Dirac states from their additional contributions the low-temperature point spectroscopy by measuring $g(E, T)$. We find that their onset is far more abrupt than expected from thermal broadening; instead, it is correlated with the development of the bulk KI. Our measurements corroborate one another by each detecting a consistent Dirac-point energy of $E_D \approx -5$ meV.

2.2 Imaging quasiparticle interference

We studied nominally pure, 0.1% Gd-doped, and 0.5% Fe-doped SmB_6 by cleaving single crystals in cryogenic ultra-high vacuum and directly inserting into the STM at 4 K (see Methods). We found that adding a small amount of Gd or Fe dopants enhanced quasiparticle scattering, but our observed QPI dispersions were consistent across all samples. We focused on regions where exactly half of the atoms remain on the cleaved surface, resulting in an ordered (2×1) reconstruction (Fig. 2.2A) [62, 63]. We identify this surface as a half-Sm termination because intentional Fe dopants, which substitute for Sm, appeared at the lattice sites. A half-Sm termination is beneficial because it is non-polar, eliminating the possibility of polarity-driven surface states [51]. Furthermore, the (2×1) reconstruction increases our sensitivity to one of the $\bar{X}$-point Dirac cones by folding it to the $\bar{\Gamma}$ point (Fig. 2.2B), where it has a longer vacuum decay length due to its lower in-plane momentum [64].

We detected clear interference patterns in raw $g(\mathbf{r}, E)$ around defects, caused by the elastic scattering of quasiparticles, as shown in Figs. 2.2C,D. Their energy-dependent wavevector, $\mathbf{q}(E) = \mathbf{k}_f(E) - \mathbf{k}_i(E)$, encodes the momentum transfer between initial $(\mathbf{k}_i)$ and final $(\mathbf{k}_f)$ states and tracks the underlying electronic structure [65–67]. In SmB_6, QPI patterns are typically short-ranged around defects, as in Fig. 2.2D, reflecting contributions from localized f electrons. Correspondingly, they manifest as fairly broad peaks in the Fourier-transformed differential conductance, $|\tilde{g}(\mathbf{q}, E)|$, with highest signal-to-noise along the q_y direction (Fig. 2.2E), primarily due to the anisotropy of the scattering form factor (see Supplementary Section V [60]). We quantified their wavevector by fitting angle-averaged linecuts of $|\tilde{g}(\mathbf{q}, E)|$ along q_y with a set of Gaussians (Fig. 2.2F, details in Supplementary Section IV [60]). The QPI wavevector changes rapidly with energy, as shown in Fig. 2.3, but can be broadly divided into two energy ranges. For energies within the KI gap Δ, there are two sets of roughly linear dispersions: one very shallow (green guides in Fig. 2.3), and one steep (blue guides). For energies outside this range, the set of dispersions can be mapped to the known low-

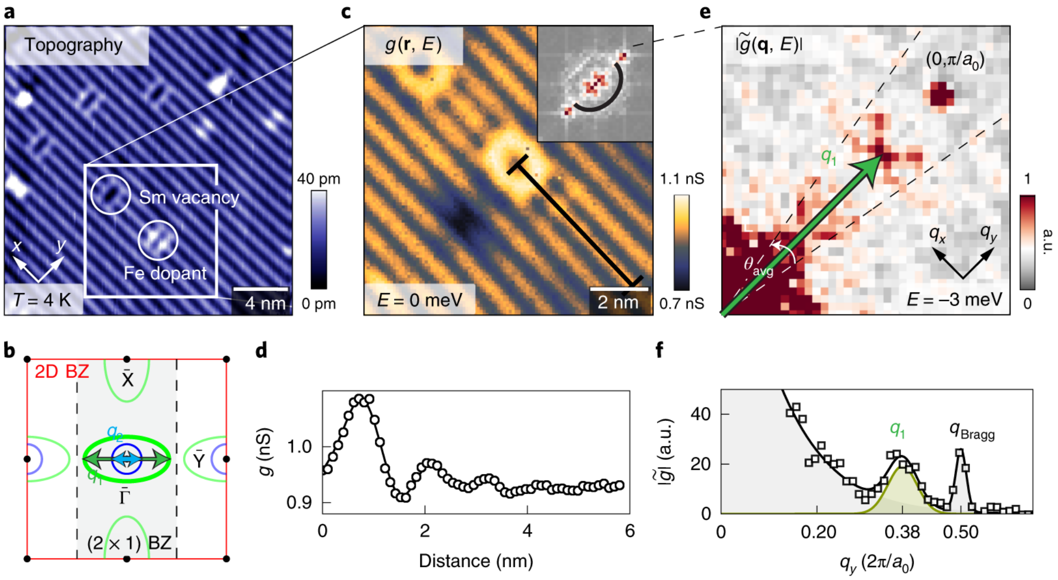

Figure 2.2: Imaging quasiparticle interference (QPI) on the (2×1) surface of SmB$_6$. (**A**) A (2×1) surface reconstruction on the half-Sm termination of SmB$_6$ doubles the unit cell in the y direction, creating the rows of atoms shown in the topographic image (sample bias $V_s = -100$ mV, current set point $I_s = 50$ pA). (**B**) Correspondingly, the surface Brillouin zone is halved along k_y, folding the $\bar{Y}$-point Dirac cone to $\bar{\Gamma}$. (**C**) Atomic defects on the surface scatter momentum eigenstates to generate QPI patterns in the spatially resolved differential conductance, $g(\mathbf{r}, E = 0$ meV$)$, measured in the boxed area in (A) ($V_s = -100$ mV, $I_s = 150$ pA). In this region, QPI appears as a ring in the Fourier transform (FT) of differential conductance, $|\tilde{g}(\mathbf{q}, E)|$ (green line in inset). (**D**) The QPI is short ranged around defects, reflecting contributions from localized f states; it decays after a few periods in this linecut along the black line in (C). (**E**) In a larger 30-nm area, the QPI signal in $|\tilde{g}(\mathbf{q}, E = -3$ meV$)|$ manifests as a broad peak with highest signal-to-noise along q_y ($V_s = 30$ mV, $I_s = 180$ pA). At this energy, it occurs at the q_y vector corresponding to intra-cone backscattering within the $\bar{X}$-point Dirac cone (labelled q_1 in (B)). The image has been two-fold symmetrized to increase signal-to-noise. (**F**) We quantified QPI peaks by fitting θ-averaged linecuts of $|\tilde{g}(\mathbf{q}, E)|$ along q_y to a sum of Gaussians that capture contributions from the Bragg peak, low-$\mathbf{q}$ disorder and dispersing QPI (green peak labelled q_1).

energy Kondo insulator states of SmB$_6$ (details in Supplementary Section VIII [60]). None of these dispersions were noticeably affected by magnetic fields up to 9 T (compare Fig. 2.3A-B), consistent with previous STM spectra [68] (see Supplementary Section VI [60]). All dispersions were reproducible in six different raw datasets, on three distinct samples, from two different growers, with distinct STM acquisition parameters, three of which are shown in Fig. 2.3.

The in-gap states we image are in excellent agreement with expectations for a TKI phase with f-dominated heavy Dirac fermions [38, 39, 56]. Their dispersions, overlaid on Figs. 2.3A,C, match

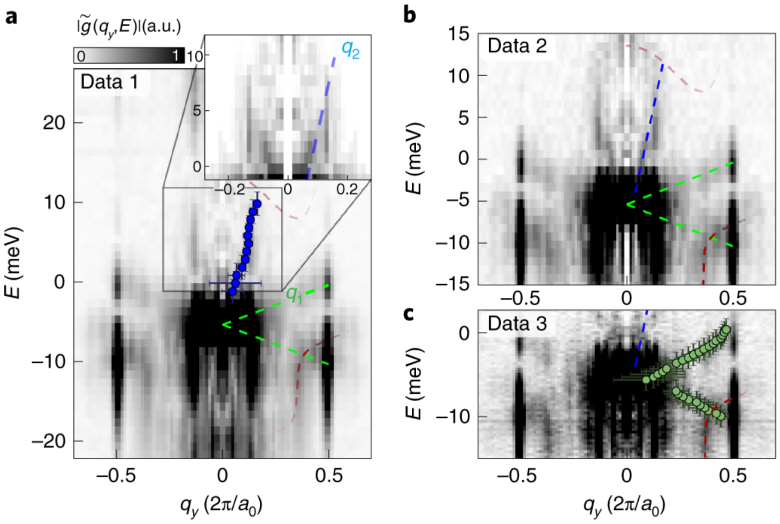

Figure 2.3: **Raw QPI is consistent in three different sample areas.** (**A-C**) θ-averaged linecuts along q_y of $|\tilde{g}(\mathbf{q},E)|$ on three different sample areas give consistent results. In each case, dispersing QPI signals are marked by dashed guides: green (labelled q_1) and blue (q_2) lines track surface states, while the red guides track KI states. A box-windowed FT (zoomed inset in (C)) enhances the low-$\mathbf{q}$ signal (blue) compared to the Hanning-windowed FT that reduces spread of the high-$\mathbf{q}$ states in the main panel. The $\mathbf{q}$-axis error bars are estimates based on the covariance matrix of the Gaussian fits, whereas the E-axis error bars show the energy resolution of the STM. Data in (A) and (C) have $B = 0$ T, and (B) has $B = 9$ T, which does not noticeably affect the QPI. All other data acquisition parameters are listed in Table SI.

the two sets of linear traces expected from scattering within distinct Dirac cones, (labelled q_1 and q_2 in Fig. 2.2B): their average nodal point energies $E_D = -5 \pm 1$ meV, lie within the KI gap, and their distinct velocities, $v_{\bar{X}} \approx 1150 \pm 40$ m/s and $v_{\bar{\Gamma}} \approx 14000 \pm 1000$ m/s, identify them as Dirac states positioned at the $\bar{X}$-point and the $\bar{\Gamma}$-point, respectively (Fig. 2.1D). The largest effective Dirac mass [34] is at the $\bar{X}$ point with $m^* = \hbar k_F / v_{D_{\bar{X}}} = (410 \pm 20) m_e$. Additionally, the size of each Fermi pocket along q_y is in excellent agreement with ARPES measurements of k_F [47, 49]. Meanwhile, the apparent discrepancies between our measured velocities and Dirac points, and those of ARPES, can be explained by the fact that we access a single, non-polar surface, whereas ARPES experiments typically average over a mixture of terminations [2].

Intra-cone backscattering, illustrated in Fig. 2.2B, is the simplest identifiable process responsible for the observed Dirac-state QPI. We adduce that the scattering vector $\mathbf{q}(E_F) = 2\mathbf{k}(E_F)$ is in good agreement with the size of surface state Fermi pockets in electronic structure calculations [39]. Yet, the observation of backscattering is unusual, because in the simplest model for topological surface states, whereby Dirac cones have an in-plane helical spin structure, neither magnetic nor non-magnetic backscattering leads to a peak in the QPI spectrum [69]. On the other hand, introducing even weak out-of-plane ferromagnetic correlations immediately restores the backscattering peak for magnetic defects, while preserving the Dirac cone structure (see Supplementary Section III [60]). Such ferromagnetic canting can occur due to the Dzyaloshinski-Moriya interaction, the local spin polarization induced by magnetic defects [70], or in topological insulators with strong interactions, such as TKIs, where it was shown theoretically that surface states possess an out-of-plane spin polarization [40, 71]. As it turns out, hysteresis associated with surface ferromagnetism was recently observed in SmB_6 at low temperature [72]. In addition, we found that a small inclusion of nominally non-magnetic Sm-vacancies leads to an enhanced magnetic susceptibility at low temperatures, akin to the addition of Kondo holes [73] (see also Supplementary Section III [60]). In fact, the combination of magnetic defects and local ferromagnetic correlations was also proposed as the origin of the backscattering QPI signal recently measured in magnetically doped topological insulators [74].

2.3 The formation of heavy Dirac states

To associate the Dirac states detected from QPI with a TKI phase, we also tracked their temperature dependence in point spectra, $g(E, T)$. Unlike trivial surface states, the formation of heavy Dirac fermions at the surface of a TKI is predicated on the coherence of the correlation-driven KI gap. With increasing temperature, incoherent Kondo lattice states spread into this gap as the hybridization between f and d electrons unwinds. Eventually, this process is expected to drive a topological phase transition as band-parity inversion is lost, eliminating the non-trivial surface states. However, theory has not yet succeeded to describe coherent Kondo lattice evolution, much less the concomitant formation of heavy Dirac fermions. Here, we experimentally extract this complex connection by tracking the simultaneous temperature evolution of the KI gap and Dirac surface state contributions to $g(E)$. In general, $g(E)$ cannot be directly interpreted as density of states in multi-orbital Kondo lattice systems due to the quantum interference between electrons co-tunneling into f and d states [75, 76]. We account for this effect by modeling the differential conductance spectrum as

$$g(\mathbf{r}_0, E) \propto \left[\mathbf{t}^T \mathrm{Im} G(\mathbf{r} - \mathbf{r}_0 = 0, E)\mathbf{t}\right], \quad \mathbf{t}^T = [t_d \; t_{f_1} \; t_{f_2}], \tag{2.1}$$

where t_α represents tunneling probabilities into the individual orbital states and $G(\mathbf{r}, E)$ is the Fourier transform of $\widetilde{G}(\mathbf{k}, E)$, the renormalized KI Green's function describing a tight-binding Hamiltonian that qualitatively reproduces known bulk bands [39] (see also Supplementary Section VIII [60]). Eqn. 2.1 includes contributions only from the underlying KI, but not from emergent topological surface states. Even so, it accurately captures all features in $g(E)$ at 15 K (Fig. 2.4A), implying that surface states are negligible at this temperature. Fits to Eqn. 2.1 can be further decomposed into interference terms and the bulk density of states, $D(E)$, weighted by the relative tunneling probabilities (inset to Fig. 2.4A). As temperature is lowered, $D(E, T)$ exhibits a narrow energy window of diminished spectral weight that onsets below $T^*_\Delta \approx 35$ K and expands to $\Delta \approx 14$ meV at low temperatures (Fig. 2.4B), in correspondence with bulk measurements of the KI gap in SmB_6 [42, 44, 57, 58].

The heavy Dirac surface states in SmB_6 emerge only at low temperatures as the KI gap becomes coherent. They are visible in our measurements of $g(E)$ at 2 K as an additional contribution within the KI gap that is not captured by Eqn. 2.1 (see arrow in Fig. 2.4A). The differences between $g(E)$ and fits to Eqn. 2.1 are characteristic of linear bands with a crossing point near -5 meV (Fig. 2.4C), which perfectly matches our independent QPI measurements of heavy Dirac surface states (Fig. 2.3).

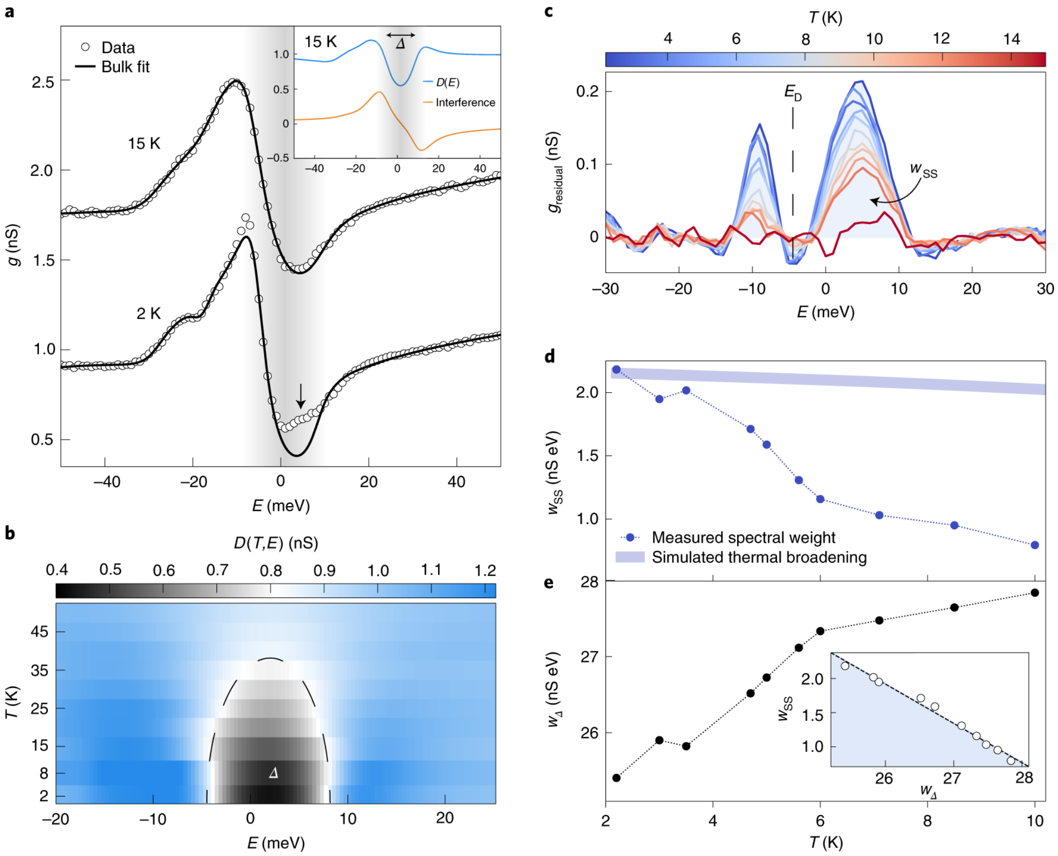

Figure 2.4: **Concomitant evolution of Dirac states and KI gap.** (**A**) Quantum mechanical interference of electrons tunneling from the tip to either d or f states in the SmB$_6$ Kondo lattice leads to a characteristic peak-dip lineshape in $g(E)$ data (open circles). At 15 K, the data is well described by a co-tunneling model (Eqn. 2.1, black line), allowing bulk KI state contributions ($D(E)$, blue line in inset) to be disentangled from interference effects (orange). Yet at 2 K, the fit deviates for energies within the KI gap (grey region), signaling the onset of an additional conductance channel (surface states, arrow) not captured in our bulk KI model. (**B**) The temperature evolution of KI states, $D(E)$, from fitting $g(E, T)$ to a co-tunneling model (see blue curve in (A)). The KI gap Δ onsets below $T^*_\Delta \approx 35$ K and reaches $\Delta \approx 14$ meV at 2 K. (**C**) The deviations of $g(E)$ from the co-tunneling model intensify with lowering temperature. They are characteristic of a linear band dispersion with a nodal energy of -5 meV, and match our independent raw QPI measurements of Dirac surface states (see Fig. 2.3). (**D**) The rapid onset of the Dirac surface states, captured from integrating the fit residuals in (C) (w_{SS}, blue dots), cannot be explained by thermal broadening (thick blue line, see Supplementary Section X [60]). (**E**) Instead, it is correlated with the development of the bulk KI gap, calculated by integrating $D(E)$ for energies within Δ, demonstrating the direct relationship between the evolving host insulator and its topologically emergent states (see inset).

Similar temperature-dependent features in $g(E)$ point spectra have also been observed on the (1×1) boron termination [68]. We quantified the emergence of the surface states by integrating $g_{\text{residual}}(E)$

at each temperature (Fig. 2.4D). We found that the surface states diminish rapidly with increasing temperature, faster than can be accounted for by thermal broadening alone (blue line in Fig. 2.4D), and indeed faster even than the filling of the insulating gap at around 35 K where the topology of the bands is inverted. One possible explanation for this fast decay is that the surface states are reliant on bulk coherence. Certainly, the evolution of their spectral weight is correlated with the weight of residual states in the KI gap, calculated by integrating $D(E)$ for energies within Δ (Fig. 2.4E). Alternatively, the unusually fast decay of the surface states may reflect their interactions with magnetic correlations generated by Kondo lattice defects [58, 77].

Our simultaneous imaging of Kondo insulator formation and slow in-gap surface modes is consistent with SmB_6 hosting a correlation-driven topological surface state that harbors the heaviest known Dirac fermions. The optimal positioning of the *f*-character surface states at the chemical potential, enforced by Kondo lattice interactions, increases prospects for interface engineering to discover novel forms of topological superconductivity and construct transformative quantum devices. SmB_6 and prospective TKIs may become leading testbeds for fractional and non-Abelian statistics, both of which are essential elements of prospective universal topological quantum computation.

2.4 METHODS

STM experiments were carried out on single crystals of pure, 0.1% Gd-doped, and 0.5% Fe-doped SmB_6 grown using the Al-flux method [43]. Crystals were cleaved in cryogenic ultrahigh vacuum (UHV) at $\sim$ 30K and immediately inserted into our home-built STM. STM tips were cut from PtIr wire and cleaned by *in-situ* field emission on Au foil. The cryogenic UHV environment allowed the cleaved surface to stay clean for several months. Data were collected on three different samples and multiple fields of view.

Magnetic susceptibility measurements were performed on single crystalline samples of SmB_6 and

$Sm_{0.95}B_6$ grown by the Al-flux technique with starting composition Sm:B:Al $= 1 - x : 6 : 700$ ($x = 0.0$ and 0.05, respectively). The mixture of Samarium pieces, Boron powder (99.99%) and Aluminum shots (99.999%) was placed in an alumina crucible and loaded in a vertical tube furnace with ultra high-purity Ar flow. The furnace was heated to 1450°C for 12 h followed by slow cooling to 1050°C at 2°C/h. At 1050°C the furnace was shut down, and the flux was removed at room temperature by etching with a NaOH solution. The atomic structure of the resulting single crystals was verified by X-ray diffraction at room temperature in a Bruker D8 Venture diffractometer using a Mo $K\alpha$ X-ray source. A Quantum Design superconducting quantum interference device was used to measure the magnetic response of the crystals to a magnetic field of 1 kOe. The magnetic susceptibility curves were normalized to their values at 350K because of the uncertainty in the determination of the actual number of Sm vacancies.

This chapter appears as:

Phys. Rev. B **101** *085142 (2020)*.

C. E. Matt, Harris Pirie, et al.

3

Consistency between ARPES and STM measurements on SmB_6

The Kondo insulator SmB_6 has emerged as a primary candidate for exotic quantum phases, due to the predicted formation of strongly-correlated, low-velocity topological surface states, and corresponding high Fermi-level density of states. However, measurements of the surface-state ve-

locity in $\mathrm{SmB_6}$ differ by orders of magnitude, depending on the experimental technique used. Here we reconcile two techniques, scanning tunneling microscopy (STM) and angle-resolved photoemission spectroscopy (ARPES), by accounting for surface band bending on polar terminations. Using spatially-resolved scanning tunneling spectroscopy (STS), we measure a band shift of $\sim$ 20 meV between full-Sm and half-Sm terminations, in qualitative agreement with our density functional theory (DFT) calculations of the surface charge density. Furthermore, we reproduce the apparent high-velocity surface states reported by ARPES, by simulating their observed spectral function as an equal-weight average over the two band-shifted domains that we image by STM. Our results highlight the necessity of local measurements to address inhomogeneously-terminated surfaces, or fabrication techniques to achieve uniform termination for meaningful large-area surface measurements of polar crystals such as $\mathrm{SmB_6}$.

3.1 INTRODUCTION

In a Kondo insulator (KI), strong interactions between localized *f* electrons renormalize their spectral weight towards the chemical potential. Below a characteristic temperature T^*, conduction electrons begin to scatter from these renormalized *f* states, opening a hybridization gap at the Fermi level. In a subset of KIs called topological Kondo insulators, this gap can encode a non-trivial bulk topological invariant, leading to the appearance of protected surface states [34, 78]. In the KI $\mathrm{SmB_6}$p, the onset of the hybridization gap leads to a resistivity upturn below $\sim$ 50 K [57, 58, 79]. Yet, rather than diverging, the resistivity saturates below 5 K, indicating the emergence of an additional conduction channel [41, 44]. This conduction channel has been attributed to topological surface states by several theoretical studies, which span complementary approaches including renormalized band theory and tight-binding Hamiltonians matched to LDA (+Gutzwiller) calculations [32, 39, 56]. These calculations predict the existence of three surface Dirac cones with heavy quasiparticles, of

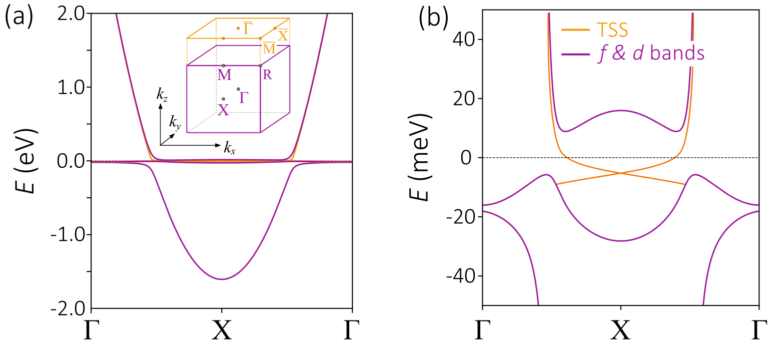

Figure 3.1: (a) Schematic of the SmB$_6$ band structure, showing two heavy f bands hybridizing with a light d band (all purple), and topological surface states (TSS, orange) that have a low velocity. Inset of (a): Bulk and surface Brillouin zone of SmB$_6$p. (b) Zoom-in of band structure at the Fermi level.

predominantly f character, as shown schematically in Fig. 3.1. Such low-velocity Dirac fermions would provide a high density of states at the Fermi level, increasing their susceptibility to exotic orders and their potential utility [35, 37, 40, 56]. However, the empirical identification of the additional conduction channel [41, 44] with the predicted topological surface states [32, 39, 56] has remained controversial due to apparent contradictions between different experimental techniques.

Experimentally, angle-resolved photoemission spectroscopy (ARPES) and scanning tunneling microscopy (STM) have each identified key features of the topological states in SmB$_6$p, but with quantitative and qualitative differences. At low temperatures, ARPES studies reported a hybridization gap that hosts linearly dispersing surface states [45–49] with a non-trivial spin texture [80, 81]. However, the apparent velocity of these states is an order of magnitude higher than theoretically predicted (see Table 3.1). Meanwhile, the hallmark of a topological surface state—its Dirac point—has not been clearly resolved in any ARPES experiment to date [47], leading to the suggestion that it has been pushed into the valence band by a strong surface potential [82], or by the breakdown of the Kondo effect at the surface [33]. On the other hand, milliKelvin scanning tunneling spectroscopy (STS) studies identified several strong resonances within the hybridization gap, consistent with low-velocity surface states [68, 83]. Additionally, momentum-resolved STM directly imaged linearly

Table 3.1: Comparison of SmB_6 surface-state properties predicted by theory and measured by STM, ARPES, and quantum oscillations. We tabulate values for the Fermi velocity v, Dirac-point energy E_D, and surface Fermi wavevector k_F, at both the $\overline{\mathrm{X}}$ and $\overline{\Gamma}$ points of the surface Brillouin zone.

	Theory [39]	STM [1]	ARPES [49]	Quantum scillation [53]
$\hbar v_{\bar{X}}$ (meV·Å)	7.6 ± 0.3	16 ± 2	240 ± 20	1900 ± 300
$E_{D_{\bar{X}}}$ (meV)	-5.4 ± 0.1	1 ± 1	-65 ± 4	-57 ± 9
$(k_{F_{\bar{X}}} - \bar{X})(\pi/a_0)$	0.44 ± 0.06	0.19 ± 0.02	$0.51 \pm 0.03\,(\Gamma - \mathrm{X} - \Gamma)$	0.039 ± 0.003
$\hbar v_{\bar{\Gamma}}$ (meV·Å)	90 ± 9	50 ± 2	220 ± 20	4300 ± 100
$E_{D_{\bar{\Gamma}}}$ (meV)	-9 ± 2	-7 ± 1	-23 ± 3	-460 ± 20
$k_{F_{\bar{\Gamma}}}(\pi/a_0)$	0.07 ± 0.01	0.14 ± 0.02	0.15 ± 0.03	0.142 ± 0.001

dispersing low-velocity surface states that converge to a Dirac point within the gap [1], consistent with theoretical predictions [39].

The apparent inconsistencies between STM and ARPES arise from the different experimental length scales for each technique. STM typically images hundred-nanometer regions with picometer spatial resolution. On SmB_6p, STM universally observes surface domains with sizes on the order of tens of nanometers [1, 62, 63, 68, 83, 84], consistent with its polar structure and the lack of a natural cleavage plane. Yet the typical ARPES spot size is on the order of tens of microns [85], and consequently averages over thousands of SmB_6 surface domains. This averaging poses a problem if the various domains exhibit polarity-driven band bending, as ARPES spectra will contain a superposition of spectral features, shifted in energy with respect to one another.

Here we use STM spectroscopy to guide a simulation of the spectral functions on polar Sm 1×1 and non-polar Sm 2×1 terminations, using the energy and momentum broadening of typical ARPES experiments. For a range of realistic experimental parameters, our *simulated* ARPES spectra show topological surface states with an artificially enhanced Fermi velocity and a buried Dirac point, similar to published *experimental* ARPES results. Our findings provide the long-sought, fully-consistent explanation for the apparent discrepancy between the band structure measured by

ARPES and STM. They further confirm the consistency between STM and theoretical predictions of low-velocity surface states with an in-gap Dirac point and high density of states at the Fermi level.

3.2 METHODS

We performed STM experiments on single crystals of SmB_6 grown using the Al-flux method [43, 72]. We cleaved the crystals in cryogenic ultra-high vacuum at ~ 30 K before inserting them into the STM head. We prepared PtIr STM tips by *ex situ* mechanical sharpening then *in situ* field emission on Au foil.

We performed calculations in the framework of density functional theory (DFT), as implemented in the Quantum ESPRESSO package [86]. We calculated the exchange-correlation functional using the generalized gradient approximation of Perdew-Burke-Ernzerhof (GGA-PBE) [87]. The electron-ion interactions are described by ultrasoft pseudopotentials with valence electron configurations of $2s^2 2p^1$ for B atoms and $5s^2 4d^{10} 5p^6 6s^2 4f^6$ for Sm atoms. The energy cutoff for the plane wave basis is 120 Ry with a charge density cutoff of 500 Ry. We used a Monkhorst-Pack [88] scheme with a $12 \times 12 \times 1$ k-mesh for the Brillouin zone integration for the supercell with one unit cell (1×1 Sm) and $6 \times 12 \times 1$ k-mesh for the supercell with two unit cells (2×1 Sm). In all calculations, the lattice parameter was fixed at the experimental value $a_0 = 4.13$ Å, with slab thickness 20.65 Å and vacuum thickness 15 Å to minimize interactions between the periodic images. We did not consider spin polarization or spin-orbit coupling since our focus is on the electrostatics of the material.

3.3 SURFACE CHARACTERIZATION

Due to its lack of a natural cleavage plane, an abundance of distinct surface terminations have been observed by STM on SmB_6 [89]. Across a dozen STM experiments, the largest reported domain of

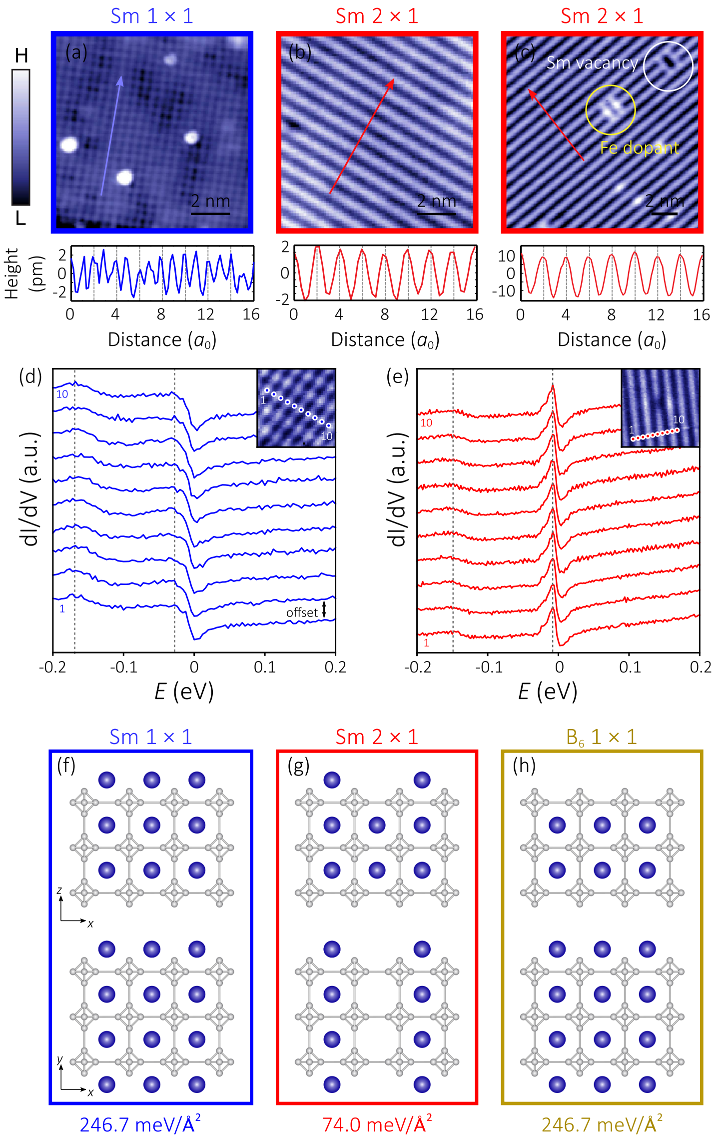

Figure 3.2: STM topography of the (a) Sm 1×1 termination and the Sm 2×1 termination of (b) pristine SmB$_6$ and (c) Fe-doped SmB$_6$ [1]. Acquisition parameters are: (a) $T = 9.5$ K, $V_s = 200$ mV, $R_J = 10\ \mathrm{G\Omega}$ (b) $T = 8.5$ K, $V_s = 100$ mV, $R_J = 5\ \mathrm{G\Omega}$ and (c) $T = 6.5$ K, $V_s = 100$ mV, $R_J = 0.5\ \mathrm{G\Omega}$. (d) - (e) Spatially homogeneous dI/dV spectra on the Sm 1×1 and Sm 2×1 surface. Each curve is offset for clarity. The location is indicated in the inset of each panel. The inset in (d) shows an area of 2.5×2.5 nm^2 and (e) an area of 5.1×5.1 nm^2. Acquisition parameters are: (d) $T = 9.5$ K, $V_\mathrm{s} = -200$ mV, $R_\mathrm{J} = 2\ \mathrm{G\Omega}$, bias excitation amplitude $V_\mathrm{rms} = 2.82$ mV, and (e) $T = 6.5$ K, $V_\mathrm{s} = 200$ mV, $R_\mathrm{J} = 1\ \mathrm{G\Omega}$, bias excitation amplitude, $V_\mathrm{rms} = 1.41$ mV. (f) - (h) Side-view (upper) and top-view (lower) of different surface terminations and their corresponding formation energies, calculated by DFT.

an ordered surface on pristine SmB_6 ($< 1\%$ dopants) is only 60 nm [1, 62, 63, 68, 83, 84, 89–91].

Two commonly observed surfaces are the 1×1 square lattice [Fig. 3.2(a)] and the 2×1 rows that arise when half of the Sm atoms are removed during cleaving [Fig. 3.2(b) and 3.2(c)] [89, 92]. The 2×1 surface has also been observed by low-energy electron diffraction [93] and ARPES, where it manifests as Umklapp scattering [46, 52]. We confirmed the identity of the $2{\times}1$ surface using lightly Fe-doped samples where Fe is known to substitute for Sm [77]; we observed individual Fe-atom signatures centered on the rows of Sm atoms in Fig. 3.2(c). We confirmed the identity of the 1×1 lattice presented in Fig. 3.2(a) as a full Sm layer due to the direction of its band bending compared to the 2×1 surface, as shown in Fig. 3.2(d-e) and discussed in more detail below.

The relative prevalence of each surface can be understood from its formation energy [Figs. 3.2(f-h)]. Although most STM reports have focused on the 1×1 surface [62, 63, 68, 83], our more frequent observation of the 2×1 surface is consistent with its lower formation energy as calculated by DFT. In general, a more balanced charge distribution on either side of the cleave, as drawn in Fig. 3.2(g), is intuitively expected to lower the surface formation energy.

3.4 TERMINATION-DEPENDENT BAND BENDING

In general, the surface termination can cause a redistribution of charge that affects the local electronic structure, an effect well studied in conventional semiconductors [94]. In bulk SmB_6p, Sm atoms donate equal amounts of charge to the B_6 octahedra above and below them. However, on the 1×1 surface the Sm atoms are under-coordinated; the B layer beneath the topmost Sm layer cannot accept all of the excess electrons, so they accumulate on the surface. This charge accumulation is qualitatively captured in our calculations of the electron transfer, which use Bader analysis to partition the DFT charge density (Fig. 3.3).

The increased electron density near the 1×1 surface leads to reduced surface charge transfer

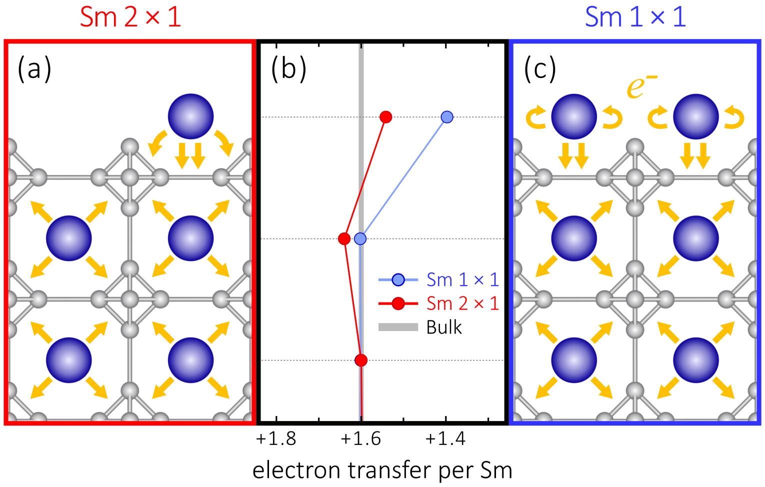

Figure 3.3: DFT-calculated electron transfer from Sm atoms to B_6 clusters for the 2×1 surface (a) and the 1×1 surface (c). Fewer electrons are drawn from each Sm atom on the 1×1 surface as compared to the 2×1 surface.

shown as a blue line in Fig. 3.3(b), greater filling of the Sm orbitals, and to a slight downward bending of the surface bands. On the other hand, Sm atoms at the 2×1 surface can donate a greater fraction of their electrons to the B layer below, because there are only half as many Sm atoms at the surface as in the bulk. Correspondingly, we found only a minor deviation in the calculated charge transfer at the 2×1 surface, shown as a red line in Fig. 3.3(b). Although our Bader charge analysis quantitatively departs from the experimental Sm valence of around $+2.5$ [95], it provides a qualitative understanding of the charge transfer on the SmB_6 surface.

To experimentally determine the accumulation of surface charge, we measured local differential conductance, $dI/dV(\mathbf{r}, E)$, where I is the tunneling current and V is the bias applied to the sample with respect to the tip. On a typical ordered domain, there are three pronounced spectral features: a peak around -150 meV, a peak just below E_F, and a shoulder around 40 meV, as shown in Fig. 3.4(a). The two filled-state peaks predominantly reflect contributions from the Sm $4f$ states, as determined by previous STM and ARPES measurements, and by dynamical mean-field theory calculations [1, 83, 84, 96]. Although the peak energies are homogeneous within each ordered domain

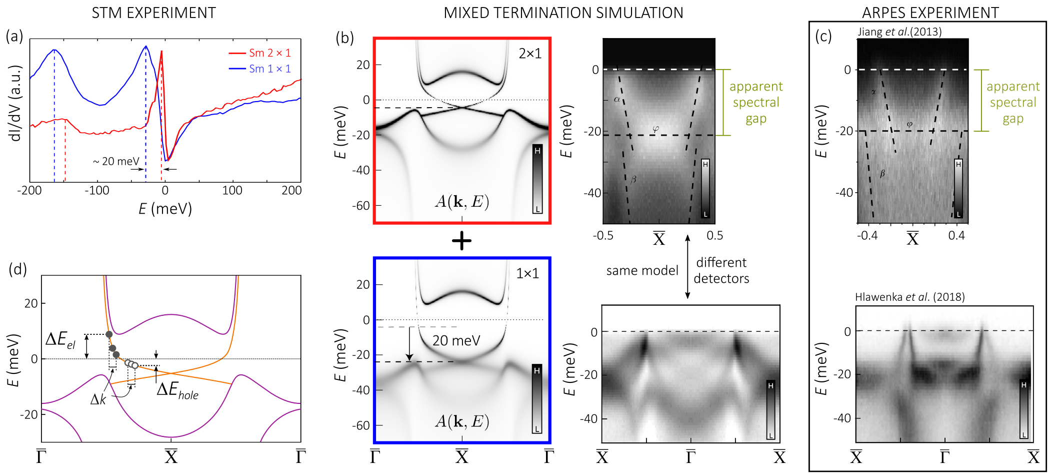

Figure 3.4: (a) Measured dI/dV on two different surfaces of SmB$_6$p. Acquisition parameters are (blue curve) $T = 9$ K, $V_s = -250$ mV, $R_J = 2$ GΩ, bias excitation amplitude $V_{\mathrm{rms}} = 2.8$ mV, and (red curve) $T = 8$ K, $V_s = 200$ mV, $R_J = 1$ GΩ, $V_{\mathrm{rms}} = 1.4$ mV. (b) Starting with the electronic structure derived by STM on the non-polar 2×1 surface (red) [1], we inferred the electronic structure on the 1×1 polar termination by rigidly shifting the occupied states down by 20 meV (blue), based on our local STS measurements. The average of the simulated spectral functions from the 2×1 and 1×1 surfaces imitates the result of a spatially averaging measurement such as ARPES. We convoluted the averaged spectral function with a Gaussian kernel in order to account for finite temperature, energy and momentum resolution. The following realistic experimental parameters have been used to simulate the spectra along the $\overline{\mathrm{M}} - \overline{\mathrm{X}} - \overline{\mathrm{M}}$ and $\overline{\mathrm{X}} - \overline{\Gamma} - \overline{\mathrm{X}}$ directions. Upper panel: $T = 12$ K, $\Delta E = 10$ meV, $\Delta k = 0.04$ Å^{-1} (as reported in Ref. [49]); lower panel: $T = 1$ K, $\Delta E = 3$ meV, $\Delta k = 0.01$ Å^{-1} (as reported in Ref. [52]). Furthermore, we included band folding as described in Ref. [52] for the simulation presented in the lower panel. Despite the low-velocity Dirac fermions we started with, both simulations give the appearance of high-velocity states at the Fermi level that reproduce the ARPES experimental data presented in Refs. [49] and [52]. (c) Two different ARPES intensity maps are reproduced from Refs. [49] and [52] for direct comparison with our mixed-termination simulations in panel (b). (d) Adding electrons increases the Fermi level by a large amount due to the high velocity of the surface states above the chemical potential, whereas removing electrons decreases the Fermi level by only a small amount given the low surface state velocity below the chemical potential..

[see Fig. 3.2(d-e)], we found that the peaks are shifted downward on the 1×1 surface by about 20 meV compared to the 2×1 surface.

3.5 SPECTRAL FUNCTION SIMULATION

ARPES spectra can be broadened by local band bending if the spot size encompasses multiple surface domains of different polarity. We investigated this possibility in SmB$_6$ by deriving a spectral function for each termination, from our STM measurements [1]. In accordance with our data, our simulation includes low-velocity Dirac states close to the chemical potential, connecting a light bulk *d* band to two heavy bulk *f* bands. Each state includes a Fermi-liquid-like quasiparticle decay rate $\propto \omega^2$ [97]. We simulated each termination by adjusting the energies of the *f* and *d* bands to match our STM spectra. Specifically, in the 1×1 spectral-function simulation, the occupied states are shifted down by 20 meV relative to the 2×1 simulation. We simulated ARPES spectra by computing an equal-weighted average of the spectral functions for each surface, then convolving the result with a Gaussian kernel that accounts for detector resolution and temperature broadening as shown in right panels of Fig. 3.4(b). Specifically, we mimic the detectors in Ref. [49] with parameters $T = 12$ K, $\Delta E = 10$ meV, and $\Delta k = 0.04$ Å^{-1}, and Ref. [52] with parameters $T = 1$ K, $\Delta E = 3$ meV, and $\Delta k = 0.01$ Å^{-1}. In each case, our simulation captures the main features of the measured ARPES spectra as reproduced in Fig. 3.4(c): an apparent hybridization gap of approximately 20 meV, and in-gap surface states with an apparent high velocity, which seem to extrapolate to a buried Dirac point [*].

3.6 DISCUSSION

A complete understanding of the cleaved SmB_6 surface requires considering both electron-rich surfaces, such as the Sm 1×1 surface, and electron-deficient surfaces, such as the B-rich terminations. Importantly, our STM measurements have shown that the heavy Dirac surface states become flat only below the chemical potential [1], leading to a highly electron-hole-asymmetric band-bending scenario, as depicted in Fig. 3.4(d) and Fig. 3.5. In such a scenario, we expect that surplus electrons, as found on Sm 1×1 terminations, primarily populate the steeper (upper) part of the surface-state

---

[*] The $\Gamma_8^{(2)}$ crystal-field-split 4*f* state is missing in our STM-derived simulation, but present in ARPES experiments. The discrepancy arises because STM does not couple strongly to the $\Gamma_8^{(2)}$ state, which lacks the correct symmetry to hybridize. However the lack of hybridization also means that the $\Gamma_8^{(2)}$ state does not play an important role in Kondo or topological physics.

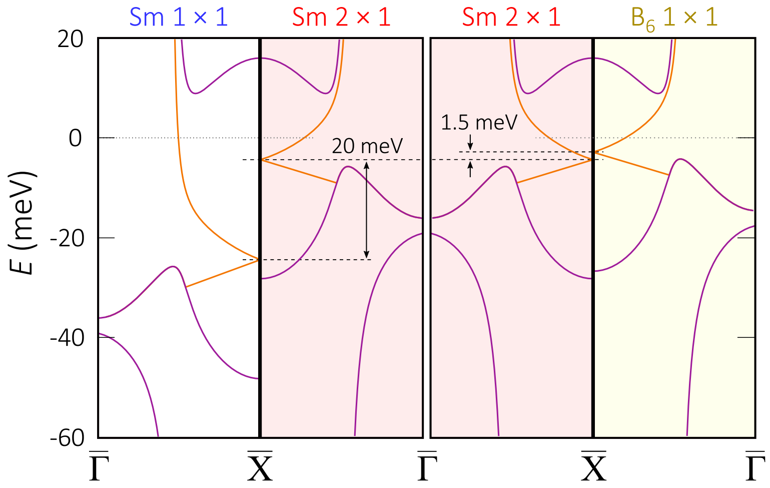

Figure 3.5: Band bending range on SmB_6 surfaces. The Sm 1×1 is the most negatively charged surface with a measured downward band bending of 20 meV, compared to the charge neutral Sm 2×1 surface. Bands on the B_6 1×1 surface, which is the most positively charged surface, are shifted up by 1.5 meV [68]. Therefore, our simulation including just the Sm 1×1 and Sm 2×1 surface spans more than 90 $\%$ of the maximum energy range of 21.5 meV.

dispersion [see Fig. 3.1(b)], producing a notable downward shift of spectral features, as shown in Fig. 3.4(a). Conversely, a surface deficient of electrons, as expected for B-rich terminations, would depopulate the very flat (lower) part of the surface-state dispersion. Due to the dramatic difference in band slope (velocity) above and below the Fermi level, spectral features would be shifted upward by much less on a surface with missing electrons, than they would be shifted downward on a surface with the same number of excess electrons. Indeed, on B_6 1×1 surfaces, STM measured a prominent peak at -6.5 meV [68], which is shifted upward by only 1.5 meV compared to the corresponding peak on the neutral Sm 2×1 surface [see Fig. 3.4(a)]. Thus, the total band-bending range, defined by the most negatively charged Sm 1×1 termination and the most positively charged B_6 1×1 termination, is 21.5 meV, as shown in Fig. 3.5. Therefore, our ARPES simulation, using data from the two surfaces we observe, covers more than 90% of the maximum possible surface band-bending.

While our study focuses on the (001) surface, recent ARPES experiments also reported high-velocity surface states on the (110) and (111) surfaces [98, 99]. These reports are surprising because both surfaces are nominally non-polar and hence are expected to host low-velocity Dirac states. In fact, magnetothermoelectric studies have already indicated the presence of heavy metallic states on the (110) surface [59], contrary to the ARPES measurement. Under closer inspection by STM, the (110) surface appears to be inhomogeneous on small length scales [89]. The intense atomic-scale disorder may alter the local electronic environment and cause local charging, analogous to termination-dependent band bending on the (100) surface [83]. This local charging would be averaged in ARPES measurements, possibly resulting in enhanced surface-state velocities, similar to our simulations on the (100) surface (Fig. 3.4).

Band bending on SmB_6 may also affect the perception of the hybridization gap and explain the apparent discrepancy between its size, as reported by ARPES and STM. ARPES generally reports 15-20 meV for the part of the hybridization gap below E_F, as shown in Fig. 3.4(c) [45–49, 52], while the *full* gap, as measured by STM, is only 8-15 meV [1, 62, 68, 83]. In Fig. 3.4(b), our ARPES simulation shows a large gap below E_F, of about 25 meV, despite arising from a band structure with a gap of only 15 meV on the non-polar surface, as measured by STM. Specifically, averaging over different surface terminations blurs the top of the bulk valence band, which introduces an apparent increase of the hybridization gap on the occupied side. The full impact of excess charge on the surface Kondo environment and *d*-*f* hybridization remains an open theoretical question [33].

SmB_6 is a promising platform for devices that exploit correlated topological phases, but its cubic and polar structure give rise to small, charged surface domains, on which band bending may locally distort the Dirac surface states. Using STM spectroscopy, we investigated two distinct surface terminations and measured a band shift of about 20 meV between them. These measurements guided a simulation of ARPES spectra, which captures the essential experimental features of ARPES, but remains consistent with STM conclusions [1]. Our results suggest that band bending is most pronounced on Sm-rich terminations, motivating the development of new surface treatments or epitaxial-growth techniques such as molecular beam epitaxy to achieve a more uniform termination. Control over the termination would allow the important correlated surface states to be tuned closer to the Fermi level, without introducing disorder through chemical doping, which would be advantageous for future applications [100].

4

Visualizing the charge puddles around Kondo holes

Many of today's quantum materials are impacted by intrinsic charge inhomogeneity, especially those with strong electron interactions that promote competing orders [101]. In a Kondo lattice, the interaction between itinerant conduction electrons and local *f* moments generates heavy fermions—quasiparticles with masses hundreds of times that of a bare electron [15, 16]. This interaction unwinds around atomic disruptions to the *f* electron site, called "Kondo holes", leading to puddles of itinerant charge that nucleate local magnetic structure [73, 102–104]. Yet such charge environments have eluded measurement at the atomic scale, largely because their strong inherent screening reduces the electrostatic potential. Here we introduce a technique to visualize the charge distribution in heavy-fermion systems with sub-nanometer resolution using a conventional scanning tunneling microscope (STM). Specifically, we measure the local rectification $R(\mathbf{r}, V) = |I(\mathbf{r}, +V)/I(\mathbf{r}, -V)|$, which tracks small shifts in the Kondo resonance as it adjusts to different charge environments. Using this technique, we image the charge redistribution around spin-less thorium atoms in URu_2Si_2 and discover signatures of unhybridized conduction electrons existing within its heavy-fermion ground state. Meanwhile, in the topological Kondo insulator SmB_6, we discover that Sm-site defects are Kondo holes that harbor puddles of itinerant charge extending for around 6 nm. Our results suggest that the prevalence of local magnetism around Kondo holes can fully explain the mysterious 3D quantum oscillations recently measured in Kondo insulators [19, 20]. Finally, we anticipate our work to be a starting point for developing atomic-scale charge sensors using heavy-fermion probes.

4.1 KONDO HOLES NUCLEATE PUDDLES OF UNHYBRIDIZED ELECTRONS

At nanometer length scales, intrinsic charge inhomogeneity is commonplace, but its consequences are often complex, especially in materials with strong electron interactions that promote competing orders [101]. In Kondo-lattice systems, the competition between antiferromagnetic ordering of local *f* moments and their screening by conduction electrons leads to a rich phase diagram exhibiting quantum criticality [13], unconventional superconductivity [14], and heavy fermions [15, 16]—quasiparticles entangled with *f*-electron character (see Fig. 4.1(a)). Atomic-scale disorder provides

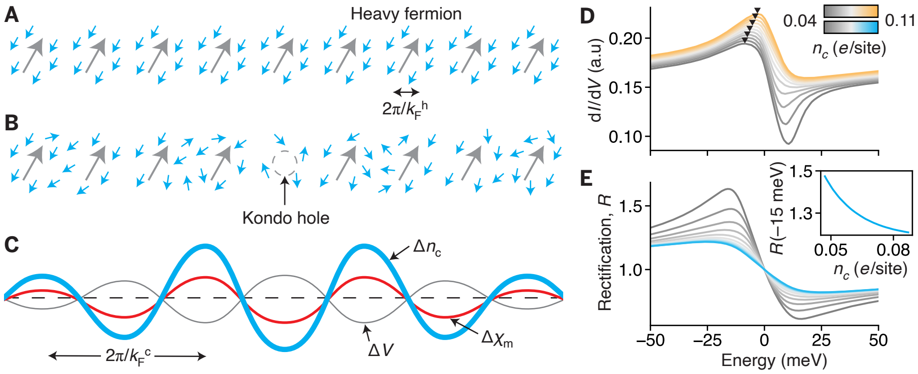

Figure 4.1: **Calculations of the disrupted screening cloud around Kondo holes.** (**A**) In a Kondo lattice environment, magnetic moments at each site (gray arrows) are coherently screened by itinerant conduction electrons (blue arrows) to form a spin-less ground state of heavy fermions (orange line), characterized by the wavevector $k^{\mathrm{h}}_{\mathrm{F}}$. (**B**) If one moment is removed to create a Kondo hole, the conduction electrons previously screening it can redistribute themselves. (**C**) The redistributed screening cloud contains oscillations in the conduction electron density (Δn_{c}), interaction strength (ΔV), and magnetic susceptibility $(\Delta\chi_{\mathrm{m}})$, as shown schematically. (**D**) In a Kondo lattice, the calculated dI/dV contains a peak-dip feature near the Fermi level, due to co-tunneling into the Kondo resonance. The energy position of this peak (black triangles) shifts according to the local charge, n_{c}. (**E**) The asymmetric dI/dV induces a strong peak in the rectification $R(\mathbf{r}, V) = |I(\mathbf{r}, +V)/I(\mathbf{r}, -V)|$, whose amplitude changes as the Kondo resonance shifts position. These changes are nearly linear for the small range of local doping expected around a Kondo hole (inset).

both a probe of the electronic structure of these phases [65] and a tuning parameter to promote correlated phases [73]. By substituting the f-contributing atom or by removing it entirely, an impurity in a dense Kondo lattice locally untangles the hybridized heavy-fermion ground state [102], leaving puddles of unhybridized electrons behind (see cartoon in Fig. 4.1(b)). As the disrupted electrons reorganize to form a new screening cloud, they adjust the strength of their interactions with the remaining f moments [73], leading to enhanced local magnetism [104] (Fig. 4.1(c)). If the same mechanism exists in the topological counterparts to these systems [32], then the breakdown of hybridization around Kondo holes may locally prohibit the emergent topological phase. At higher concentrations, the Dirac surface states could mediate interactions between Kondo holes, leading to new phases, like a spontaneous quantum anomalous Hall effect [40].

Early indications of Kondo holes were found in the low-temperature resistivity and specific heat of heavy-fermion metals doped with nonmagnetic impurities [105]. More recently, the hybridization disorder around Kondo holes was visualized at atomic length scales [106], supporting the existence of unhybridized electrons in the redistributed screening cloud [73]. Directly coupling to these charge puddles is difficult, as the metallic screening strongly renormalizes the bare charge distribution. However, there are a few promising new approaches [107–109]. The most widespread among them is to decorate the tip of a Kelvin probe force microscope with a single atom or molecule [110, 111]. This technique was recently used to image charge variations within a single molecule [112]. However, it becomes inaccurate for small tip-sample separations due to the influence of short-range forces [113, 114], complicating further improvements to its spatial resolution [115]. Meanwhile, a scanning tunneling microscope (STM) routinely achieves the sub-nanometer spatial resolution, cryogenic temperatures, and meV energy resolution required to access atomic charge distributions, but existing methods to extract the electrostatic potential from the STM vacuum decay length contain significant artifacts [116]. Consequently, simultaneously achieving the high precision and high resolution required to measure the screened charge environment around a Kondo hole is not possible using existing techniques.

Here we develop a new STM modality to image the charge environment in Kondo-lattice systems with sub-ångström resolution. Specifically, we measure the ratio of forward-to-backward tunneling current, i.e. the local rectification $R(\mathbf{r}, V) = |I(\mathbf{r}, +V)/I(\mathbf{r}, -V)|$, where I is the sample-to-tip tunneling current at position $\mathbf{r}$ and applied sample bias V. At high biases above 100 mV, $R(\mathbf{r}, V)$ was previously used to track charge inhomogeneity from the spectral weight transfer in hole-doped cuprates [117]. We focus on low biases, typically $V \lesssim 10$ mV, where spatial variations in $R(\mathbf{r}, V)$ mirror the response of the Kondo resonance to its local charge environment. These variations image the disrupted screening cloud around spin-less thorium atoms in URu_2Si_2 and around three separate Sm-site defects in SmB_6: Fe dopants, Gd dopants, and Sm vacancies. We identify these three Kondo holes as the primary origin of topological backscattering in SmB_6, indicating the development of local magnetism. Importantly, the charge puddles we image in SmB_6 contain the same, unexpected wavevector seen in recent quantum oscillation experiments [19, 118], suggesting that Kondo-lattice defects contribute to those measurements.

4.2 IMAGING KONDO HOLES IN $\mathrm{URU_2SI_2}$

Our technique uses the energy shift of the Kondo resonance $\varepsilon_f(\mathbf{r})$ to detect the local charge environment. In a mean-field description, $\varepsilon_f(\mathbf{r})$ is a Lagrange multiplier that enforces uniform f-electron occupation, typically constraining $\langle n_f \rangle = 1$ at each site. As additional carriers Δn_c enter the system, ε_f adjusts position to ensure the constraint is still met, by adding or depleting f-electron character from the reshaped Fermi surface (see calculation in Fig. 4.1 (d)). The magnitude and direction of the ε_f shift depend on the details of the band structure. But the relationship between Δn_c and ε_f is linear over a wide doping range, implying that the local charge environment can be inferred from measuring ε_f. The Kondo resonance usually appears as a peak-dip feature in the STM tunneling conductance $\mathrm{d}I/\mathrm{d}V$ [119] due to the presence of multiple tunneling channels [75, 76]. In simple cases, ε_f can be estimated by fitting $\mathrm{d}I/\mathrm{d}V$ to a Fano or co-tunneling model [65, 120], though the exact value can depend on the model used. Consequently, measurement of the sub-meV energy shift of $\varepsilon_f(\mathbf{r})$ is not reliable for detecting the charge redistribution around a Kondo hole. On the other hand, the strong peak-dip feature associated with the Kondo resonance naturally creates a pronounced peak in the rectification. The height of this peak is insensitive to STM setup artifacts [117], but it changes dramatically as ε_f shifts, because the rectification primarily probes the particle-hole asymmetry of the local density of states (see Fig. 4.1(e)).

To demonstrate our technique for detecting local charge, we first studied Kondo holes in 0.1%-thorium-doped $\mathrm{URu_2Si_2}$, which undergoes a transition to a coherent heavy-fermion state below $T_o = 17.5$ K [65, 121–123]. Above this temperature, it displays roughly metallic behavior with a Fermi surface consisting of a single conduction band with wavevector $k_F^c \approx 0.3\,\pi/a$, where a

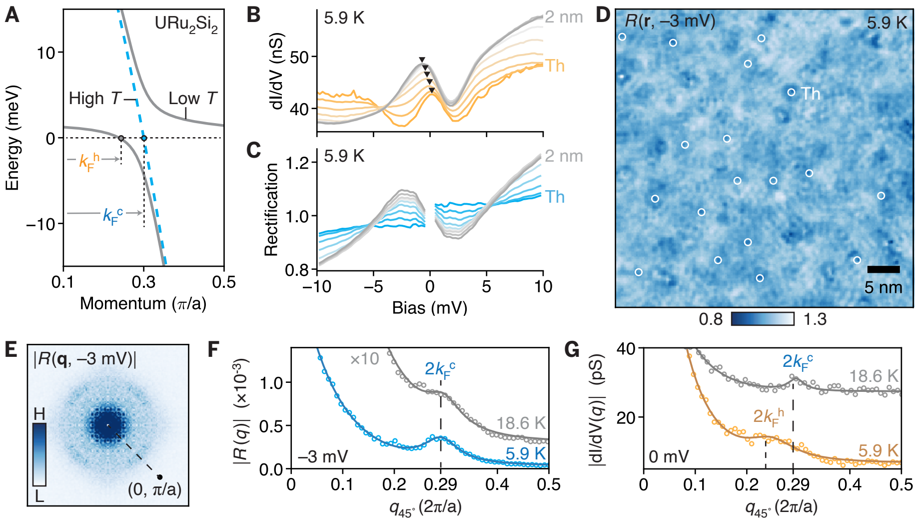

Figure 4.2: Kondo holes in URu$_2$Si$_2$. (**A**) Heavy fermions emerge in URu$_2$Si$_2$ at temperatures below about 17 K as itinerant conduction electrons (blue line) hybridize with a renormalized 5f level, reducing the Fermi wavevector from k_F^c to k_F^h. (**B**) The formation of heavy fermions is characterized by an asymmetric Fano lineshape in the tunneling conductance (gray curve). Near a thorium dopant, the conductance trace reveals a sharp in-gap resonance (orange), a signature of a Kondo hole. (**C**) The amount of rectification is highly sensitive to the dI/dV peak position (black triangles in **B**), which shifts towards zero near the dopant, consistent with the modified local charge density. The spectra in **B** and **C** are averaged over the 18 well-isolated thorium dopants shown in panel **D**. (**D-E**) The measured rectification ratio contains clear oscillations (**E**) that manifest as a ring in the 4-fold-symmetrized Fourier transform. (**F**) These oscillations match the high-temperature Fermi wavevector of $2k_F^c$, both above and below the heavy-fermion crossover. (**G**) In contrast, a conventional dI/dV measurement couples to the temperature-dependent Fermi surface, which changes dramatically from 18.6 K to 5.9 K. For clarity, the 18.6 K data has been scaled in **F** and offset in **G**.

is the lattice constant (see Fig. 4.2(a)). Below T_o, the Fermi wavevector jumps to $k_F^h \approx 0.25\ \pi/a$ due to the coherent onset of two heavy bands [65]. Substituting spin-less thorium atoms for magnetic uranium atoms is known to induce Kondo-hole behavior [103], creating oscillations in the local hybridization at $2k_F^c$ [106]. These defects also act as scattering centers, generating quasiparticle interference patterns in dI/d$V(\mathbf{r}, V)$ at the heavy-fermion wavevector $2k_F^h$ [65]. The established coexistence of these two wavevectors and the accessible temperature of the metal-like state make URu$_2$Si$_2$ an ideal compound to characterize our new technique using the expected charge puddles around Kondo holes.

We simultaneously measured $R(\mathbf{r}, V)$ and dI/d$V(\mathbf{r}, V)$ on the uranium termination of URu$_2$Si$_2$, both above and below T_0. The coherent onset of heavy fermions below T_0 is accompanied by the appearance of a peak-dip feature in dI/dV: the Kondo resonance (see Fig. 4.2(b)). Close to a thorium dopant, this feature evolves into a in-gap resonance, shifting the peak position upwards. This shift—and even the barely perceptible shifts 2 nm away from the dopant—are strongly amplified by measuring the rectification (see Fig. 4.2(c)). For biases within the hybridization gap $|v|/e \lesssim 5$ mV (where $-e$ is the electron charge), the rectification measured in a larger 60×60 nm^2 area reveals widespread spatial oscillations emanating from thorium dopants, as shown in Fig. 4.2(d). These long-lived oscillations create sharp peaks in the Fourier transform along the lattice direction at 0.29 ± 0.01 $(2\pi/a)$ (see Fig. 4.2(e-f)). Their wavevector is in excellent agreement with $2k_F^c$, as determined from quasiparticle interference patterns in dI/d$V(\mathbf{r}, V)$ above T_0, but it is distinct from the heavy bands measured in dI/d$V(\mathbf{r}, V)$ below T_0 (see Fig. 4.2(g)). The existence of these rectification oscillations at $2k_F^c$ suggest that some electrons retain their itinerant character around Kondo holes, even below T_0.

4.3 IMAGING KONDO HOLES IN SmB$_6$

If Kondo holes similarly liberate electrons in the insulating counterparts to heavy-fermion metals, they could contribute to a number of recent bulk anomalies seen in Kondo insulators, like the low-temperature upturn in linear specific heat [17], the finite AC optical conductivity [18], and the 3D Fermi surface inferred from quantum oscillation [19, 20] and Compton scattering [21] experiments. In the topological Kondo insulator SmB$_6$, these metallic properties persist even as the bulk resistivity increases by 10 orders of magnitude [22]! This discrepancy led to several theoretical proposals—some suggest that the metallic behavior is intrinsic [23–25], and some implicate defects [27–30]. Experimentally, an increased concentration of Sm vacancies was shown to globally inhibit the development of the hybridization gap [124], and eventually lead to bulk DC conduction [22].

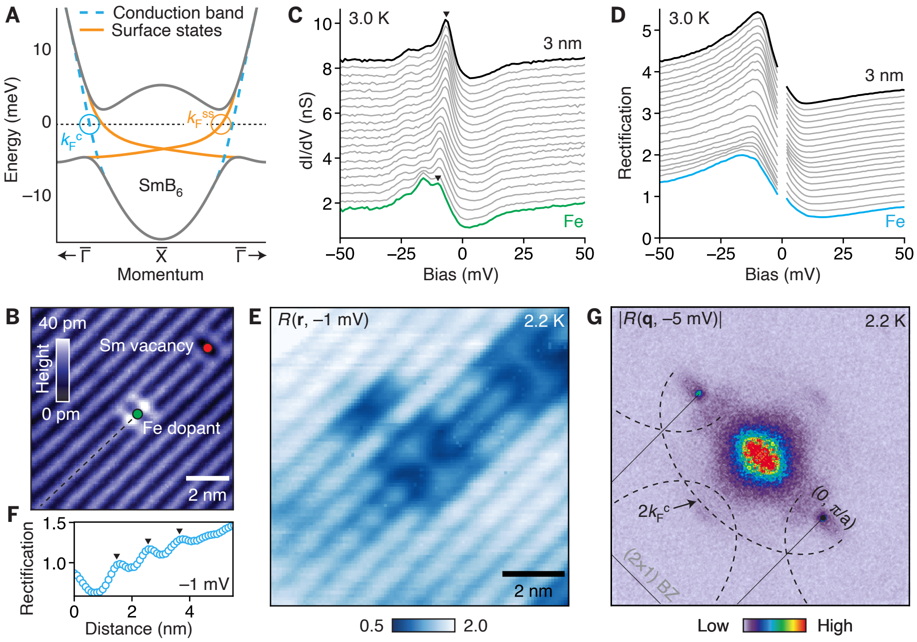

Figure 4.3: Kondo holes in SmB$_6$. (**A**) In SmB$_6$, the hybridization of conduction electrons (blue line) with localized $4f$ moments leads to an inverted band structure (gray) hosting emergent heavy Dirac surface states with a reduced Fermi wavevector (orange), as shown in this schematic. (**B**) Both the Fe dopant and Sm vacancy in this area of (2×1)-reconstructed SmB$_6$ are expected to act as Kondo holes because they each displace a $4f$ moment. (**C-D**) The $\mathrm{d}I/\mathrm{d}V$ peak changes position near the Fe dopant (black triangles), leading to large variations in the local rectification. The spectra in **C** and **D** have been offset for clarity. (**E**) The measured rectification in the same area as **B** contains clear oscillations around the two impurities. (**F**) Linecut of the rectification along the black dashed line in **B**. (**G**) In a larger 80×80-nm^2 area, these oscillations appear as a sharp ring in the 2-fold-symmetrized Fourier transform, which matches the unhybridized Fermi surface inferred from ARPES experiments (dashed lines).

Meanwhile, samples with high concentrations of Gd dopants appear to generate metallic puddles that amplify local magnetism [125, 126]. Similar local magnetism was observed in samples with intentional Fe dopants [77], another Sm-site defect. All of these facts suggest the presence of Kondo holes, yet their key signature—the accompanying charge oscillations at $2k_\mathrm{F}^\mathrm{c}$—remain undetected by any microscopic probe.

We imaged charge oscillations at $2k_\mathrm{F}^\mathrm{c}$ around around three candidate Kondo holes in SmB$_6$: Sm vacancies, Fe dopants, and Gd dopants, two of which are shown in Fig. 4.3(b). We focused on the 2×1-reconstructed Sm termination, as its charge environment most closely represents that of the

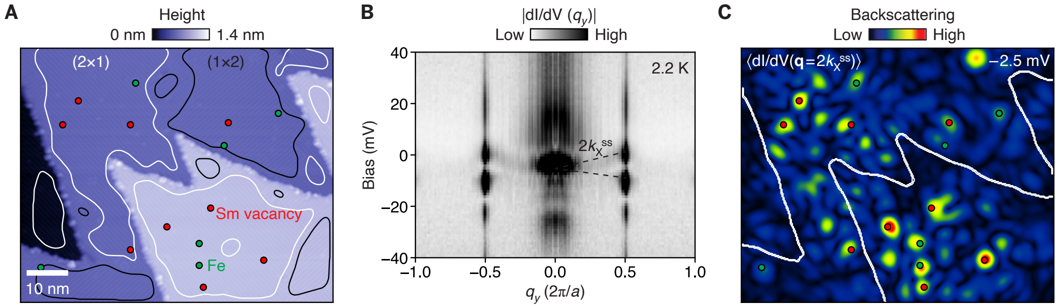

Figure 4.4: Kondo holes backscatter heavy Dirac fermions. (**A**) This area of SmB$_6$ contains several Kondo holes (red and green dots) on several (2×1)- or (1×2)-reconstructed patches (solid lines). (**B**) For energies within the Kondo insulating gap, the Fourier-transformed dI/dV along q_y contains a linearly dispersing signal (black dashed line) corresponding to quasiparticle interference from backscattered heavy Dirac fermions. The Fourier transform from (1×2) domains were rotated by 90° before being averaged with those from (2×1) domains. (**C**) The amount of topological backscattering, calculated from Fourier-filtering dI/dV at the backscattering wavevector $q = 2k_X^{ss}$, is strongly peaked around each Kondo hole. This map is computed only for ordered patches of the sample, as marked in **A**, and excludes the step edges.

bulk [2]. Close to a Fe dopant, we noticed that the peak in dI/dV shifts in energy, strongly impacting the simultaneously measured rectification (see Fig. 4.3(c-d)). Similar shifts have been associated with the buildup of charge around boron clusters on the Sm (1×1) termination [83]. For biases within the hybridization gap $|v|/e \lesssim 10$ mV, a spatial map of the rectification reveals clear oscillations around dopants (see Fig. 4.3(e-f)). In a larger 80×80-nm^2 area (shown in Fig. 4.4(a)), these oscillations create a sharp ring in the Fourier transform of $R(\mathbf{r}, V)$, as shown in Fig. 4.3(g). Its wavevector is larger than that of the surface state detected by quasiparticle interference imaging [1] and it does not disperse with bias, indicating a different origin. On the other hand, its size closely matches the unhybridized 5d band found by extrapolating angle-resolved photoemission data [49] to the Fermi level, after accounting for band folding on the 2×1 surface (dashed lines in Fig. 4.3(g)). The oscillations in $R(\mathbf{r}, V)$ show for the first time the real-space structure of local charge puddles around Kondo holes in SmB$_6$, with a wavevector that matches the 3D Fermi surface measured by quantum oscillations [19].

4.4 The origin of topological backscattering

The prevalence of magnetism and the breakdown of hybridization around Kondo holes can explain the observation of backscattering in SmB_6 [1], which is generally forbidden for topological surface states. The surface states were already shown to be locally sensitive to magnetism: they are suppressed around Sm-site defects or when measured with a magnetic STM tip [90]. Furthermore, their emergence is tied to the coherence of the hybridization gap [1], suggesting that the reduced hybridization around Kondo holes [106, 124] may weaken them. To directly determine the microscopic mechanism linking Kondo holes and topological backscattering, we imaged $dI/dV(\mathbf{r}, V)$ on a large area of 2×1-reconstructed SmB_6 that contains 15 well-isolated Kondo holes (Fig. 4.4(a)). The $dI/dV(\mathbf{r}, V)$ maps contain quasiparticle interference patterns matching the wavevector for backscattering of topological heavy Dirac fermions $q = 2k_X^{\mathrm{ss}}$, in agreement with our previous report [1]. We searched for the origin of this signal by Fourier-filtering $dI/dV(\mathbf{r}, V)$ at the wavevector $2k_X^{\mathrm{ss}}$ to create a map of the local backscattering strength (Fig. 4.4(c)). The sharp peaks in this image are a consequence of the localized nature of the quasiparticle interference, a result of f-electron entanglement. Most of these peaks align with the positions of Sm vacancies or Fe dopants, indicating that Kondo holes are the dominant source of topological backscattering in SmB_6.

Atomic-scale charge inhomogeneity has a profound impact on many interacting quantum materials, but it is usually difficult to measure. In Kondo-lattice systems, images of the local rectification provide a rare peek at the ground-state charge landscape. They reveal puddles of itinerant electrons around defects, signaling a local breakdown of hybridization. In SmB_6, the connection between hybridization and topology poses a dilemma around Kondo holes—does topological protection extend to interaction-driven systems? Our observation of topological backscattering indicates that this protection is lost around Kondo holes, pointing to a Swiss-cheese-like state within the topological phase. Lastly, our demonstrated sensitivity of the Kondo resonance to its local charge environment, and its subsequent amplification in $R(r, V)$, open a new direction for atomic-scale charge sensing using heavy-fermion probes.

Part II

Rapidly prototyping quantum materials

5

Quantum mimicry

At the most basic level, the behavior of all quantum materials is captured in a single vector wave equation, called the Schrödinger equation:

$$\hat{\mathcal{H}} \left|\Psi(t)\right\rangle = i\hbar\frac{\partial}{\partial t}\left|\Psi(t)\right\rangle , \tag{5.1}$$

where the Hamiltonian $\hat{\mathcal{H}}$ describes the potential and kinetic energy of each electron, $|\Psi(t)\rangle$ is the time-dependent, many-body wavefunction encoding the relative amplitude and phase of each quantum state, and $\hbar$ is the reduced Plank constant. If this wave equation could be accurately solved for systems with $\sim\ 10^{24}$ particles, the entire range of interacting quantum phases would be within reach. Unfortunately, the scope of this calculation far exceeds the earth's collective computing power, so a simplification is needed to move forward.

5.1 THE CASE FOR ACOUSTICS

One approach to simplifying Eq. 5.1 is to formulate a similar equation but for a simpler system, such as acoustic waves. With optimistic eyes, Eq. 5.1 appears to already have roughly the same form as the equation governing the propagation of sound:

$$\underbrace{B(\mathbf{r})\boldsymbol{\nabla}\cdot\frac{1}{\rho(\mathbf{r})}\boldsymbol{\nabla}}_{\sim\hat{\mathcal{H}}}p(t,\mathbf{r}) = \frac{\partial^2}{\partial t^2}\underbrace{p(t,\mathbf{r})}_{\sim\Psi(t)}, \tag{5.2}$$

where $\rho(\mathbf{r})$ is the density, $B(\mathbf{r})$ is the bulk modulus, and $p(t,\mathbf{r})$ is the pressure. Here $\rho(\mathbf{r})$ and $B(\mathbf{r})$ are spatial potentials that dictate how sound moves through a medium, similar to the role played by $\hat{\mathcal{H}}$ in Eq. 5.1, whereas $p(t,\mathbf{r})$ describes the combined amplitude and phase of the acoustic waves, much like $|\Psi(t)\rangle$ does in Eq. 5.1.

At first glance, the Newtonian behavior of sound seems completely detached from the quantum motion of electrons in solids. Yet the similarity between their governing wave equations raises the hope that some of the quantum phases hidden in Eq. 5.1 have analogous acoustic solutions in Eq. 5.2, provided the mapping between these equations is defined precisely. For example, the hydrogen-like solutions of the Schrödinger equation can be directly compared to the series of acoustic standing modes in an air cavity (compare Fig. 5.1(a) and (b)). Coupling two of these modes gives

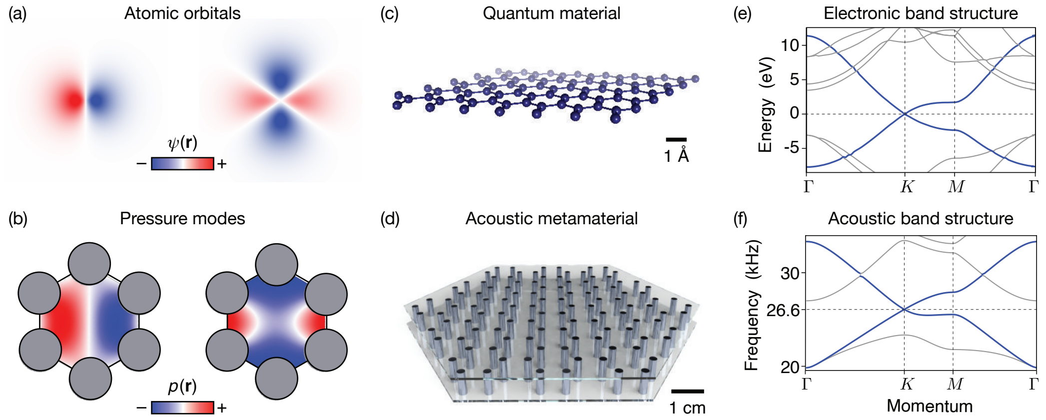

Figure 5.1: Equivalent band structures at two vastly different length scales. (**a**) The building blocks of quantum materials are the orbitals in the valence shells of constituent atoms. (**b**) The same symmetries are obeyed by the standing waves formed when sound is confined to a cavity, such as the space between these gray pillars. (**c**) The emergent behavior of quantum materials is the collective motion of many coupled orbitals in a lattice geometry. (**d**) A carefully constructed acoustic metamaterial can implement the same couplings as its quantum counterpart, implying the collective behavior is comparable in each system. (**e-f**) The resultant electronic and acoustic band structures describe the analogous motion of electrons and sound in a honeycomb lattice, despite eight orders-of-magnitude difference in their respective length scales.

the same bonding and anti-bonding eigenmodes in acoustics as it does in quantum mechanics. And by arranging enough coupled cavities in a lattice geometry, a sufficiently complex acoustic metamaterial can even mimic the emergent, collective behavior of thousands of electrons in a solid (see Fig. 5.1 (c-f)).

Concentrating on acoustic waves is certainly an appealing approach: the equations for sound are exactly solvable using finite-element methods, and new acoustic designs can be 3D printed and tested within hours. Additionally, while quantum materials are limited by discrete atom choices, acoustic metamaterials offer the possibility to explore intermediate compounds because they can be tuned continuously. They bridge the gap between discrete material platforms, allowing their emergent properties to be isolated, optimized, or combined—all of which can aid the design of future devices. Lastly, new acoustic metamaterials can be quickly converted to photonic equivalents under a simple mapping of variables [127].

Yet, the analogy between acoustics and electronics has its limitations. First, the pressure eigenmodes in acoustics are fundamentally bosonic, meaning they commute under exchange, unlike electrons. Consequently, the interactions between these modes are implemented differently from the interactions between electrons. But the non-linear extensions of the acoustic wave equation imply that some form of acoustic interactions is feasible. Besides, the commutation relations don't prevent acoustic metamaterials from accurately recreating the single-particle eigenstates of their quantum counterparts. Second, acoustic pressure fields are generally classical, but they can have parallels in the quantum limit. For example, two recent experiments demonstrated control of surface acoustic waves in the quantum limit [128, 129], and lattice geometries are a natural extension [130].

5.2 THE RISE OF ACOUSTIC METAMATERIALS

In the last few years, acoustic metamaterials have emerged as convenient testbed for a wide variety of condensed matter phenomena. Already, they have been used to successfully imitate topological insulators [131], higher-order topology [132, 133], fragile topology [134], and Weyl semi-metals [135–137]. Incredibly, these metamaterials often demonstrated by analogy the novel properties of quantum systems before those quantum materials were first synthesized! At the same time, metamaterials have contributed to the development of next-generation technology, such as invisibility cloaks [138], topological lasers [139, 140], and super-resolution ultrasound imagers [141]. These applications demonstrate that the transfer of knowledge flows both ways: acoustic metamaterials have unlocked new phases of topological quantum matter, while simultaneously translating ideas from electronics into useful acoustic devices.

In the remainder of this part of the thesis, I describe three forays into quantum mimicry that demonstrate its two-way transfer of knowledge. In chapter 6, I present the design of the first topological acoustic transistor—a switch for sound that can be controlled by a second similar switch.

In chapter 7, I describe a general design scheme for imitating van der Waals heterostructures, a vast space of quantum materials that can be combined together like Lego blocks. Finally, in chapter 8, I recreate in acoustics the novel mechanism that generates correlated insulating behavior in twisted bilayer graphene.

This chapter appears as:

Phys. Rev. Lett. **128** *015501 (2022).*

Harris Pirie, et al.

6

Topological phononic logic

TOPOLOGICAL METAMATERIALS HAVE ROBUST PROPERTIES ENGINEERED from their macroscopic arrangement, rather than their microscopic constituency. They can be designed by starting from Dirac metamaterials with either symmetry-enforced or accidental degeneracy. The latter case provides greater flexibility in the design of topological switches, waveguides, and cloaking devices, because a large number of tuning parameters can be used to break the degeneracy and induce a topological phase. However, the design of a topological logic element—a switch that can be controlled by the output of a separate switch—remains elusive. Here we numerically demonstrate a topological logic gate for ultrasound by exploiting the large phase space of accidental degeneracies in a honeycomb lattice. We find that a degeneracy can be broken by six physical parameters, and we show how to tune these parameters to create a phononic switch that transitions between a topological waveguide and a trivial insulator by ultrasonic heating. Our design scheme is directly applicable to photonic crystals and may guide the design of future electronic topological transistors.

6.1 Classical topological insulators

Topological insulators were first conceived as quantum electronic materials with an insulating bulk and conducting surface Dirac states, allowing for dissipationless charge and spin transport along their boundaries. Their central principle—the inversion of energy bands—is also present in many classical lattice systems, inspiring the design of photonic [142–144], phononic [145], and mechanical metamaterials [146–148] with topologically protected transport. These classical systems provide a platform to test ideas in topological band theory, because they are more tangibly understood than their quantum counterparts, and their governing wave equations can be solved exactly. Their robust properties have been used in many promising applications including zero- and negative-refractive-index materials [136, 149–152], cloaking [153, 154], and protected waveguides for sound and light that outperform non-topological alternatives [131, 155, 156]. A key remaining challenge is to control the topological phase in a way that allows waveguides to toggle one another, paving the way towards topological logic circuits with greater efficiency than current CMOS technology [157–159].

A general design approach to achieve the band inversion that defines a topological metamaterial is to start from a bulk Dirac state, then intentionally break the Dirac-point degeneracy to open a negative gap. This approach can be broadly divided into two methods. The first method starts from a symmetry-enforced Dirac state, such as the K-point Dirac cone in graphene-like honeycomb or triangular metamaterials, then opens a gap by breaking a symmetry of the system. In systems with broken time-reversal ($\mathcal{T}$) symmetry [160–164], the resultant topological phase is analogous to the quantum Hall effect, while those with broken inversion symmetry [165–170] can realize an analog of the quantum spin Hall effect. However, there is limited flexibility in the design of these topological phases, as they can be tuned only by a symmetry-breaking operation. On the other hand, the second method searches for the accidental degeneracy of three [127, 149, 154] or four [150, 171, 172] bands, producing a Dirac-like cone or double Dirac cones, respectively. This method gives access to a far larger set of topological phases because the accidental degeneracy can be broken by several more-accessible tuning parameters while retaining inversion and $\mathcal{T}$ symmetry. Despite the utility and flexibility of this second method, the complete space of all topological phases has yet to be mapped for any accidental degeneracy.

We start from a particular accidental bulk Dirac-point degeneracy that gives rise to a topological state analogous to a quantum spin Hall system. In a quantum spin Hall system, the protection of the Dirac point is a consequence of the spin-1/2 nature of electrons. Specifically, because $\mathcal{T}^2 = -1$ for spin-1/2 states, Kramers theorem requires a degeneracy at all $\mathcal{T}$-invariant points of the Brillouin zone. However, spin-0 phononic and spin-1 photonic systems both have $\mathcal{T}^2 = +1$, so Kramers theorem does not apply. Instead, designs typically rely on mode hybridization to form a pseudospin-1/2 subsystem, for example with the transverse electric and magnetic polarizations of light [143]. But transverse shear modes are not available in airborne acoustics, so finding an analogy of Kramers theorem is challenging. In 2012, Sakoda [171] addressed this issue and constructed a pseudospin-1/2 system using the discrete symmetries of a triangular lattice, which was adapted to longitudinal acoustic modes shortly thereafter [150, 172, 173], and subsequently demonstrated experimentally [131]. In this scheme, a lattice with C_{6v} symmetry generates an accidental degeneracy at the Γ point between doubly degenerate E_1 and E_2 modes that transform as (x, y) and $(xy, x^2 - y^2)$, denoted (p_x, p_y) and $(d_{xy}, d_{x^2-y^2})$, respectively. These doubly degenerate modes allow the formation of a pseudospin-1/2 basis, with corresponding eigenstates $p_\pm = (p_x \pm ip_y)/\sqrt{2}$ and $d_\pm = (d_{x^2-y^2} \pm id_{xy})/\sqrt{2}$. The accidental degeneracy between the $p_\pm$ and $d_\pm$ subsystems can be lifted without breaking C_{6v} symmetry, resulting in a topological phase with helical edge modes protected by a pseudo-$\mathcal{T}$ symmetry, analogous to the quantum spin Hall state [131, 165].

Here we numerically investigate the topological phase space for a Γ-point accidental degeneracy in a phononic honeycomb lattice using commercial finite-element modeling software COMSOL MULTIPHYSICS. We find a manifold of system configurations that host a bulk accidental double Dirac cone, and we demonstrate that a topological phase can be induced by gapping the Dirac node with six independent physical parameters, which collapse into a three-dimensional (3D) phase space. This vast phase space guides the design of three topological circuit elements: a static-geometry waveguide, an externally switchable device, and a universal logic gate. While we illustrate each element using phononic metamaterials, the same design principles apply to electronic and photonic metamaterials.

6.2 FORCE-TUNED TOPOLOGICAL WAVEGUIDE

A static-geometry topological waveguide is formed at the interface between a lattice with normally ordered bands and one with inverted bands. This type of waveguide was already demonstrated using two hexagonal phononic crystals of steel pillars in a fluid medium with different filling ratios, $\tilde{r} = R/a$ [131, 172], where R and a are the radius and spacing of the pillars, respectively (see inset to Fig. 6.1(b)). When the filling ratio is large, the band structure around the Γ point contains doubly degenerate $p_\pm$ modes separated from $d_\pm$ modes by a positive energy gap, $\Delta > 0$, as shown in Fig. 6.1(a). At the critical filling ratio for a steel/water system, $\tilde{r}^* = 0.371$, the four modes become accidentally degenerate and the bulk metamaterial hosts double Dirac cones. Below critical filling,

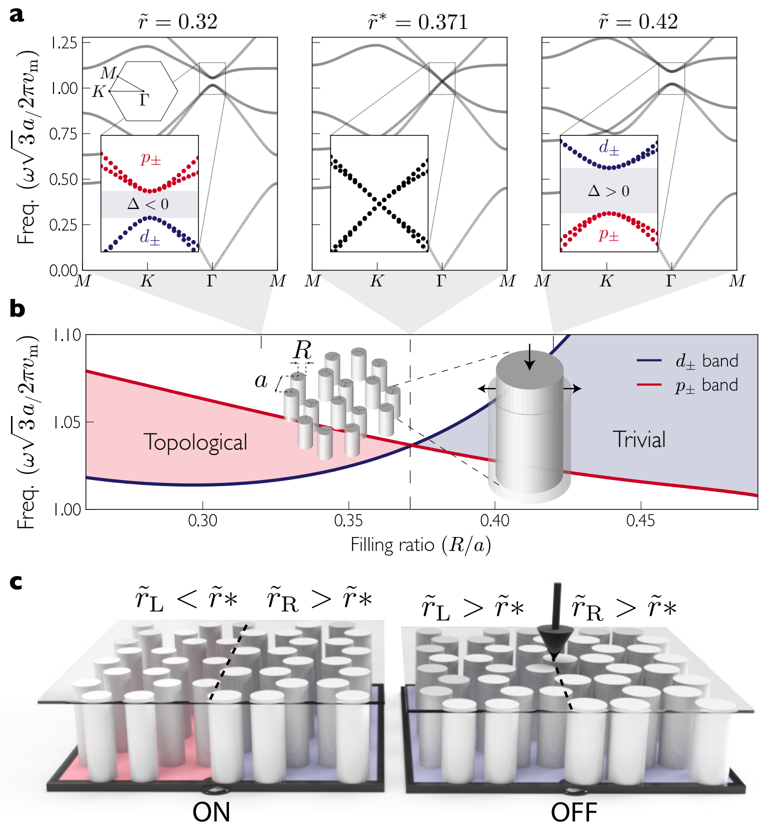

Figure 6.1: **An externally controlled topological switch for sound.** (**a**) The phononic band structure for a honeycomb lattice of steel pillars in water passes through an accidental degeneracy as the radius of the pillars is varied. This degeneracy is between $p_\pm$ bands (red) and $d_\pm$ bands (blue), and occurs at the critical filling ratio of $\tilde{r}^* \equiv R^*/a = 0.371$ (middle panel). As the filling ratio is tuned away from this value, a positive (right) or negative (left) band gap opens, leading to a topological phase transition. (**b**) This transition can be clearly seen by tracking the Γ-point eigenvalues as $\tilde{r}$ is tuned. (**c**) A topological waveguide is made by placing two lattices with $\tilde{r}_L < \tilde{r}^*$ and $\tilde{r}_R > \tilde{r}^*$ next to each other (left panel). When the pillars are compressed vertically, their radius expands such that both sides of the waveguide become trivial insulators (right panel). This device is a topological switch for sound that turns ‘off’ when compressed.

the $p_\pm$ modes have higher energy than the $d_\pm$ modes, and the band structure contains a negative energy gap, $\Delta < 0$. Topologically protected edge modes are confined to the interface between a positive- and negative-gapped material, allowing the design of topological waveguides that are pseudospin polarized and immune to defects including cavities, bends, and lattice disorder [131].

Our first advance is a new mechanism to create an externally switchable topological waveguide for sound, providing a simple alternative to the existing schemes [174–176]. In general, a topological switch hosts robust transport when 'on', but is a trivial insulator when 'off'. It requires a tuning mechanism capable of changing the sign of the band gap on the topological side, while leaving the trivial side unchanged. We found that an external vertical compression/extension can induce this behavior, as it alters the radius of pillars, which can toggle the topological phase (see inset to Fig. 6.1(b)). For materials with a positive Poisson's ratio, a topological waveguide naturally switches 'off' when compressed, once the filling ratio of its topological side increases beyond $\tilde{r}^*$, as shown in Fig. 6.1(c). In practice, rubber pillars are ideal for this application as they are far more stretchable than metal pillars, and have a higher Poisson's ratio [177]. Advancing beyond static-geometry topological waveguides [131, 155, 156, 167–170], this type of switch could be used to control passive acoustic isolation systems, but the output of one switch cannot sustain the macroscopic stretch required to activate a second, similar switch.

6.3 A TOPOLOGICAL SWITCH CONTROLLED BY ULTRASOUND

Our second, more significant advance is to design a phononically controlled acoustic switch—i.e. a topological logic element. Like electronic field-effect transistors, these switches may be connected together to form circuits. Here we rely explicitly on the flexibility granted by the large phase space of accidental degeneracies in a honeycomb metamaterial. In general, an accidental band degeneracy can be lifted by tuning any lattice parameter, as it is not protected by symmetry. The relevant parameters in a phononic lattice define the acoustic wave equation,

$$\boldsymbol{\nabla} \cdot \left[\frac{1}{\rho_r(\mathbf{r})} \boldsymbol{\nabla} p(\mathbf{r}) \right] = -\frac{\omega^2}{v_\mathrm{m}^2} \cdot \frac{p(\mathbf{r})}{v_r^2(\mathbf{r}) \rho_r(\mathbf{r})} \tag{6.1}$$

where p is the pressure, ω is the eigenfrequency, and $\rho_r(\mathbf{r}) = \rho(\mathbf{r})/\rho_\mathrm{m}$ and $v_r(\mathbf{r}) = v(\mathbf{r})/v_\mathrm{m}$ are the relative density and speed of sound, respectively. In total, there are six physical parameters that

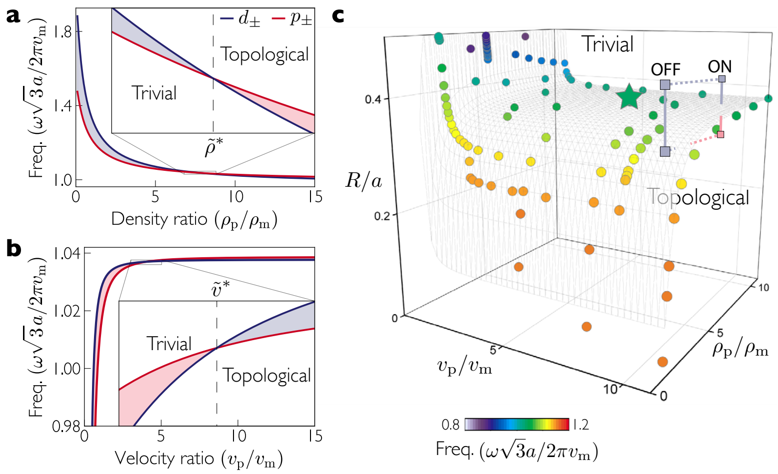

Figure 6.2: **Topological phase space for a honeycomb phononic lattice.** An accidental degeneracy between the $p_\pm$ and $d_\pm$ modes in a steel/water system (green star in (c)) can be broken by tuning the ratio of (**a**) density while holding speed of sound and radius fixed; or (**b**) speed of sound while holding radius and density fixed. (**c**) Each accidental degeneracy is a point in $(\tilde{v}, \tilde{\rho}, \tilde{r})$ space, colored according to its crossing frequency (e.g. the steel/water system has a crossing frequency of 90 kHz for $a = 1$ cm). Together, they separate phase space into a topological and a trivial region. A topological waveguide pairs configurations from different sides of this surface (see solid line labelled ON), provided their bulk spectral gaps overlap. Transmission through it can be switched 'off' by tuning to two configurations that occur on the same side of the surface (see path labelled OFF).

can tune the resulting eigenspectrum: R, a, ρ_{p}, ρ_{m}, v_{p}, and v_{m}, where the subscript refers to pillars or medium. First note that uniformly scaling ρ_{p} and ρ_{m} produces no change. Second, uniformly scaling v_{p} and v_{m} scales all eigenfrequencies of Eq. 6.1, but does not shift eigenfrequencies relative to one another, and therefore cannot alter the topological phase. We take this scaling into account by adopting dimensionless units for frequency, $\tilde{\omega} = \omega\sqrt{3}a/2\pi v_{\mathrm{m}}$. In fact, the frequency-normalized band structure depends only on three dimensionless ratios: $\tilde{r} = R/a$, $\tilde{v} = v_{\mathrm{p}}/v_{\mathrm{m}}$ and $\tilde{\rho} = \rho_{\mathrm{p}}/\rho_{\mathrm{m}}$. In the example system of steel pillars in water, we find that varying either $\tilde{v}$ or $\tilde{\rho}$ lifts the accidental degeneracy and can open a negative gap (Fig. 6.2(a-b)). More generally, varying any combination of lattice parameters along a path in $(\tilde{v}, \tilde{\rho}, \tilde{r})$ space that connects the topological phase to the trivial phase must pass through an accidental degeneracy. Consequently, there exists a surface in $(\tilde{v}, \tilde{\rho}, \tilde{r})$ space that separates the topological phase from the trivial phase, on which there is accidental degeneracy between $p_\pm$ and $d_\pm$ modes and a bulk double Dirac cone. We numerically calculated the shape of this surface, shown in Fig. 6.2(c), by recording the accidental crossing point in an $\tilde{r}$ sweep for a discrete set of $(\tilde{v},\tilde{\rho})$ points, at fixed $(v_\mathrm{m},\rho_\mathrm{m})$.

A key challenge in designing a topological switch is to preserve overlapping bulk spectral gaps before and after switching. For example, in the sweep shown in Fig. 6.2(a), increasing $\tilde{\rho}$ causes both $p_\pm$ and $d_\pm$ modes to decrease in frequency, leading to a band inversion because the $d_\pm$ modes decrease faster than the $p_\pm$ modes. Yet, this tuning parameter alone cannot be used to design a topological waveguide because at any frequency there are bulk modes in one of the two sides that mask the edge states, unlike Fig. 6.1(b). The same accidental degeneracy can be broken by varying $\tilde{v}$, which causes both $p_\pm$ and $d_\pm$ modes to increase in frequency (Fig. 6.2(b)), again precluding a usefully overlapping gap. However, an overlapping bulk gap may occur when tuning a combination of $\tilde{v}$ and $\tilde{\rho}$, for instance, in a waveguide between two sets of pillars with different materials but the same radius. In general, each accidental degeneracy on the surface in Fig. 6.2(c) can be used to construct a practical waveguide for a parameter sweep through some solid angle in $(\tilde{v},\tilde{\rho},\tilde{r})$ space. Schematically, such a waveguide combines two points in parameter space connected by a path that punctures the surface in Fig. 6.2(c). Consequently, a topological switch combines four points in phase space, with three above the surface (trivial) and one below (topological), e.g. the square points in Fig. 6.2(c). Furthermore, a useful switch requires the bulk to remain gapped and overlapping on all four $(\tilde{v},\tilde{\rho},\tilde{r})$ trajectories that connect these points, except where they pass through the surface.

To enable the output of one switch to control the next, our design for a phononically-controlled topological switch uses a temperature increase delivered by ultrasonic phonons as its tuning mechanism. Each switch contains a honeycomb lattice of steel pillars connecting the source and drain terminals, attached to a base plate made from a second material, in an air-tight container, as shown in Fig. 6.3(c). The temperature increase needed to toggle the switch is provided by a thermoacoustic converter connected to a third terminal (labelled ‘gate’ in Fig. 6.4(g-h), see [177]). The primary

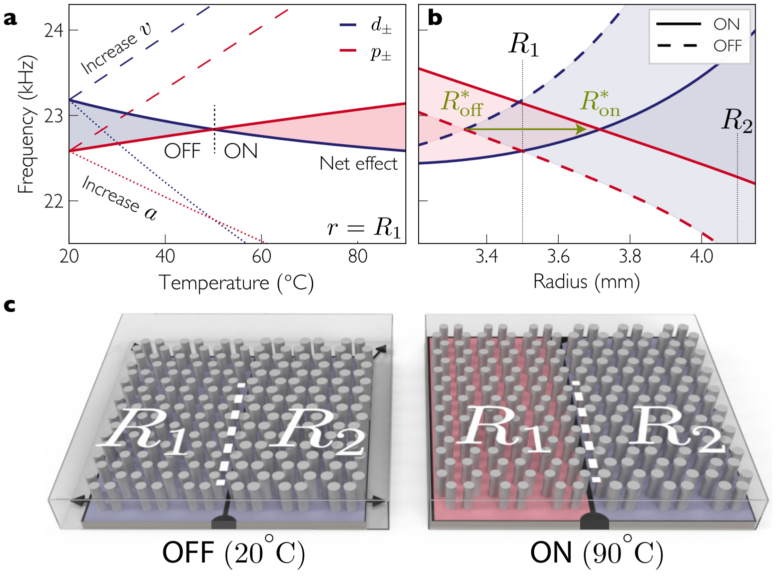

Figure 6.3: **Designing a temperature-controlled topological switch.** We consider a honeycomb lattice of steel pillars ($R_1 = 3.5$ mm, $R_2 = 4.1$ mm, $a = 8.5$ mm) anchored to a high-thermal-expansion base plate, in an air medium within a sealed fixed-size box. (**a**) Heating this system has two main competing effects: eigenfrequencies are increased by raising the speed of sound in air (dashed lines), but decreased as the base plate thermally expands (dotted lines). The latter effect also tunes $\tilde{r}$ to induce a band inversion. These two effects can be balanced by correctly choosing the thermal expansion coefficient of the base plate (here 1.61×10^{-3} K^{-1}), providing a temperature-tunable topological phase transition with an overlapping spectral gap (solid lines). (**b**) A topological switch combines two sizes of pillars: one side transitions from trivial to topological as the switch is heated (R_1), while the other remains trivial throughout (R_2). (**c**) Unlike the switch design in Fig. 6.1(c), which is triggered by tuning R at fixed a, this switch is turned 'on' by increasing a at fixed R, and can be actuated by phonon-delivered heat.

effect of heating the device is to change the speed of sound in the medium, which typically increases all eigenfrequencies of the system (see dashed lines in Fig. 6.3(a)). Second, heating causes thermal expansion of the materials, increasing both R and a, though not necessarily equally. If the base plate and pillar materials are selected such that a increases faster than R, the net result is to reduce all eigenfrequencies of the system and induce a band inversion (dotted lines in Fig. 6.3(a)). Finally, heating alters the density of the air and the materials, which has been taken into account, but is insignificant. The first two effects can be balanced to maintain a bulk gap throughout the switching process, by fixing the ratio v_m/a that appears in the eigenfrequency of Eq. 6.1. Because the base plate expands linearly with temperature, we seek a medium where v_m also increases linearly. For an ideal gas at temperature T, v_{m} increases as $\sqrt{T}$, but the trend is almost linear near room temperature; as such, air is a suitable medium. Consequently, to keep v_{m}/a fixed as the temperature increases from T_i to T_f, we seek a base material with a coefficient of thermal expansion given by $\alpha = 1/(T_i + \sqrt{T_i T_f})$. For the proof-of-principle switch shown in Fig. 6.3(b), the required baseplate thermal expansion coefficient is $1.61 \times 10^{-3}\ \mathrm{K}^{-1}$, which is within the range achievable by origami metamaterials [178]. Alternatively, we empirically demonstrated an even larger effective thermal expansion coefficient by thermally actuating using the shape-memory alloy Nitinol [177].

The advantage of a topological phononic switch can be seen from the finite-sized calculations in Fig. 6.4. Unlike a trivial waveguide, which experiences significant losses induced by disorder and bends (Fig. 6.4(a-b)), the topological switch acts as a robust pseudospin-dependent waveguide when 'on' due to a Dirac cone between the two sides (Fig. 6.4(c-d)). As it is cooled, the pillars contract around the input terminal; both sides become trivially insulating and block transmission, turning the switch 'off' (Fig. 6.4(e-f)). Our topological switch is stable against mild temperature changes provided its operational frequency remains within the spectral gap (see Fig. 6.3(a)). Such temperature variations alter only the localization of the edge states, not their presence or absence [177].

6.4 BUILDING A UNIVERSAL LOGIC GATE FOR ULTRASOUND

Our proof-of-principle temperature-controlled phononic switches can be linked to form a universal NAND gate with two main segments. First, we design a topological AND gate by connecting two switches in series (Fig. 6.4(g)). This device requires both control signals (A and B) to be 'on' to heat each switch and allow information to propagate [177]. Second, to design a topological NOT gate, we utilize a base plate material that has a negative coefficient of thermal expansion; that is, it shrinks when heated. At room temperature (control is 'off'), the NOT gate is a topological waveguide that transmits information, but when the control is 'on', the device heats and shrinks, transitioning to

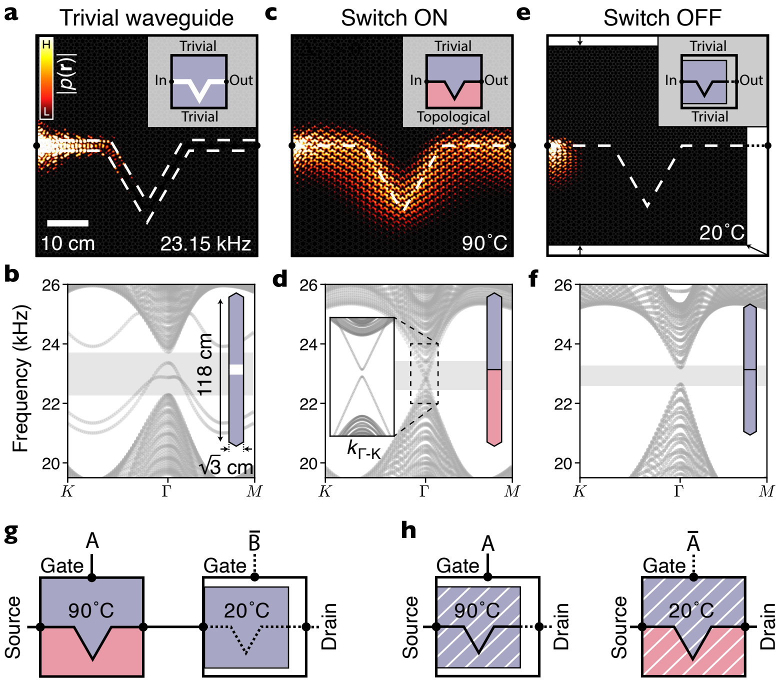

Figure 6.4: **Topological logic gates with ultrasound.** (**a**) Transmission through a trivial waveguide, like this channel in an insulating steel/air phononic crystal, is disrupted by disorder and bends. (**b**) The band structure of the corresponding supercell (see inset) contains a bulk gap with trivial edge states. (**c**) In contrast, a topological waveguide with the same parameters as in Fig. 3, allows robust transport regardless of channel geometry; it can be used as the 'on' state of a topological switch. (**d**) Its band structure hosts protected, Dirac-like edge states (inset) due to a negative bulk gap on one side. (**e**) When the system is cooled, it contracts and both sides become trivial insulators, preventing transmission. (**f**) Excitations at frequencies within the gap decay exponentially as they enter the device. (**g**) A topological AND gate, constructed from two switches in series, requires both control signals (A and B) to be high to register an output. (**h**) A topological NOT gate uses a base plate with a negative thermal expansion coefficient; it contracts to turn 'off' when heated (left), and expands to turn 'on' when cooled (right).

a trivial insulator. To maintain an overlapping bulk gap throughout this transition, we require a medium where the speed of sound decreases with increasing temperature, a behavior commonly observed in oils [179]. Specifically, a device using steel pillars in sunflower oil requires a coefficient of thermal expansion of $-2.0 \times 10^{-3}\ \mathrm{K}^{-1}$ to keep the ratio v_m/a fixed, a value recently demonstrated [178].

The design of topological metamaterials based on a broken accidental degeneracy is extremely versatile due to the large number of tuning parameters available. Specifically, for a phononic honeycomb lattice, the topological phase can be tuned by six independent parameters, which collapse onto a 3D phase space. This phase space guided a proof-of-principle design for a phononically controlled topological switch, the building block of an acoustic logic gate. The macroscopic size and moderate speed of our device makes it an ideal tool for teaching and understanding topological materials. More importantly, the same design process can be followed for piezoelectric materials at mesoscopic length scales, enabling switchable control of topologically protected surface-acoustic waves for integrated phononics [180]. Finally, our approach directly applies to optical systems under a simple mapping of variables [127], or to nano-structured quantum materials [181], providing a new direction for developing a field-effect topological transistor.

This chapter appears as:

Phys. Rev. B **101** *121103(R) (2020)*.

William Dorrell, Harris Pirie, et al.

7

van der Waals metamaterials

The van der Waals heterostructures are an active frontier for discovering emergent phenomena in condensed matter systems. They are constructed by stacking elements of a large library of two-dimensional materials that couple together through van der Waals interactions. However, the number of possible combinations within this library is staggering, so fully exploring their potential is a daunting task. Here we introduce van der Waals metamaterials to rapidly prototype and screen their quantum counterparts. These layered metamaterials are designed to reshape the flow of ultrasound to mimic electron motion. In particular, we show how to construct analogues of all stacking configurations of bilayer and trilayer graphene through the use of interlayer membranes that emulate van der Waals interactions. By changing the membrane's density and thickness, we can also reach coupling regimes far beyond that of naturally occurring graphene. We anticipate that van der Waals metamaterials can be used to explore, extend, and inform future electronic devices. Furthermore, they allow the transfer of useful electronic behavior to acoustic systems, such as flat bands in magic-angle twisted bilayer graphene, which may aid the development of super-resolution ultrasound imagers.

7.1 INTRODUCTION

The recent excitement surrounding van der Waals (vdW) heterostructures stems from the diverse emergent phenomena that can arise by layering two-dimensional (2D) materials like graphene and other xenes, or transition metal dichalcogenides [182–184]. Such vdW heterostructures are poised to contribute to transformative technologies including ultra-thin low-energy transistors [185], photodetectors [186], and light-emitting diodes [187]. Recently, their capabilities were expanded to include exotic many-body quantum behaviors such as unconventional superconductivity, which can occur in twisted bilayer graphene (TBG) [188, 189]. However, finding the most interesting systems and behaviors is a time-consuming task, given the countless stacking combinations afforded by the ever-increasing library of 2D materials and tuning parameters such as twist angle. Twist angle is a particularly exciting but challenging new parameter, because the small 'magic angle' of 1.18° that gives rise to such exotic effects in TBG also presents forbidding computational difficulties due to the increased unit cell size. An open problem is to develop a method for rapidly predicting and prototyping vdW heterostructures to create a tight feedback loop for their technological advancement.

In the last few years, phononic metamaterials have emerged as a promising platform for mimick-

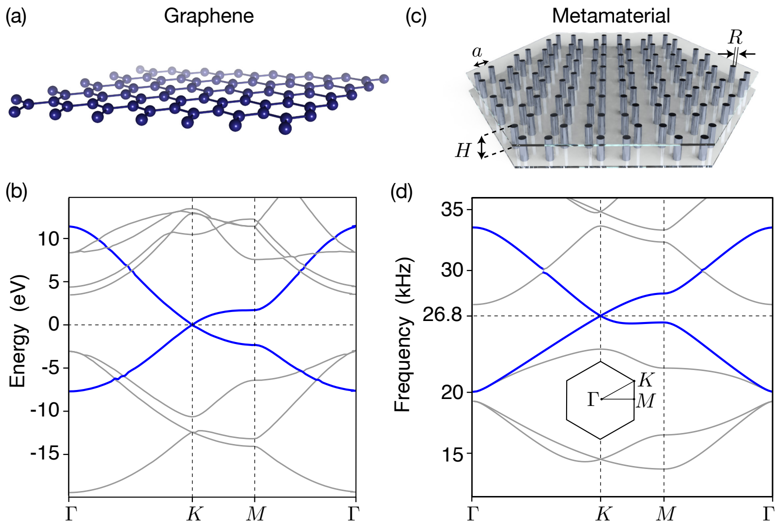

Figure 7.1: Phononic metamaterial analogue of graphene. (**a**) In graphene, the honeycomb lattice symmetry leads to (**b**) a band structure featuring a linearly dispersive K-point Dirac cone (blue), adapted from Ref. [190]. (**c**) We designed a phononic metamaterial to imitate graphene by arranging a honeycomb lattice of steel pillars in air. The pillars have radius $R = 0.32$ cm, height $H = 0.1$ cm, and spacing $a = 1$ cm. (**d**) Their simulated phononic band structure recreates the Dirac cone in graphene (blue).

ing condensed matter systems [131, 147, 164, 191, 192]. They are appealing quantum analogues because their governing wave equations are straightforward, making calculations fast; they can be quickly fabricated; and their properties derive from macroscopic structures with continuously tunable geometry, as opposed to the limited discrete elements of the periodic table. A carefully constructed phononic metamaterial can host propagating sound waves that closely resemble the behavior of electrons moving in solids. For example, the Dirac-like electronic bands of graphene, which rely on the C_6 symmetry of its honeycomb carbon lattice (Fig. 7.1(a-b)), can be reproduced in the phonon band structure of a honeycomb arrangement of steel pillars in air (Fig. 7.1(c-d)). This general framework has been applied to yield analogues of graphene in longitudinal phononics [127, 193], surface acoustics [130], photonics [194], and mechanics [192, 195]. Given these successes, it is natural to ask whether the same strategy works for multi-layer systems. Existing metamaterial designs have made innovative use of multi-layer structures [196, 197], including recent work that coupled two-layered sonic crystals to create topological phases [198]. These findings represents important steps towards mimicking multi-layer heterostructures. However, without control of the strength of interlayer coupling, accurately recreating the diverse library of vdW heterostructures remains an elusive goal.

Here we demonstrate a versatile framework for mimicking layered vdW heterostructures with acoustic metamaterials. Specifically, we numerically explore the coupling strength of an interlayer membrane as a function of material properties using the commercial finite-element modeling software COMSOL MULTIPHYSICS. By tuning the membrane properties, we discover a simple phenomenological model for metamaterial interlayer coupling that allows us to recreate all stacking configurations of bilayer and trilayer graphene, and furthermore to reach coupling regimes far beyond those in naturally occurring graphene. Our work opens a different path to explore vdW heterostructures, which could uncover new phenomena and inform the fabrication of future quantum materials. In the opposite direction, our work guides the translation of electronic vdW phenomena to phononic systems, which could stimulate useful acoustic devices.

7.2 PHONONIC BILAYER GRAPHENE

Building on previous work, we started from a monolayer phononic metamaterial designed to emulate the Dirac cone in graphene [4, 131, 172]. The presence of a Dirac cone relies only on the C_6 symmetry of the unit cell, but its shape can be tuned by material choice and pillar size. For convenience, our device consists of a honeycomb lattice of steel pillars in air, as shown in Fig. 7.1(c). We calculated its band structure for various configurations of pillar radius (R), height (H), and spacing (a), and found a close match to graphene when $R = 0.32$ cm, $H = 0.1$ cm, and $a = 1$ cm (Fig. 7.1(d)). Importantly, our metamaterial contains an isolated Dirac cone like graphene, despite small differences in the surrounding bands. Consequently, for frequencies close to 26.8 kHz our

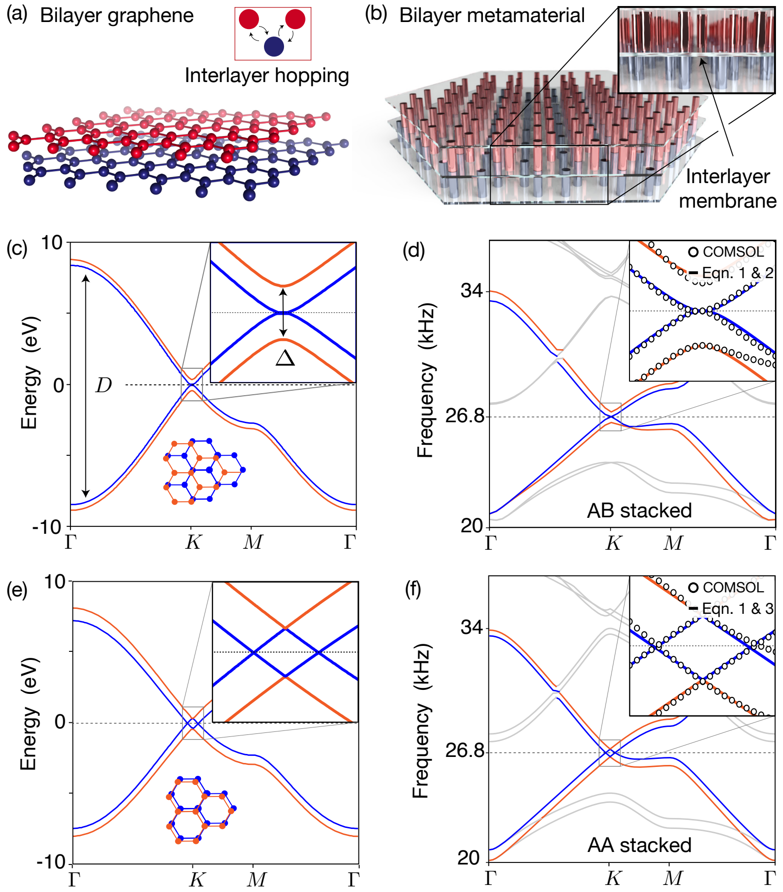

Figure 7.2: Phononic metamaterial analogue of bilayer graphene. (**a**) We recreated interlayer hopping in bilayer graphene using (**b**) two layers of honeycomb metamaterial separated by a flexible membrane. (**c**) In AB-stacked bilayer graphene, the Dirac cones hybridize to create a 'kissing' band structure. (**d**) With an interlayer membrane made of 0.19-mm thick HDPE, the same effect is seen in our bilayer metamaterial. This effect is well described by the same tight-binding Hamiltonian used to describe bilayer graphene (inset). (**e**) In AA-stacked bilayer graphene, the structure of the Dirac cone changes. (**f**) By stacking our metamaterial in the AA configuration, it accurately captures the AA graphene Dirac cone structure. Panels (c) and (e) are tight-binding calculations reprinted with minimal alterations from Ref. [199], with permission from Elsevier.

acoustic device responds similarly to undoped graphene.

Our first advance is to demonstrate a phononic analogue of bilayer graphene by stacking two honeycomb metamaterials on top of each other. In its natural state, bilayer graphene stacks in an AB configuration (Fig. 7.2(a)). Each layer contributes an identical Dirac cone, $E(\mathbf{k})$, to the band structure. The two Dirac cones then couple through interlayer hopping, Δ, to generate a characteristic band structure whereby the linear Dirac cones are replaced by parabolic 'kissing' bands [199] (Fig. 7.2(c)). The combined structure can be described by a simple tight-binding Hamiltonian [199, 200],

$$\mathcal{H}(\mathbf{k}) = \begin{bmatrix} E(\mathbf{k}) & \delta \\ \delta^T & E(\mathbf{k}) \end{bmatrix}, \text{ where } E(\mathbf{k}) = \begin{bmatrix} 0 & v_\mathrm{F}\mathbf{k} \\ v_\mathrm{F}\mathbf{k} & 0 \end{bmatrix}, \tag{7.1}$$

$$\delta = \delta_{AB} = \frac{1}{2} \begin{bmatrix} 0 & 0 \\ \Delta & 0 \end{bmatrix}, \tag{7.2}$$

and v_F is the Fermi velocity. In this model, $E(\mathbf{k})$ describes hopping between sublattice sites within a single layer, while δ_{AB} describes the first-order interlayer coupling, which always occurs between inequivalent sub-lattice sites and so contributes an off-diagonal term. To compare the magnitude of graphene's interlayer hopping to that in our metamaterial, we used a dimensionless coupling metric, $\widetilde{\Delta} = \Delta/D$, where D is the Dirac-cone bandwidth. In bilayer graphene, $\widetilde{\Delta} = 4.7\%$ based on tight-binding fits to experimental data and *ab initio* calculations (see Fig. 7.2(c) and Ref. [199]).

Our metamaterial analogue of bilayer graphene controllably couples phonons between layers through the use of an intermediary membrane (Fig. 7.2(b)). Intuitively, as phonons in one layer propagate, they induce matching oscillations in the membrane, which links to the other layer and promotes the desired layer-to-layer crosstalk. To achieve a similar coupling magnitude as in bilayer graphene, we used a 0.19-mm thick sheet of high-density polyethylene (HDPE) as the intermediary layer. We computed the phononic band structure of our bilayer metamaterial using COMSOL

MULTIPHYSICS (open circles in Fig. 7.2(d)). All simulations contain additional 0.19-mm thick HDPE sheets on the outer edges to confine the modes to the 2D layers. Strikingly, we found 'kissing' bands in the bilayer metamaterial, analogous to those in bilayer graphene. Furthermore, the phononic bands are well described by the same tight-binding model (Eqn. 7.1 and 7.2, solid lines in Fig. 7.2(d)) with reasonable values for the sound velocity $v_s = 140$ m/s (analogous to v_F in graphene) and phonon bandwidth $\Delta = 700$ Hz, yielding $\widetilde{\Delta} = 4.7\%$. Thus, the intermediary HDPE sheet quantitatively reproduces the interlayer hopping in bilayer graphene.

The first key advantage of vdW metamaterials is the versatility of their stacking configuration. In bilayer graphene, stacking arrangements other than AB host a rich range of physical phenomena [188, 201]. Yet non-AB stacking is technically challenging to fabricate in graphene, which tends to relax locally back to AB, making it especially difficult to isolate and empirically confirm a particular uniform configuration. On the other hand, constructing translated or twisted metamaterials presents no additional difficulty, allowing analogues of quantum electronic phenomena to be rapidly and unambiguously explored. To illustrate this point, we recreated the band structure of AA-stacked bilayer graphene by translating our AB-stacked metamaterial, but retaining the same HDPE interlayer (Fig. 7.2(e-f)). The band structure is well described by the tight-binding Hamiltonian in Eqn. 7.1, but with a modified coupling matrix that instead encodes interlayer hopping between vertically-aligned, identical sub-lattice sites:

$$\eth = \eth_{AA} = \frac{1}{2}\begin{bmatrix} \Delta & 0 \\ 0 & \Delta \end{bmatrix}. \tag{7.3}$$

This model accurately describes both the phononic and electronic AA-stacked systems, as shown in the insets to Fig. 7.2(e-f). In addition, it captures the behavior of both AA-stacked and AB-stacked metamaterials using the same values of v_F and Δ, simply by switching the $\eth$ matrix.

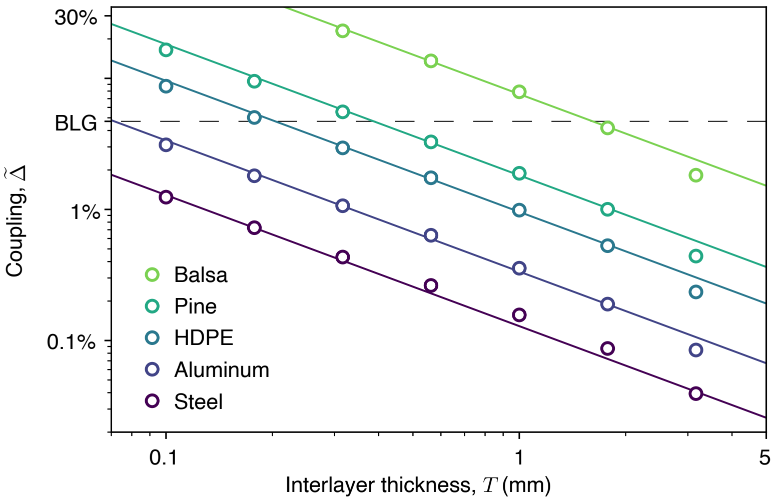

Figure 7.3: Interlayer coupling is controllable over two orders of magnitude. The computed dimensionless coupling strength ($\widetilde{\Delta}$, open circles) varies inversely with interlayer density (ρ) and thickness (T): $\widetilde{\Delta} = \Delta/D \propto 1/(\rho T)$ (solid lines), where Δ is the interlayer hopping and D is the bandwidth. With common materials, it is possible to engineer interlayer coupling to be an order of magnitude larger or smaller than in natural bilayer graphene (4.7%, dashed line).

The second key advantage of vdW metamaterials is the ease with which membrane properties can be changed to explore diverse coupling regimes. In electronic vdW heterostructures, the interlayer coupling is often seen as a fixed property, and experiments that vary it are technically challenging. For instance, a substantial vertical pressure of 1.3 GPa is required to effect just a 20% increase in the interlayer coupling strength of TBG by pushing the layers closer together [202]. Yet, this additional tuning knob has permitted some remarkable discoveries; for example, pressure increases the magic angle and the superconducting transition temperature in TBG [202, 203]. In our system, tuning the interlayer coupling is as simple as using a thicker membrane or changing its composition. Intuitively, the same pressure variation causes a flexible membrane to move more than a stiff membrane, so the interlayer coupling increases as the membrane becomes thinner or less dense. We computed the band structure of our AB-stacked bilayer metamaterial to quantify $\widetilde{\Delta}$ as a function of thickness for five different membrane materials, as shown in Fig. 7.3. We found that $\widetilde{\Delta}$ was largely independent of the interlayer membrane's speed of sound over a wide range of values. For example, an artificial order-of-magnitude increase in the speed of sound of the HDPE membrane in Fig. 7.2(b), without altering its density (ρ) or thickness (T), produced only a minimal change in $\widetilde{\Delta}$ from 4.7% to 4.6%. To a good approximation, $\widetilde{\Delta}$ varies inversely with ρ and T following the phenomenological rule:

$$\widetilde{\Delta} \equiv \frac{\Delta}{D} \propto \frac{1}{\rho T}. \tag{7.4}$$

These strong dependencies make it possible to vary $\widetilde{\Delta}$ over more than two orders of magnitude using only common household materials, like steel or wood. Thus, candidate twistronic materials can be categorized based on their intralayer and interlayer coupling strengths, then prototyped as simple phononic metamaterials by adjusting the pillar and membrane properties. In addition, the interlayer thickness could be spatially textured to capture variations in coupling strength due to the inherent lattice corrugation or relaxation in many vdW heterostructures, including twisted bilayer graphene [183, 204–206].

7.3 Towards Full vdW Heterostructures

Our interlayer coupling scheme generalizes beyond bilayer metamaterials. Quantum vdW heterostructures combine elements from a vast library of 2D materials to realize emergent behavior that further diversifies as the number of layers increases. To demonstrate this trend in vdW metamaterials, we simulated an analogue of trilayer graphene by stacking three honeycomb lattices of steel pillars, interspersed with the same HDPE membranes used previously (Fig. 7.4(a)). Trilayer graphene has three possible stacking configurations, each encoded by a different interlayer hopping matrix, ∂. In each case, we engineered a similarly-stacked trilayer metamaterial with interlayer interactions that promote a nearly identical band structure to trilayer graphene, as shown in Fig. 7.4(b-c). Both the electronic and phononic system can be described by the same tight-binding Hamiltonian, which is a simple extension of Eqn. 7.1,

$$\mathcal{H}(\mathbf{k}) = \begin{bmatrix} E(\mathbf{k}) & \delta_1 & 0 \\ \delta_1^T & E(\mathbf{k}) & \delta_2 \\ 0 & \delta_2^T & E(\mathbf{k}) \end{bmatrix}, \tag{7.5}$$

where the stacking-dependent δ matrices are

$$\delta^{(1)}_{AAA} = \delta^{(2)}_{AAA} = \frac{\delta_{AA}}{\sqrt{2}}, \tag{7.6}$$

$$\delta^{(1)}_{ABA} = \frac{\delta_{AB}}{\sqrt{2}}, \qquad \delta^{(2)}_{ABA} = \frac{\delta^T_{AB}}{\sqrt{2}}, \tag{7.7}$$

$$\delta^{(1)}_{ABC} = \delta^{(2)}_{ABC} = \frac{\delta_{AB}}{\sqrt{2}}. \tag{7.8}$$

Unlike their quantum counterparts, vdW metamaterials can be tuned continuously to span a large space of band structures. Although we have focused primarily on analogues of graphene, parallels to other vdW materials can be easily drawn by tuning the geometry and composite materials of the metamaterial. For example, hexagonal boron nitride (hBN) is a common ingredient in many vdW heterostructures because it hosts a large insulating band gap [208]. It consists of two interpenetrating triangular lattices of boron and nitrogen, and consequently breaks the C_6 symmetry of the unit cell to open a gap at the K point. Similarly, an analogue of hBN can be produced by breaking the C_6 symmetry of the graphene metamaterial in Fig. 7.1(c), for example by using pillars of different radii. Unlike the electronic version, the resulting band gap in the metamaterial can be continuously tuned because the radii may be chosen arbitrarily. Single-layer metamaterials exhibiting such wide band gaps have been extensively explored in the literature [209]. Our coupling scheme allows them to be incorporated into vdW metamaterials, affording enormous flexibility in recreating,

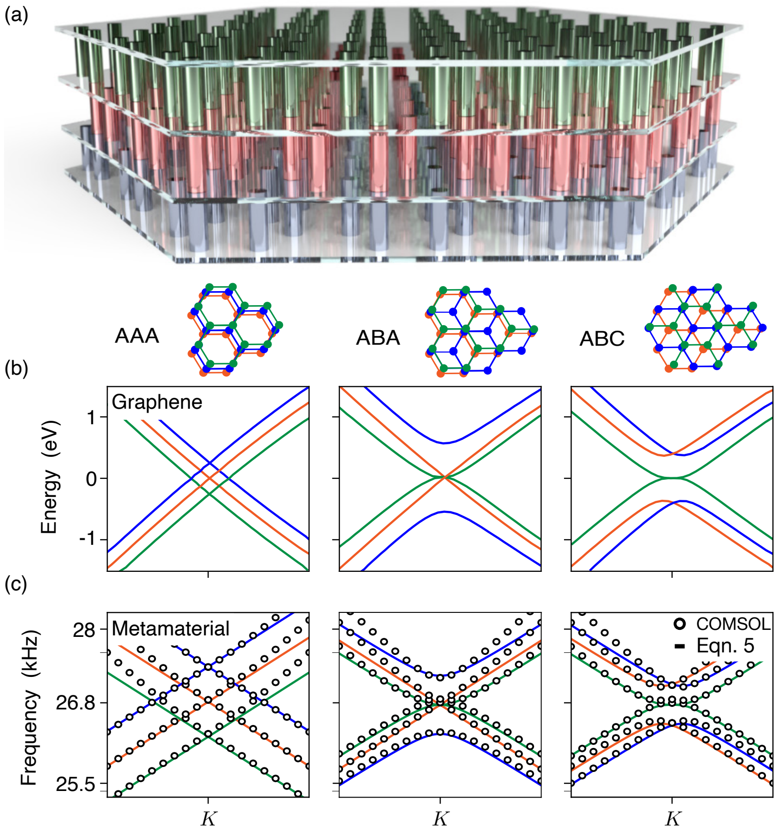

Figure 7.4: Phononic metamaterial analogue of trilayer graphene. **(a)** Our trilayer phononic metamaterial comprises three honeycomb lattices of steel pillars separated by 0.19-mm thick HDPE layers. **(b)** The Dirac cone structure of trilayer graphene displays qualitatively different behavior in each of its three different stacking configurations, adapted with permission from Ref. [207]. Copyright 2017, American Chemical Society. **(c)** Each behavior is recreated in a trilayer metamaterial by matching the stacking pattern. The calculated band structure (open circles) is well described by a simple two-parameter Hamiltonian (Eqn. 7.5, solid lines).

exploring, and extending the emergent electronic phenomena of quantum vdW heterostructures.

7.4 CONCLUSIONS

The essential ingredient of vdW heterostructures—their interlayer coupling—extends beyond electronic systems. By adding a flexible membrane between phononic metamaterials, we demonstrated that this coupling can be accurately recreated in acoustics. The resultant vdW metamaterials permit the rapid exploration of diverse stacking combinations and extensive coupling regimes that are challenging to reach in electronic materials. To illustrate their potential, we developed macroscopic acoustic analogues of every stacking configuration of bilayer and trilayer graphene. Our results provide a guide for designer vdW metamaterials, which may focus and inform future vdW-based electronic devices. Conversely, they permit mapping intriguing electronic phenomena to phononics, like the flat bands in magic-angle TBG, which may provide a new platform for non-linear acoustics. Finally, our design scheme applies directly to photonic metamaterials through a simple mapping of variables [127].

This chapter appears as:

2D Mater. **8** *031002 (2021)*.

S. Minhal Gardezi, Harris Pirie, et al.

8

Simulating twistronics with acoustic metamaterials

Twisted van der Waals (vdW) heterostructures have recently emerged as a tunable platform for studying correlated electrons. However, these materials require laborious and expensive effort for both theoretical and experimental exploration. Here we numerically simulate twistronic behavior in acoustic metamaterials composed of interconnected air cavities in two stacked steel plates. Our classical analog of twisted bilayer graphene perfectly replicates the band structures of its quantum counterpart, including mode localization at a magic angle of 1.12°. By tuning the thickness of the interlayer membrane, we reach a regime of strong interlayer tunneling where the acoustic magic angle appears as high as 6.01°, equivalent to applying 130 GPa to twisted bilayer graphene. In this regime, the localized modes are over five times closer together than at 1.12°, increasing the strength of any emergent non-linear acoustic couplings.

8.1 TWISTRONICS VASTLY EXPANDS THE VDW PHASE SPACE

Van der Waals (vdW) heterostructures host a diverse set of useful emergent properties that can be customized by varying the stacking configuration of sheets of two-dimensional (2D) materials, such as graphene, other xenes, or transition-metal dichalcogenides [182–184, 210]. Recently, the possibility of including a small twist angle between adjacent layers in a vdW heterostructure has led to the growing field of twistronics [211]. The twist angle induces a moiré pattern that acts as a tunable potential for electrons moving within the layers, promoting enhanced electron correlations when their kinetic energy is reduced below their Coulomb interaction. Even traditional non-interacting materials can reach this regime, as exemplified by the correlated insulating state in twisted bilayer graphene [188]. Already, vdW heterostructures with moiré superlattices have led to new platforms for Wigner crystals [212], interlayer excitons [213–215], and unconventional superconductivity [189, 202, 216]. But the search for novel twistronic phases is still in its infancy and there are countless vdW stacking and twisting arrangements that remain unexplored. Theoretical investigations of these new arrangements are limited by the large and complex moiré patterns created by multiple small twist angles. Meanwhile, fabrication of vdW heterostructures is restricted to the symmetries and properties of the few freestanding monolayers available today. It remains pressing to develop a more accessible platform to rapidly prototype and explore new twistronic materials to accelerate their technological advancement.

The development of acoustic metamaterials over the last few years has unlocked a compelling platform to guide the design of new quantum materials [217]. Whereas quantum materials can be difficult to predict and fabricate, acoustic metamaterials have straightforward governing equations, continuously tunable properties, fast build times, and inexpensive characterization tools, making them attractive testbeds to rapidly explore their quantum counterparts. Sound waves in an acoustic metamaterial can be reshaped to mimic the collective motion of electrons in a crystalline solid. These acoustic devices can recreate many phenomena seen in quantum materials, such as chiral Landau levels [218], higher-order topology [132, 133], and fragile topology [134]. In vdW systems, the Dirac-like electronic bands in graphene have been mimicked using longitudinal acoustics [127, 191, 193], surface acoustic waves [130], and mechanics [192, 195]. Further, it was recently discovered that placing a thin membrane between metamaterial layers can reproduce the coupling effects of vdW forces, yielding acoustic analogs of bilayer and trilayer graphene [5, 198]. The inclusion of a twist angle between metamaterial layers has the potential to further expand their utility. In addition to electronic systems, moiré engineering has recently been demonstrated in systems containing vibrating plates [219], spoof surface-acoustic waves [220], and optical lattices [221]. However, without simultaneous control of in-plane hopping, interlayer coupling, and twist angle, rapidly prototyping next-generation twistronic devices using acoustic metamaterials remains an elusive goal.

Here we propose a simple acoustic metamaterial that precisely recreates the band structure of twisted bilayer graphene, including mode localization at a magic angle of 1.12°. We start with a monolayer acoustic metamaterial that implements a tight-binding model describing the low-energy band structure of graphene. By combining two of these monolayers with an intermediate polyethylene membrane, we numerically simulate both stacking configurations of *untwisted* bilayer graphene using finite-element modeling software, COMSOL MULTIPHYSICS. Our simulated acoustic analog of *twisted* bilayer graphene hosts flat bands at the same magic angle of $\sim 1.1^{\circ}$ as its quantum counterpart [188, 222]. A key advantage of our metamaterial is the ease with which it reaches coupling conditions beyond those feasible in atomic bilayer graphene. By tuning the thickness of the interlayer membrane, we design new metamaterials that host flat bands at several magic angles between 1.12° and 6.01°. Our results demonstrate the potential for acoustic vdW metamaterials to precisely simulate and explore the ever-growing number of quantum twistronic materials.

8.2 Using air cavities as atoms

We begin by introducing a general framework for designing acoustic metamaterials to prototype non-interacting electronic materials that are well described by a tight-binding model. In our metamaterial, each atomic site is represented by a cylindrical air cavity in a steel plate (see Fig. 8.1(a)). The radius of the air cavity determines the eigenfrequencies of its ladder of acoustic standing modes. In a lattice of these cavities, the degenerate standing modes form narrow bands, separated from each other by a large frequency gap. We focus primarily on the lowest, singly degenerate *s* band. Just as electrons hop from atom to atom in an electronic tight-binding model, sound waves propagate from cavity to cavity in our acoustic metamaterial through a network of tunable thin air channels. This coupling is always positive for *s* cavity modes, but either sign can be realized by starting with higher-order cavity modes [223]. Because sound travels much more easily through air than through steel, these channels are the dominant means of acoustic transmission through our metamaterial. They allow nearest- and next-nearest-neighbor coupling to be controlled independently by varying the width or length of separate air channels, providing a platform to implement a broad class of tight-binding models.

To recreate bilayer graphene in an acoustic metamaterial, we started from a honeycomb lattice of air cavities, with radius of 3.5 mm and a separation of 10 mm, in a 1-mm-thick steel sheet, encapsu-

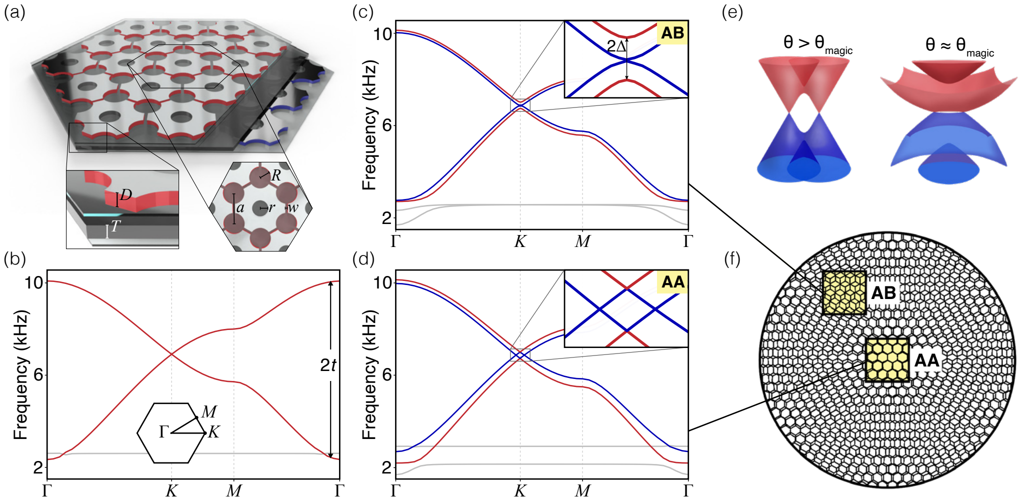

Figure 8.1: Acoustic vdW metamaterials. (a) In this acoustic metamaterial, sound waves propagate through connected air cavities in solid steel to mimic the way that electrons hop between carbon atoms in bilayer graphene. Our metamaterial design has cavity spacing $a = 10$ mm, cavity radius $R = 3.5$ mm, channel width $w = 0.875$ mm, and steel thickness $D = 1$ mm. The smaller, unconnected cavities in the center of each unit cell improve the interlayer coupling of our bilayer metamaterial, but they do not act as additional lattice sites. (b) The C_6 symmetry of the lattice protects a Dirac-like crossing at the K point of the calculated monolayer acoustic band structure. (c-d) Two sheets of acoustic graphene coupled by an interlayer polyethylene membrane of thickness $T = 2.35$ mm accurately recreate the AB and AA configurations of bilayer graphene, as shown in these calculations. (e) As the two sheets are twisted relative to one another, the two Dirac cones contributed by each layer hybridize, ultimately producing a flat band at small twist angles. (f) The twisted bilayer heterostructure has its own macroscopic periodicity with distinct AB and AA stacking regions.

lated by 1-mm-thick polyethylene boundaries. Each cavity is coupled to its three nearest neighbors using 0.875-mm-wide channels, giving an *s*-mode bandwidth of $2t = 7.8$ kHz (see Fig. 8.1(b)). This *s* manifold is well isolated from other higher-order modes in the lattice, which appear above 25 kHz. The C_6 symmetry of our metamaterial ensures a linear crossing at the K point, similar to the Dirac cone in graphene [190]. The frequency of this Dirac-like crossing and other key aspects of the band structure are controlled by the dimensions of the cavities and channels. Building on previous work, we coupled two layers of acoustic graphene together using a thin interlayer membrane [5]. By laterally translating the stacking configuration, the same acoustic metamaterial mimics both the parabolic touching around the K point seen in AB-stacked bilayer graphene, and the offset Dirac bands seen in AA-stacked bilayer graphene [200, 201], as shown in Fig. 8.1(c-d). The frequency span between the K-point eigenmodes is twice the interlayer coupling strength Δ, which is set by the interlayer membrane thickness [5]. We found that a 2.35-mm-thick polyethylene membrane (density 950 kg/m^3 and speed of sound 2460 m/s) accurately matched the dimensionless coupling ratio $\Delta/t \approx 5\%$ in bilayer graphene.

8.3 ACOUSTIC MAGIC ANGLES

Introducing a twist angle between two graphene layers creates a moiré pattern that grows in size as the angle decreases. At small angles, the Dirac cones from each layer are pushed together and hybridize due to the interlayer coupling [224, 225], as shown in Fig. 8.1(e). Eventually, they form a flat band with a vanishing Fermi velocity (v_F) at a so-called magic angle [188, 222, 226], see Fig. 8.2(a). We searched for the same band-flattening mechanism by introducing a commensurate-angle twist to our acoustic bilayer graphene metamaterial. Strikingly, our metamaterial mimics its quantum counterpart even down to the magic angle, producing acoustic flat bands at 1.12°, as shown in Fig. 8.2(a-b). Importantly, there are no other acoustic bands near the Dirac point that can fold and interfere with these flat bands (see Fig. 8.1(b)). The flat bands appear upside down in our acoustic model because its interlayer coupling (between s cavity modes) has the opposite sign from graphene's (between p_z orbitals). However, this asymmetry is quite small and its influence is not generally noticeable at higher angles [222, 227]. Our acoustic flat bands correspond to real-space pressure modes that are primarily located on the AA region, see Fig. 8.2(c). This AA localization agrees with calculations of the local electronic density of states in magic-angle twisted bilayer graphene [188, 228]. In our acoustic system, these localized modes represent sound waves that propagate with a low group velocity of 0.05 m/s, compared to 30 m/s in the untwisted bilayer.

The magic angle of twisted bilayer graphene can be tuned by applying vertical pressure to push the graphene layers closer together and increase the interlayer coupling [203]. Consequently, the

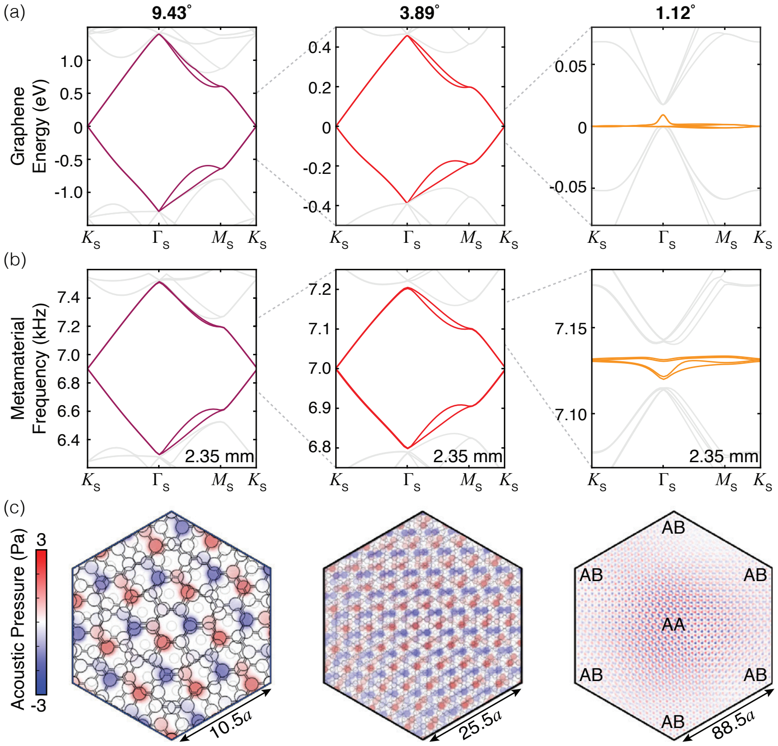

Figure 8.2: Trapping sound by twisting. (a) As the twist angle between two layers of graphene decreases, the Dirac bands are compressed around the Fermi level, eventually becoming completely flat at a magic angle of 1.12°, as shown in these electronic tight-binding calculations of unrelaxed twisted bilayer graphene. (b) The same trend occurs in our numerical simulations of a bilayer acoustic metamaterial, spawning acoustic flat bands at 1.12°. (c) For large angles, the calculated acoustic Dirac-like modes at the K_s point are itinerant and persist across the entire supercell. But at the magic angle, they become localized on the AA-stacked region in the center of the supercell.

Dirac bands begin to flatten at higher angles under pressure than at ambient conditions. However, a substantial vertical pressure of a few GPa is required to move the magic angle from 1.1° to 1.27°, corresponding to only a 20% increase in the interlayer coupling strength [202]. In our metamaterial, no such physical restrictions apply: the interlayer coupling can be tuned over two orders of magnitude simply by changing the thickness of the coupling membrane [5]. In practice, we anticipate an experimental setup that includes interchangeable polyethylene sheets of different thicknesses. To demonstrate this capability, we numerically reproduced the band flattening at a fixed angle of 2° simply by incrementally reducing the thickness of the interlayer membrane to 1.21 mm (Fig. 8.3).

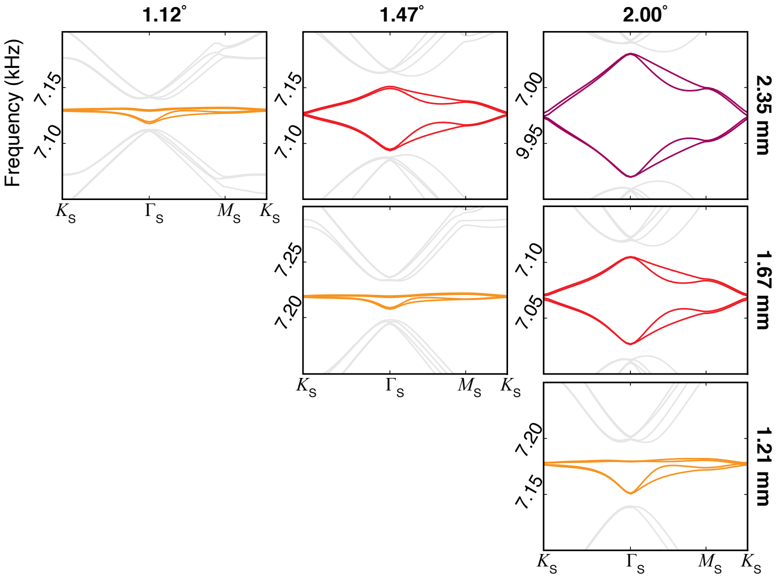

Figure 8.3: Interlayer coupling tunes the magic angle. Reducing the thickness of the polyethylene membrane enhances the coupling between layers of our simulated acoustic metamaterial. Consequently, an acoustic flat band (orange) can been formed either by decreasing the twist angle with a fixed membrane thickness (along rows), or by decreasing the thickness at fixed angle (columns). For example, to realize flat bands at 2°, we need to reduce the membrane thickness to 1.21 mm.

In other words, the flat band condition can be approached from two directions: either reduce the twist angle at fixed interlayer thickness, or reduce the thickness at fixed angle. For comparison, it is expected to require about 9 GPa of vertical pressure for twisted bilayer graphene to reach flat bands at 2° [203].

8.4 Exploring extreme coupling regimes

Our acoustic metamaterial provides a simple computational platform to explore twistronics in extreme coupling regimes, well beyond the experimental capability of its electronic counterpart. By further reducing the interlayer membrane thickness, we searched for flat bands at high commensurate angles of 3.89°, 5.09°, and 6.01°, equivalent to pressures of 45 GPa, 85 GPa, and 129 GPa that would need to be applied to the graphene system [203]. In each case, we discovered flat bands

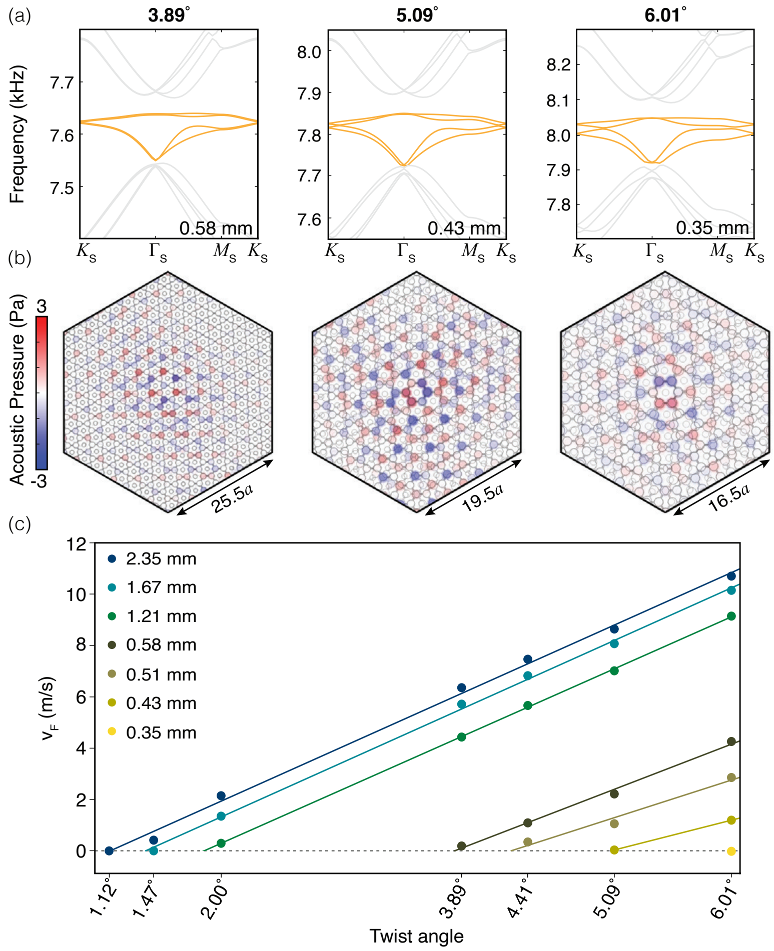

Figure 8.4: Reproducing flat bands at high magic angles. (a) By reducing the thickness of the interlayer membrane to 0.58 mm, 0.43 mm, and 0.35 mm, we computed flat bands at 3.89°, 5.09°, and 6.01° twist angles. (b) In each case, the simulated K_s-point eigenmodes appear predominantly around the AA-stacked region in the center of the supercell. As the supercell shrinks, these localized modes form a dense array, increasing the possibility of interactions with similar localized modes in neighboring supercells. (c) By correctly choosing the interlayer membrane's thickness, any angle can become a magic angle with a vanishing K_s-point velocity.

similar to those in twisted bilayer graphene (Fig. 8.4(a)). These flat bands all correspond to collective pressure modes that are localized on the AA-stacked central regions (Fig. 8.4(b)). But these localized modes are over five times closer to each other spatially at 6.01° than they are at 1.12°. Generally speaking, the modes interact more strongly as they become closer together, potentially allowing interactions to dominate over the reduced kinetic energy at a high magic angle. Consequently, a high-magic-angle metamaterial could be susceptible to non-linear effects if tuned correctly, akin to a phonon-phonon interaction. In principle, any twist angle can become a magic angle that hosts a dense array of such localized modes, by choosing the correct interlayer thickness (Fig. 8.4(c)).

Although we focused on recreating twisted bilayer graphene, our metamaterial can be easily extended to capture other vdW systems. For example, by breaking the sublattice symmetry in our unit cell, one can explore the localized modes shaped from twisted quadratic bands, imitating semiconductors like hexagonal boron nitride [229] or transition-metal dichalcogenides [230]. Our metamaterial platform could even mimic twistronic Hamiltonians that cannot yet be realized in condensed matter experiments, which are restricted to the primarily-hexagonal set of 2D materials available today. In principle, a twistronic heterostructure can be constructed from any lattice symmetry to spawn diverse flat bands with distinct topologies [231]. Acoustic metamaterials can smoothly deform between these twistronic phases, allowing their properties to be isolated, optimized, or combined. Further, our metamaterial design can independently control AA and AB coupling by appropriately texturing the interlayer membrane, which may unlock perfectly flat bands at the magic angle [206]. It can also implement tunable in-plane lattice relaxation, which modifies both the electronic [205, 232] and phononic [233, 234] bands in twisted bilayer graphene. Beyond two-layer systems, our design motivates a future experimental setup to explore the intricate moiré patterns created by multiple arbitrary twist angles. Such experimental acoustic devices may quickly surpass theoretical electronic calculations, which are made nearly impossible by the highly incommensurate geometry, even in the three-layer case [235]. Importantly, our design translates to the length scales and materials required for photonic [127] or surface-acoustic-wave [130] devices, which may provide a more-natural platform to fabricate the large arrays required to study complex multilayer structures.

The enormous phase space of twisted vdW heterostructures promises many new phenomena, but unearthing them is hindered by theoretical and experimental obstacles. Our twisted bilayer metamaterial translates the field of twistronics to acoustics, opening a different path to continue this search (see roadmap in supplement (available online at stacks.iop.org/2DM/8/031002/mmedia). By introducing a twist angle to vdW metamaterials, we discovered flat bands that *precisely* mimic the behavior of twisted bilayer graphene at 1.1° and that slow transmitted sound by a factor of 600 (20 times slower than a leisurely walk). The close agreement between our acoustic system and its electronic counterpart gives confidence that twisted acoustic metamaterials can be a valuable platform for more general quantum material design. For example, future 3D-printed acoustic metamaterials could simulate multilayer twistronic heterostructures containing several independent twist angles, a challenging regime for today's theoretical tools. Meanwhile, recent experiments have demonstrated control of surface acoustic waves in the quantum limit [128, 129], which could provide a new direction to incorporate phonon-phonon interactions into our acoustic system.

8.5 Methods

We simulate three-dimensional metamaterial models using the pressure acoustics, frequency domain interface within the acoustics module of COMSOL MULTIPHYSICS. A basic monolayer metamaterial consists of a honeycomb arrangement of air cavities, with radius of 3.5 mm and a separation of 10 mm, in a 1-mm-thick steel sheet. To form a bilayer metamaterial, two such steel sheets are separated and bounded by three identical polyethylene membranes, as shown in Fig. 8.1(a). The bounding and interlayer membranes all have identical, tunable thicknesses. Each model is cut to form a supercell at a commensurate twist angle, allowing three pairs of Floquet periodic boundary conditions on its six hexagonal sides. The top and bottom boundary sheets are impedance-matched to air on their outer faces. Our metamaterial contains three materials: steel plates (density 7070 kg/m^3 and speed of sound 5790 m/s), air cavities (1.2 kg/m^3, 343 m/s), and high-density polyethylene interlayer and outer boundary membranes (950 kg/m^3, 2460 m/s). The mesh conditions we use depend on the size of the unit cell. For the monolayer and untwisted bilayer metamaterials, as well as twisted bilayer metamaterials with twist angles above 3.89°, we use the physics-controlled “fine” mesh. For models with lower twist angles, we switch to a coarser user-defined mesh with the following parameters: minimum element size 0.09, maximum element size 1, maximum growth rate 1.45, curvature factor 0.5, and resolution 0.6. After constructing the appropriate metamaterial supercell, we create an eigenfrequency study using the following parametric sweep. For a hexagonal supercell with moiré length L, we simulate the $\mathbf{k}$-space sweep around the supercell Brillouin zone along the path $\Gamma_s \to K_s \to M_s \to \Gamma_s$ using the following equation:

$$\mathbf{k} = \frac{\pi}{3\sqrt{3}L} \begin{cases} \begin{pmatrix} 4a \\ 0 \end{pmatrix} & 0 < a < 1 \\ \begin{pmatrix} 6 - 2a \\ \sqrt{3}(2a - 1) \end{pmatrix} & 1 < a < 1.5 \\ \begin{pmatrix} 3 + 3\sqrt{3} - 2\sqrt{3}a \\ 3 + \sqrt{3} - 2a \end{pmatrix} & 1.5 < a < \dfrac{3 + \sqrt{3}}{2}, \end{cases}$$

where a is an arbitrary sweep parameter. To speed up computation, we typically calculate only the ten eigenfrequencies closest to the Dirac frequency.

The electronic band structures of TBG displayed in Fig. 8.2(a) were generated using a tight-binding model based on density functional theory (DFT) results for bilayer graphene [236]. For the selected angles, we use a twisted commensurate supercell alongside the DFT-derived couplings to populate an electronic k-dependent Hamiltonian, which we then diagonalize. Although atomic relaxations are known to modify the magic angle and the low-energy band gaps between the flat bands and nearby bands in quantum materials [227], we do not attempt to incorporate analogous relaxations in our metamaterial.

References

[1] H. Pirie, Y. Liu, A. Soumyanarayanan, P. Chen, Y. He, M. M. Yee, P. F. S. Rosa, J. D. Thompson, D.-J. Kim, Z. Fisk, X. Wang, J. Paglione, D. K. Morr, M. H. Hamidian, and J. E. Hoffman, "Imaging emergent heavy Dirac fermions of a topological Kondo insulator," Nature Physics **16**, 52–56 (2020).

[2] C. E. Matt, H. Pirie, A. Soumyanarayanan, Y. He, M. M. Yee, P. Chen, Y. Liu, D. T. Larson, W. S. Paz, J. J. Palacios, M. H. Hamidian, and J. E. Hoffman, "Consistency between ARPES and STM measurements on SmB_6," Phys. Rev. B **101**, 085142 (2020).

[3] H. Pirie, E. Mascot, C. E. Matt, Y. Liu, P. Chen, M. H. Hamidian, S. Saha, X. Wang, J. Paglione, G. Luke, C. Hirjibehedin, J. C. S. Davis, D. K. Morr, and J. E. Hoffman, "Visualizing the charge puddles around Kondo holes" (in preparation).

[4] H. Pirie, S. Sadhuka, J. Wang, R. Andrei, and J. E. Hoffman, "Topological phononic logic," Phys. Rev. Lett. **128**, 015501 (2022).

[5] W. Dorrell, H. Pirie, S. M. Gardezi, N. C. Drucker, and J. E. Hoffman, "van der waals metamaterials," Phys. Rev. B **101**, 121103 (2020).

[6] S. M. Gardezi, H. Pirie, S. Carr, W. Dorrell, and J. E. Hoffman, "Simulating twistronics in acoustic metamaterials," 2D Materials **8**, 031002 (2021).

[7] J.-F. Ge, Z.-L. Liu, C. Liu, C.-L. Gao, D. Qian, Q.-K. Xue, Y. Liu, and J.-F. Jia, "Superconductivity above 100 K in single-layer FeSe films on doped $SrTiO_3$," Nature Materials **14**, 285–289 (2015).

[8] D. Huang and J. E. Hoffman, "Monolayer FeSe on $SrTiO_3$," Annual Review of Condensed Matter Physics **8**, 311–336 (2017).

[9] A. Kitaev, "Fault-tolerant quantum computation by anyons," Annals of Physics **303**, 2–30 (2003).

[10] A. Fornieri, A. M. Whiticar, F. Setiawan, E. Portolés, A. C. C. Drachmann, A. Keselman, S. Gronin, C. Thomas, T. Wang, R. Kallaher, G. C. Gardner, E. Berg, M. J. Manfra,

A. Stern, C. M. Marcus, and F. Nichele, "Evidence of topological superconductivity in planar Josephson junctions," Nature **569**, 89–92 (2019).

[11] H. Ren, F. Pientka, S. Hart, A. T. Pierce, M. Kosowsky, L. Lunczer, R. Schlereth, B. Scharf, E. M. Hankiewicz, L. W. Molenkamp, B. I. Halperin, and A. Yacoby, "Topological superconductivity in a phase-controlled Josephson junction," Nature **569**, 93–98 (2019).

[12] F. Arute, K. Arya, R. Babbush, D. Bacon, J. C. Bardin, R. Barends, R. Biswas, S. Boixo, F. G. S. L. Brandao, D. A. Buell, B. Burkett, Y. Chen, Z. Chen, B. Chiaro, R. Collins, W. Courtney, A. Dunsworth, E. Farhi, B. Foxen, A. Fowler, C. Gidney, M. Giustina, R. Graff, K. Guerin, S. Habegger, M. P. Harrigan, M. J. Hartmann, A. Ho, M. Hoffmann, T. Huang, T. S. Humble, S. V. Isakov, E. Jeffrey, Z. Jiang, D. Kafri, K. Kechedzhi, J. Kelly, P. V. Klimov, S. Knysh, A. Korotkov, F. Kostritsa, D. Landhuis, M. Lindmark, E. Lucero, D. Lyakh, S. Mandrà, J. R. McClean, M. McEwen, A. Megrant, X. Mi, K. Michielsen, M. Mohseni, J. Mutus, O. Naaman, M. Neeley, C. Neill, M. Y. Niu, E. Ostby, A. Petukhov, J. C. Platt, C. Quintana, E. G. Rieffel, P. Roushan, N. C. Rubin, D. Sank, K. J. Satzinger, V. Smelyanskiy, K. J. Sung, M. D. Trevithick, A. Vainsencher, B. Villalonga, T. White, Z. J. Yao, P. Yeh, A. Zalcman, H. Neven, and J. M. Martinis, "Quantum supremacy using a programmable superconducting processor," Nature **574**, 505–510 (2019).

[13] S. Doniach, "The Kondo lattice and weak antiferromagnetism," Physica B **91**, 231–234 (1977).

[14] F. Steglich, J. Aarts, C. D. Bredl, W. Lieke, D. Meschede, W. Franz, and H. Schäfer, "Superconductivity in the Presence of Strong Pauli Paramagnetism: $CeCu_2Si_2$," Physical Review Letters **43**, 1892–1896 (1979).

[15] K. Andres, J. E. Graebner, and H. R. Ott, "4*f*-Virtual-Bound-State Formation in $CeAl_3$ at Low Temperatures," Physical Review Letters **35**, 1779–1782 (1975).

[16] Z. Fisk, H. R. Ott, T. M. Rice, and J. L. Smith, "Heavy-electron metals," Nature **320**, 124–129 (1986).

[17] K. Flachbart, S. Gabáni, K. Neumaier, Y. Paderno, V. Pavlík, E. Schuberth, and N. Shitsevalova, "Specific heat of SmB_6 at very low temperatures," Physica B: Condensed Matter **378–380**, 610–611 (2006).

[18] N. J. Laurita, C. M. Morris, S. M. Koohpayeh, P. F. S. Rosa, W. A. Phelan, Z. Fisk, T. M. McQueen, and N. P. Armitage, "Anomalous three-dimensional bulk ac conduction within the Kondo gap of SmB_6 single crystals," Physical Review B **94**, 165154 (2016).

[19] B. S. Tan, Y.-T. Hsu, B. Zeng, M. C. Hatnean, N. Harrison, Z. Zhu, M. Hartstein, M. Kiourlappou, A. Srivastava, M. D. Johannes, T. P. Murphy, J.-H. Park, L. Balicas, G. G.

Lonzarich, G. Balakrishnan, and S. E. Sebastian, "Unconventional Fermi surface in an insulating state," Science **349**, 287–290 (2015).

[20] Z. Xiang, Y. Kasahara, T. Asaba, B. Lawson, C. Tinsman, L. Chen, K. Sugimoto, S. Kawaguchi, Y. Sato, G. Li, S. Yao, Y. L. Chen, F. Iga, J. Singleton, Y. Matsuda, and L. Li, "Quantum oscillations of electrical resistivity in an insulator," Science **362**, 65–69 (2018).

[21] T. E. Millichamp, D. Billington, H. C. Robarts, J. Laverock, D. ONeill, M. C. Hatnean, G. Balakrishnan, J. A. Duffy, J. W. Taylor, S. R. Giblin, and S. B. Dugdale, "Direct measurement of a remnant Fermi surface in SmB_6," arXiv:2111.07727 [cond-mat] (2021), arXiv:2111.07727 [cond-mat] .

[22] Y. S. Eo, A. Rakoski, J. Lucien, D. Mihaliov, Ç. Kurdak, P. F. S. Rosa, and Z. Fisk, "Transport gap in SmB_6 protected against disorder," Proceedings of the National Academy of Sciences **116**, 12638–12641 (2019).

[23] G. Baskaran, "Majorana Fermi Sea in Insulating SmB_6: A proposal and a Theory of Quantum Oscillations in Kondo Insulators," arXiv:1507.03477 [cond-mat] (2015), arXiv:1507.03477 [cond-mat] .

[24] J. Knolle and N. R. Cooper, "Quantum Oscillations without a Fermi Surface and the Anomalous de Haas–van Alphen Effect," Physical Review Letters **115**, 146401 (2015).

[25] O. Erten, P.-Y. Chang, P. Coleman, and A. M. Tsvelik, "Skyrme Insulators: Insulators at the Brink of Superconductivity," Physical Review Letters **119**, 057603 (2017).

[26] D. Chowdhury, I. Sodemann, and T. Senthil, "Mixed-valence insulators with neutral Fermi surfaces," Nature Communications **9**, 1766 (2018).

[27] H. Shen and L. Fu, "Quantum Oscillation from In-Gap States and a Non-Hermitian Landau Level Problem," Physical Review Letters **121**, 026403 (2018).

[28] B. Skinner, "Properties of the donor impurity band in mixed valence insulators," Physical Review Materials **3**, 104601 (2019).

[29] W. T. Fuhrman and P. Nikolić, "Magnetic impurities in Kondo insulators: An application to samarium hexaboride," Physical Review B **101**, 245118 (2020).

[30] M. Abele, X. Yuan, and P. S. Riseborough, "Topological nonmagnetic impurity states in topological Kondo insulators," Physical Review B **101**, 094101 (2020).

[31] M. Z. Hasan and C. L. Kane, "*Colloquium* : Topological insulators," Reviews of Modern Physics **82**, 3045–3067 (2010).

[32] M. Dzero, K. Sun, V. Galitski, and P. Coleman, "Topological Kondo insulators," Physical Review Letters **104**, 106408 (2010).

[33] V. Alexandrov, P. Coleman, and O. Erten, "Kondo breakdown in topological Kondo insulators," Physical Review Letters **114**, 177202 (2015).

[34] M. Dzero, J. Xia, V. Galitski, and P. Coleman, "Topological Kondo Insulators," Annual Review of Condensed Matter Physics **7**, 249–280 (2016).

[35] A. Thomson and S. Sachdev, "Fractionalized Fermi liquid on the surface of a topological Kondo insulator," Physical Review B **93**, 125103 (2016).

[36] C. Wang, A. C. Potter, and T. Senthil, "Gapped symmetry preserving surface state for the electron topological insulator," Physical Review B **88**, 115137 (2013).

[37] X. Chen, L. Fidkowski, and A. Vishwanath, "Symmetry enforced non-Abelian topological order at the surface of a topological insulator," Physical Review B **89**, 165132 (2014).

[38] T. Takimoto, "SmB_6 : A Promising Candidate for a Topological Insulator," Journal of the Physical Society of Japan **80**, 123710 (2011).

[39] F. Lu, J. Zhao, H. Weng, Z. Fang, and X. Dai, "Correlated Topological Insulators with Mixed Valence," Physical Review Letters **110**, 096401 (2013).

[40] D. K. Efimkin and V. Galitski, "Strongly interacting Dirac liquid on the surface of a topological Kondo insulator," Physical Review B **90**, 081113 (2014).

[41] S. Wolgast, Ç. Kurdak, K. Sun, J. W. Allen, D.-J. Kim, and Z. Fisk, "Low-temperature surface conduction in the Kondo insulator SmB_6," Physical Review B **88**, 180405 (2013).

[42] X. Zhang, N. P. Butch, P. Syers, S. Ziemak, R. L. Greene, and J. Paglione, "Hybridization, inter-ion correlation, and surface states in the Kondo insulator SmB_6," Physical Review X **3**, 011011 (2013).

[43] D. J. Kim, S. Thomas, T. Grant, J. Botimer, Z. Fisk, and J. Xia, "Surface Hall effect and nonlocal transport in SmB_6: Evidence for surface conduction," Scientific Reports **3**, 3150 (2013).

[44] P. Syers, D. Kim, M. S. Fuhrer, and J. Paglione, "Tuning Bulk and Surface Conduction in the Proposed Topological Kondo Insulator SmB_6," Physical Review Letters **114**, 096601 (2015).

[45] J. D. Denlinger, J. W. Allen, J.-S. Kang, K. Sun, B.-I. Min, D.-J. Kim, and Z. Fisk, "SmB_6 photoemission: Past and present," in *Proceedings of the International Conference on Strongly Correlated Electron Systems (SCES2013)* (JPS Conf. Proc. 3, 017038, 2014).

[46] N. Xu, X. Shi, P. K. Biswas, C. E. Matt, R. S. Dhaka, Y. Huang, N. C. Plumb, M. Radović, J. H. Dil, E. Pomjakushina, K. Conder, A. Amato, Z. Salman, D. M. Paul, J. Mesot, H. Ding, and M. Shi, "Surface and bulk electronic structure of the strongly correlated system SmB_6 and implications for a topological Kondo insulator," Physical Review B **88**, 121102(R) (2013).

[47] N. Xu, C. E. Matt, E. Pomjakushina, X. Shi, R. S. Dhaka, N. C. Plumb, M. Radović, P. K. Biswas, D. Evtushinsky, V. Zabolotnyy, J. H. Dil, K. Conder, J. Mesot, H. Ding, and M. Shi, "Exotic Kondo crossover in a wide temperature region in the topological Kondo insulator SmB_6 revealed by high-resolution ARPES," Physical Review B **90**, 085148 (2014).

[48] M. Neupane, N. Alidoust, S.-Y. Xu, T. Kondo, Y. Ishida, D. J. Kim, C. Liu, I. Belopolski, Y. J. Jo, T.-R. Chang, H.-T. Jeng, T. Durakiewicz, L. Balicas, H. Lin, A. Bansil, S. Shin, Z. Fisk, and M. Z. Hasan, "Surface electronic structure of the topological Kondo-insulator candidate correlated electron system SmB_6," Nature Communications **4**, 2991 (2013).

[49] J. Jiang, S. Li, T. Zhang, Z. Sun, F. Chen, Z. R. Ye, M. Xu, Q. Q. Ge, S. Y. Tan, X. H. Niu, M. Xia, B. P. Xie, Y. F. Li, X. H. Chen, H. H. Wen, and D. L. Feng, "Observation of possible topological in-gap surface states in the Kondo insulator SmB_6 by photoemission." Nature communications **4**, 3010 (2013).

[50] E. Frantzeskakis, N. de Jong, B. Zwartsenberg, Y. K. Huang, Y. Pan, X. Zhang, J. X. Zhang, F. X. Zhang, L. H. Bao, O. Tegus, A. Varykhalov, A. de Visser, and M. S. Golden, "Kondo Hybridization and the Origin of Metallic States at the (001) Surface of SmB_6," Physical Review X **3**, 041024 (2013).

[51] Z.-H. Zhu, A. Nicolaou, G. Levy, N. P. Butch, P. Syers, X. F. Wang, J. Paglione, G. A. Sawatzky, I. S. Elfimov, and A. Damascelli, "Polarity-Driven Surface Metallicity in SmB_6," Physical Review Letters **111**, 216402 (2013).

[52] P. Hlawenka, K. Siemensmeyer, E. Weschke, A. Varykhalov, J. Sánchez-Barriga, N. Y. Shitsevalova, A. V. Dukhnenko, V. B. Filipov, S. Gabáni, K. Flachbart, O. Rader, and E. D. L. Rienks, "Samarium hexaboride is a trivial surface conductor," Nature Communications **9**, 517 (2018).

[53] G. Li, Z. Xiang, F. Yu, T. Asaba, B. Lawson, P. Cai, C. Tinsman, A. Berkley, S. Wolgast, Y. S. Eo, D.-J. Kim, C. Kurdak, J. W. Allen, K. Sun, X. H. Chen, Y. Y. Wang, Z. Fisk, and L. Li, "Two-dimensional Fermi surfaces in Kondo insulator SmB_6," Science **346**, 1208–1212 (2014).

[54] S. M. Thomas, X. Ding, F. Ronning, V. Zapf, J. D. Thompson, Z. Fisk, J. Xia, and P. F. S. Rosa, "Quantum Oscillations in Flux-Grown SmB 6 with Embedded Aluminum," Physical Review Letters **122**, 166401 (2019).

[55] S. Wirth and P. Schlottmann, "An STM Perspective on Hexaborides: Surface States of the Kondo Insulator SmB $_6$," Advanced Quantum Technologies , 2100102 (2021).

[56] V. Alexandrov, M. Dzero, and P. Coleman, "Cubic topological Kondo insulators," Physical Review Letters **111**, 226403 (2013).

[57] J. W. Allen, B. Batlogg, and P. Wachter, "Large low-temperature Hall effect and resistivity in mixed-valent SmB_6," Physical Review B **20**, 4807–4813 (1979).

[58] D. J. Kim, J. Xia, and Z. Fisk, "Topological surface state in the Kondo insulator samarium hexaboride," Nature Materials **13**, 466–470 (2014).

[59] Y. Luo, H. Chen, J. Dai, Z.-A. Xu, and J. D. Thompson, "Heavy surface state in a possible topological Kondo insulator: Magnetothermoelectric transport on the (011) plane of SmB_6," Physical Review B **91**, 075130 (2015).

[60] See Supplemental Materials at https://doi.org/10.1038/s41567-019-0700-8 for additional details on sample characterization, identifying the scattering process, the origin of backscattering, QPI on different samples, the impact of defects, the lack of a mass gap, the lack of band bending, modelling the spectral function, co-tunneling in Kondo lattices, identifying the Dirac point, and comparing different experimental results.

[61] B. Gorshunov, N. Sluchanko, A. Volkov, M. Dressel, G. Knebel, A. Loidl, and S. Kunii, "Low-energy electrodynamics of SmB_6," Physical Review B **59**, 1808–1814 (1999).

[62] W. Ruan, C. Ye, M. Guo, F. Chen, X. Chen, G.-M. Zhang, and Y. Wang, "Emergence of a Coherent In-Gap State in the SmB_6 Kondo Insulator Revealed by Scanning Tunneling Spectroscopy," Physical Review Letters **112**, 136401 (2014).

[63] S. Rößler, T.-H. Jang, D.-J. Kim, L. H. Tjeng, Z. Fisk, F. Steglich, and S. Wirth, "Hybridization gap and Fano resonance in SmB_6," Proceedings of the National Academy of Sciences **111**, 4798–4802 (2014).

[64] J. A. Stroscio, R. M. Feenstra, and A. P. Fein, "Electronic structure of the Si(111)2×1 surface by scanning-tunneling microscopy," Physical Review Letters **57**, 2579–2582 (1986).

[65] A. R. Schmidt, M. H. Hamidian, P. Wahl, F. Meier, A. V. Balatsky, J. D. Garrett, T. J. Williams, G. M. Luke, and J. C. Davis, "Imaging the Fano lattice to 'hidden order' transition in $\mathrm{URu}_2\mathrm{Si}_2$," Nature **465**, 570–576 (2010).

[66] P. Aynajian, E. H. da Silva Neto, A. Gyenis, R. E. Baumbach, J. D. Thompson, Z. Fisk, E. D. Bauer, and A. Yazdani, "Visualizing heavy fermions emerging in a quantum critical Kondo lattice." Nature **486**, 201–206 (2012).

[67] M. P. Allan, F. Massee, D. K. Morr, J. Van Dyke, A. W. Rost, A. P. Mackenzie, C. Petrovic, and J. C. Davis, "Imaging Cooper pairing of heavy fermions in $CeCoIn_5$," Nature Physics **9**, 468–473 (2013).

[68] L. Jiao, S. Rößler, D. J. Kim, L. H. Tjeng, Z. Fisk, F. Steglich, and S. Wirth, "Additional energy scale in SmB_6 at low-temperature," Nature Communications **7**, 13762 (2016).

[69] H.-M. Guo and M. Franz, "Theory of quasiparticle interference on the surface of a strong topological insulator," Physical Review B **81**, 041102 (2010).

[70] R. H. Nyberg, E. Rossi, and D. K. Morr, "Identifying collective modes through impurity pinning in cuprate superconductors," Phys. Rev. B **78**, 054504 (2008).

[71] Y. Baum and A. Stern, "Magnetic instability on the surface of topological insulators," Physical Review B **85**, 121105 (2012).

[72] Y. Nakajima, P. Syers, X. Wang, R. Wang, and J. Paglione, "One-dimensional edge state transport in a topological Kondo insulator," Nature Physics **12**, 213–217 (2015).

[73] J. Figgins and D. K. Morr, "Defects in Heavy-Fermion Materials: Unveiling Strong Correlations in Real Space," Physical Review Letters **107**, 066401 (2011).

[74] Y. Okada, C. Dhital, W. Zhou, E. D. Huemiller, H. Lin, S. Basak, A. Bansil, Y.-B. Huang, H. Ding, Z. Wang, S. D. Wilson, and V. Madhavan, "Direct observation of broken time-reversal symmetry on the surface of a magnetically doped topological insulator," Physical Review Letters **106**, 206805 (2011).

[75] M. Maltseva, M. Dzero, and P. Coleman, "Electron Cotunneling into a Kondo Lattice," Physical Review Letters **103**, 206402 (2009).

[76] J. Figgins and D. K. Morr, "Differential Conductance and Quantum Interference in Kondo Systems," Physical Review Letters **104**, 187202 (2010).

[77] K. Akintola, A. Pal, M. Potma, S. R. Saha, X. F. Wang, J. Paglione, and J. E. Sonier, "Quantum spin fluctuations in the bulk insulating state of pure and Fe-doped SmB_6," Physical Review B **95**, 245107 (2017).

[78] P. Misra, in *Handbook of Metal Physics*, Heavy-Fermion Systems, Chapter 11 Kondo Insulators, Vol. 2, edited by P. Misra (Elsevier, 2008) pp. 291–333.

[79] J. C. Cooley, M. C. Aronson, Z. Fisk, and P. C. Canfield, "SmB_6: Kondo insulator or exotic metal?" Phys. Rev. Lett. **74**, 1629–1632 (1995).

[80] N. Xu, P. K. Biswas, J. H. Dil, R. S. Dhaka, G. Landolt, S. Muff, C. E. Matt, X. Shi, N. C. Plumb, M. Radović, E. Pomjakushina, K. Conder, A. Amato, S. V. Borisenko, R. Yu, H.-M. Weng, Z. Fang, X. Dai, J. Mesot, H. Ding, and M. Shi, "Direct observation of the spin texture in SmB_6 as evidence of the topological Kondo insulator," Nature Communications **5**, 4566 (2014).

[81] S. Suga, K. Sakamoto, T. Okuda, K. Miyamoto, K. Kuroda, A. Sekiyama, J. Yamaguchi, H. Fujiwara, A. Irizawa, T. Ito, S. Kimura, T. Balashov, W. Wulfhekel, S. Yeo, F. Iga, and S. Imada, "Spin-polarized angle-resolved photoelectron spectroscopy of the so-predicted Kondo topological insulator SmB_6," Journal of the Physical Society of Japan **83**, 014705 (2013).

[82] B. Roy, J. D. Sau, M. Dzero, and V. Galitski, "Surface theory of a family of topological Kondo insulators," Physical Review B **90**, 155314 (2014).

[83] Z. Sun, A. Maldonado, W. S. Paz, D. S. Inosov, A. P. Schnyder, J. J. Palacios, N. Y. Shitsevalova, V. B. Filipov, and P. Wahl, "Observation of a well-defined hybridization gap and in-gap states on the SmB_6(001) surface," Physical Review B **97**, 235107 (2018).

[84] M. M. Yee, Y. He, A. Soumyanarayanan, D.-J. Kim, Z. Fisk, and J. E. Hoffman, "Imaging the Kondo insulating gap on SmB_6," (2013), arXiv:1308.1085 .

[85] N. Xu, H. Ding, and M. Shi, "Spin- and angle-resolved photoemission on the topological Kondo insulator candidate: SmB_6," Journal of Physics: Condensed Matter **28**, 363001 (2016).

[86] P. Giannozzi, S. Baroni, N. Bonini, M. Calandra, R. Car, C. Cavazzoni, D. Ceresoli, G. L. Chiarotti, M. Cococcioni, I. Dabo, A. Dal Corso, S. de Gironcoli, S. Fabris, G. Fratesi, R. Gebauer, U. Gerstmann, C. Gougoussis, A. Kokalj, M. Lazzeri, L. Martin-Samos, N. Marzari, F. Mauri, R. Mazzarello, S. Paolini, A. Pasquarello, L. Paulatto, C. Sbraccia, S. Scandolo, G. Sclauzero, A. P. Seitsonen, A. Smogunov, P. Umari, and R. M. Wentzcovitch, "QUANTUM ESPRESSO: a modular and open-source software project for quantum simulations of materials," Journal of Physics: Condensed Matter **21**, 395502 (2009).

[87] J. P. Perdew, K. Burke, and M. Ernzerhof, "Generalized gradient approximation made simple," Physical Review Letters **77**, 3865–3868 (1996).

[88] H. J. Monkhorst and J. D. Pack, "Special points for Brillouin-zone integrations," Physical Review B **13**, 5188 (1976).

[89] S. Rößler, L. Jiao, D. J. Kim, S. Seiro, K. Rasim, F. Steglich, L. H. Tjeng, Z. Fisk, and S. Wirth, "Surface and electronic structure of SmB_6 through scanning tunneling microscopy," Philosophical Magazine **96**, 3262–3273 (2016).

[90] L. Jiao, S. Rößler, D. Kasinathan, P. F. S. Rosa, C. Guo, H. Yuan, C.-X. Liu, Z. Fisk, F. Steglich, and S. Wirth, "Magnetic and Defect Probes of the SmB_6 Surface State," Science Advances **4**, eaau4886 (2018).

[91] H. Herrmann, P. Hlawenka, K. Siemensmeyer, E. Weschke, J. Sánchez-Barriga, A. Varykhalov, N. Y. Shitsevalova, A. V. Dukhnenko, V. B. Filipov, S. Gabáni, K. Flachbart, O. Rader, M. Sterrer, and E. D. L. Rienks, "Contrast Reversal in Scanning Tunneling Microscopy and Its Implications for the Topological Classification of SmB $_6$," Advanced Materials **32**, 1906725 (2020).

[92] Data can be accessed at the repository: https://doi.org/10.18126/cjyc-7ugb.

[93] S. V. Ramankutty, N. de Jong, Y. K. Huang, B. Zwartsenberg, F. Massee, T. V. Bay, M. S. Golden, and E. Frantzeskakis, "Comparative study of rare earth hexaborides using high resolution angle-resolved photoemission," Journal of Electron Spectroscopy and Related Phenomena **208**, 43–50 (2016).

[94] Z. Zhang and J. T. Yates, "Band bending in semiconductors: Chemical and physical consequences at surfaces and interfaces," Chemical Reviews **112**, 5520–5551 (2012).

[95] J. M. Tarascon, Y. Isikawa, B. Chevalier, J. Etourneau, P. Hagenmuller, and M. Kasaya, "Temperature dependence of the samarium oxidation state in SmB_6 and $Sm_{1-x}La_xB_6$," Journal de Physique **41**, 1141–1145 (1980).

[96] J. D. Denlinger, J. W. Allen, J.-S. Kang, K. Sun, J.-W. Kim, J. H. Shim, B. I. Min, D.-J. Kim, and Z. Fisk, "Temperature dependence of linked gap and surface state evolution in the mixed valent topological insulator SmB_6," (2013), arXiv:1312.6637 .

[97] C. M. Varma, Z. Nussinov, and W. van Saarloos, "Singular or non-Fermi liquids," Physics Reports **361**, 267–417 (2002).

[98] Y. Ohtsubo, Y. Yamashita, K. Hagiwara, S.-i. Ideta, K. Tanaka, R. Yukawa, K. Horiba, H. Kumigashira, K. Miyamoto, T. Okuda, W. Hirano, F. Iga, and S.-i. Kimura, "Non-trivial surface states of samarium hexaboride at the (111) surface," Nature Communications **10**, 1–7 (2019).

[99] J. D. Denlinger, S. Jang, G. Li, L. Chen, B. J. Lawson, T. Asaba, C. Tinsman, F. Yu, K. Sun, J. W. Allen, C. Kurdak, D.-J. Kim, Z. Fisk, and L. Li, "Consistency of photoemission and quantum oscillations for surface states of SmB_6," (2016), arXiv:1601.07408 .

[100] J. Yong, Y. Jiang, D. Usanmaz, S. Curtarolo, X. Zhang, L. Li, X. Pan, J. Shin, I. Takeuchi, and R. L. Greene, "Robust topological surface state in Kondo insulator SmB_6 thin films," Applied Physics Letters **105**, 222403 (2014).

[101] E. Dagotto, "Complexity in Strongly Correlated Electronic Systems," Science **309**, 257–262 (2005).

[102] R. Sollie and P. Schlottmann, "Local density of states in the vicinity of a Kondo hole," Journal of Applied Physics **70**, 5803–5805 (1991).

[103] A. de la Torre, P. Visani, Y. Dalichaouch, B. Lee, and M. Maple, "Th-doped URu_2Si_2: Influence of "Kondo holes" on coexisting superconductivity and magnetism," Physica B: Condensed Matter **179**, 208–214 (1992).

[104] R. R. Urbano, B.-L. Young, N. J. Curro, J. D. Thompson, L. D. Pham, and Z. Fisk, "Interacting Antiferromagnetic Droplets in Quantum Critical $CeCoIn_5$," Physical Review Letters **99**, 146402 (2007).

[105] J. M. Lawrence, J. D. Thompson, and Y. Y. Chen, "Two Energy Scales in $CePd_3$," Physical Review Letters **54**, 2537–2540 (1985).

[106] M. H. Hamidian, A. R. Schmidt, I. A. Firmo, M. P. Allan, P. Bradley, J. D. Garrett, T. J. Williams, G. M. Luke, Y. Dubi, A. V. Balatsky, and J. C. Davis, "How Kondo-holes create intense nanoscale heavy-fermion hybridization disorder," Proceedings of the National Academy of Sciences **108**, 18233–18237 (2011).

[107] B. Koslowski and C. Baur, "New potentiometry method in scanning tunneling microscopy: Exploiting the correlation of fluctuations," Journal of Applied Physics **77**, 28–33 (1995).

[108] C. Wagner, M. F. B. Green, P. Leinen, T. Deilmann, P. Krüger, M. Rohlfing, R. Temirov, and F. S. Tautz, "Scanning Quantum Dot Microscopy," Physical Review Letters **115**, 026101 (2015).

[109] P. Hapala, M. Švec, O. Stetsovych, N. J. van der Heijden, M. Ondráček, J. van der Lit, P. Mutombo, I. Swart, and P. Jelínek, "Mapping the electrostatic force field of single molecules from high-resolution scanning probe images," Nature Communications **7**, 11560 (2016).

[110] M. Nonnenmacher, M. P. O'Boyle, and H. K. Wickramasinghe, "Kelvin probe force microscopy," Applied Physics Letters **58**, 2921–2923 (1991).

[111] L. Gross, F. Mohn, N. Moll, P. Liljeroth, and G. Meyer, "The Chemical Structure of a Molecule Resolved by Atomic Force Microscopy," Science **325**, 1110–1114 (2009).

[112] F. Mohn, L. Gross, N. Moll, and G. Meyer, "Imaging the charge distribution within a single molecule," Nature Nanotechnology **7**, 227–231 (2012).

[113] U. Zerweck, C. Loppacher, T. Otto, S. Grafström, and L. M. Eng, "Accuracy and resolution limits of Kelvin probe force microscopy," Physical Review B **71**, 125424 (2005).

[114] S. Sadewasser, P. Jelinek, C.-K. Fang, O. Custance, Y. Yamada, Y. Sugimoto, M. Abe, and S. Morita, "New Insights on Atomic-Resolution Frequency-Modulation Kelvin-Probe Force-Microscopy Imaging of Semiconductors," Physical Review Letters **103**, 266103 (2009).

[115] F. Albrecht, J. Repp, M. Fleischmann, M. Scheer, M. Ondráček, and P. Jelínek, "Probing Charges on the Atomic Scale by Means of Atomic Force Microscopy," Physical Review Letters **115**, 076101 (2015).

[116] F. Albrecht, M. Fleischmann, M. Scheer, L. Gross, and J. Repp, "Local tunneling decay length and Kelvin probe force spectroscopy," Physical Review B **92**, 235443 (2015).

[117] Y. Kohsaka, C. Taylor, K. Fujita, A. Schmidt, C. Lupien, T. Hanaguri, M. Azuma, M. Takano, H. Eisaki, H. Takagi, S. Uchida, and J. C. Davis, "An Intrinsic Bond-Centered Electronic Glass with Unidirectional Domains in Underdoped Cuprates," Science **315**, 1380–1385 (2007).

[118] M. Hartstein, W. H. Toews, Y.-T. Hsu, B. Zeng, X. Chen, M. C. Hatnean, Q. R. Zhang, S. Nakamura, A. S. Padgett, G. Rodway-Gant, J. Berk, M. K. Kingston, G. H. Zhang, M. K. Chan, S. Yamashita, T. Sakakibara, Y. Takano, J.-H. Park, L. Balicas, N. Harrison, N. Shitsevalova, G. Balakrishnan, G. G. Lonzarich, R. W. Hill, M. Sutherland, and S. E. Sebastian, "Fermi surface in the absence of a Fermi liquid in the Kondo insulator SmB_6," Nature Physics **14**, 166–172 (2018).

[119] V. Madhavan, W. Chen, T. Jamneala, M. F. Crommie, and N. S. Wingreen, "Tunneling into a Single Magnetic Atom: Spectroscopic Evidence of the Kondo Resonance," Science **280**, 567–569 (1998).

[120] I. Giannakis, J. Leshen, M. Kavai, S. Ran, C.-J. Kang, S. R. Saha, Y. Zhao, Z. Xu, J. W. Lynn, L. Miao, L. A. Wray, G. Kotliar, N. P. Butch, and P. Aynajian, "Orbital-selective Kondo lattice and enigmatic *f* electrons emerging from inside the antiferromagnetic phase of a heavy fermion," Science Advances **5**, eaaw9061 (2019).

[121] M. B. Maple, J. W. Chen, Y. Dalichaouch, T. Kohara, C. Rossel, M. S. Torikachvili, M. W. McElfresh, and J. D. Thompson, "Partially gapped Fermi surface in the heavy-electron superconductor URu_2Si_2," Physical Review Letters **56**, 185–188 (1986).

[122] P. Aynajian, E. H. da Silva Neto, C. V. Parker, Y. Huang, A. Pasupathy, J. Mydosh, and A. Yazdani, "Visualizing the formation of the Kondo lattice and the hidden order in URu_2Si_2," Proceedings of the National Academy of Sciences **107**, 10383–10388 (2010).

[123] A. F. Santander-Syro, M. Klein, F. L. Boariu, A. Nuber, P. Lejay, and F. Reinert, "Fermi-surface instability at the 'hidden-order' transition of URu_2Si_2," Nature Physics **5**, 637–641 (2009).

[124] M. E. Valentine, S. Koohpayeh, W. A. Phelan, T. M. McQueen, P. F. S. Rosa, Z. Fisk, and N. Drichko, "Breakdown of the Kondo insulating state in SmB_6 by introducing Sm vacancies," Physical Review B **94**, 075102 (2016).

[125] W. T. Fuhrman, J. R. Chamorro, P. A. Alekseev, J.-M. Mignot, T. Keller, J. A. Rodriguez-Rivera, Y. Qiu, P. Nikolić, T. M. McQueen, and C. L. Broholm, "Screened moments and extrinsic in-gap states in samarium hexaboride," Nature Communications **9**, 1539 (2018).

[126] J. C. Souza, P. F. S. Rosa, J. Sichelschmidt, M. Carlone, P. A. Venegas, M. O. Malcolms, P. M. Menegasso, R. R. Urbano, Z. Fisk, and P. G. Pagliuso, "Metallic islands in the Kondo insulator SmB_6," Physical Review Research **2**, 043181 (2020).

[127] J. Mei, Y. Wu, C. T. Chan, and Z.-Q. Zhang, "First-principles study of Dirac and Dirac-like cones in phononic and photonic crystals," Physical Review B **86**, 035141 (2012).

[128] K. J. Satzinger, Y. P. Zhong, H.-S. Chang, G. A. Peairs, A. Bienfait, M.-H. Chou, A. Y. Cleland, C. R. Conner, É. Dumur, J. Grebel, I. Gutierrez, B. H. November, R. G. Povey, S. J. Whiteley, D. D. Awschalom, D. I. Schuster, and A. N. Cleland, "Quantum control of surface acoustic-wave phonons," Nature **563**, 661–665 (2018).

[129] Y. Chu, P. Kharel, T. Yoon, L. Frunzio, P. T. Rakich, and R. J. Schoelkopf, "Creation and control of multi-phonon Fock states in a bulk acoustic-wave resonator," Nature **563**, 666–670 (2018).

[130] S. Y. Yu, X. C. Sun, X. Ni, Q. Wang, X. J. Yan, C. He, X. P. Liu, L. Feng, M. H. Lu, and Y. F. Chen, "Surface phononic graphene," Nature Materials **15**, 1243–1247 (2016).

[131] C. He, X. Ni, H. Ge, X.-C. Sun, Y.-B. Chen, M.-H. Lu, X.-P. Liu, and Y.-F. Chen, "Acoustic topological insulator and robust one-way sound transport," Nature Physics **12**, 1124–1129 (2016).

[132] M. Serra-Garcia, V. Peri, R. Süsstrunk, O. R. Bilal, T. Larsen, L. G. Villanueva, and S. D. Huber, "Observation of a phononic quadrupole topological insulator," Nature **555**, 342–345 (2018).

[133] X. Ni, M. Weiner, A. Alù, and A. B. Khanikaev, "Observation of higher-order topological acoustic states protected by generalized chiral symmetry," Nature Materials **18**, 113–120 (2019).

[134] V. Peri, Z.-D. Song, M. Serra-Garcia, P. Engeler, R. Queiroz, X. Huang, W. Deng, Z. Liu, B. A. Bernevig, and S. D. Huber, "Experimental characterization of fragile topology in an acoustic metamaterial," Science **367**, 797–800 (2020).

[135] F. Li, X. Huang, J. Lu, J. Ma, and Z. Liu, "Weyl points and Fermi arcs in a chiral phononic crystal," Nature Physics **14**, 30–34 (2017).

[136] H. He, C. Qiu, L. Ye, X. Cai, X. Fan, M. Ke, F. Zhang, and Z. Liu, "Topological negative refraction of surface acoustic waves in a Weyl phononic crystal," Nature **560**, 61–64 (2018).

[137] B. Xie, H. Liu, H. Cheng, Z. Liu, S. Chen, and J. Tian, "Experimental Realization of Type-II Weyl Points and Fermi Arcs in Phononic Crystal," Physical Review Letters **122**, 104302 (2019).

[138] X. Ni, Z. J. Wong, M. Mrejen, Y. Wang, and X. Zhang, "An ultrathin invisibility skin cloak for visible light," Science **349**, 1310–1314 (2015).

[139] M. A. Bandres, S. Wittek, G. Harari, M. Parto, J. Ren, M. Segev, D. N. Christodoulides, and M. Khajavikhan, "Topological insulator laser: Experiments," Science **359**, eaar4005 (2018).

[140] G. Harari, M. A. Bandres, Y. Lumer, M. C. Rechtsman, Y. D. Chong, M. Khajavikhan, D. N. Christodoulides, and M. Segev, "Topological insulator laser: Theory," Science **359**, eaar4003 (2018).

[141] N. Kaina, F. Lemoult, M. Fink, and G. Lerosey, "Negative refractive index and acoustic superlens from multiple scattering in single negative metamaterials," Nature **525**, 77–81 (2015).

[142] F. D. M. Haldane and S. Raghu, "Possible Realization of Directional Optical Waveguides in Photonic Crystals with Broken Time-Reversal Symmetry," Physical Review Letters **100**, 013904 (2008).

[143] A. B. Khanikaev, S. H. Mousavi, W.-K. Tse, M. Kargarian, A. H. MacDonald, and G. Shvets, "Photonic topological insulators," Nature Materials **12**, 233–239 (2013).

[144] L. Lu, J. D. Joannopoulos, and M. Soljačić, "Topological photonics," Nature Photonics **8**, 821–829 (2014).

[145] H. Ge, M. Yang, C. Ma, M.-H. Lu, Y.-F. Chen, N. Fang, and P. Sheng, "Breaking the barriers: Advances in acoustic functional materials," National Science Review **5**, 159–182 (2018).

[146] C. L. Kane and T. C. Lubensky, "Topological boundary modes in isostatic lattices," Nature Physics **10**, 39–45 (2014).

[147] R. Süsstrunk and S. D. Huber, "Observation of phononic helical edge states in a mechanical topological insulator," Science **349**, 47–50 (2015).

[148] S. D. Huber, "Topological mechanics," Nature Physics **12**, 621–623 (2016).

[149] F. Liu, X. Huang, and C. T. Chan, "Dirac cones at $\vec{k} = 0$ in acoustic crystals and zero refractive index acoustic materials," Applied Physics Letters **100**, 071911 (2012).

[150] Y. Li, Y. Wu, and J. Mei, "Double Dirac cones in phononic crystals," Applied Physics Letters **105**, 014107 (2014).

[151] M. Dubois, C. Shi, X. Zhu, Y. Wang, and X. Zhang, "Observation of acoustic Dirac-like cone and double zero refractive index," Nature Communications **8**, 14871 (2017).

[152] I. Liberal and N. Engheta, "Near-zero refractive index photonics," Nature Photonics **11**, 149–158 (2017).

[153] J. Hao, W. Yan, and M. Qiu, "Super-reflection and cloaking based on zero index metamaterial," Applied Physics Letters **96**, 101109 (2010).

[154] X. Huang, Y. Lai, Z. H. Hang, H. Zheng, and C. T. Chan, "Dirac cones induced by accidental degeneracy in photonic crystals and zero-refractive-index materials," Nature Materials **10**, 582–586 (2011).

[155] S. H. Mousavi, A. B. Khanikaev, and Z. Wang, "Topologically protected elastic waves in phononic metamaterials," Nature Communications **6**, 8682 (2015).

[156] Q. Wei, Y. Tian, S.-Y. Zuo, Y. Cheng, and X.-J. Liu, "Experimental demonstration of topologically protected efficient sound propagation in an acoustic waveguide network," Physical Review B **95**, 094305 (2017).

[157] J. G. Checkelsky, J. Ye, Y. Onose, Y. Iwasa, and Y. Tokura, "Dirac-fermion-mediated ferromagnetism in a topological insulator," Nature Physics **8**, 729–733 (2012).

[158] L. A. Wray, "Topological transistor," Nature Physics **8**, 705 (2012).

[159] J. L. Collins, A. Tadich, W. Wu, L. C. Gomes, J. N. B. Rodrigues, C. Liu, J. Hellerstedt, H. Ryu, S. Tang, S.-K. Mo, S. Adam, S. A. Yang, M. S. Fuhrer, and M. T. Edmonds, "Electric-field-tuned topological phase transition in ultrathin Na_3Bi," Nature **564**, 390–394 (2018).

[160] Z. Wang, Y. Chong, J. D. Joannopoulos, and M. Soljačić, "Observation of unidirectional backscattering-immune topological electromagnetic states," Nature **461**, 772–775 (2009).

[161] R. Fleury, D. L. Sounas, C. F. Sieck, M. R. Haberman, and A. Alu, "Sound Isolation and Giant Linear Nonreciprocity in a Compact Acoustic Circulator," Science **343**, 516–519 (2014).

[162] Z. Yang, F. Gao, X. Shi, X. Lin, Z. Gao, Y. Chong, and B. Zhang, "Topological Acoustics," Physical Review Letters **114**, 114301 (2015).

[163] P. Wang, L. Lu, and K. Bertoldi, "Topological Phononic Crystals with One-Way Elastic Edge Waves," Physical Review Letters **115**, 104302 (2015).

[164] L. M. Nash, D. Kleckner, A. Read, V. Vitelli, A. M. Turner, and W. T. M. Irvine, "Topological mechanics of gyroscopic metamaterials," Proceedings of the National Academy of Sciences **112**, 14495–14500 (2015).

[165] L.-H. Wu and X. Hu, "Scheme for Achieving a Topological Photonic Crystal by Using Dielectric Material," Physical Review Letters **114**, 223901 (2015).

[166] Z. Zhang, Q. Wei, Y. Cheng, T. Zhang, D. Wu, and X. Liu, "Topological Creation of Acoustic Pseudospin Multipoles in a Flow-Free Symmetry-Broken Metamaterial Lattice," Physical Review Letters **118**, 084303 (2017).

[167] Z. Zhang, Y. Tian, Y. Cheng, X. Liu, and J. Christensen, "Experimental verification of acoustic pseudospin multipoles in a symmetry-broken snowflakelike topological insulator," Physical Review B **96**, 241306(R) (2017).

[168] Y. Deng, H. Ge, Y. Tian, M. Lu, and Y. Jing, "Observation of zone folding induced acoustic topological insulators and the role of spin-mixing defects," Physical Review B **96**, 184305 (2017).

[169] Y. Yang, Y. F. Xu, T. Xu, H.-X. Wang, J.-H. Jiang, X. Hu, and Z. H. Hang, "Visualization of a Unidirectional Electromagnetic Waveguide Using Topological Photonic Crystals Made of Dielectric Materials," Physical Review Letters **120**, 217401 (2018).

[170] B.-Z. Xia, T.-T. Liu, G.-L. Huang, H.-Q. Dai, J.-R. Jiao, X.-G. Zang, D.-J. Yu, S.-J. Zheng, and J. Liu, "Topological phononic insulator with robust pseudospin-dependent transport," Physical Review B **96**, 094106 (2017).

[171] K. Sakoda, "Double Dirac cones in triangular-lattice metamaterials," Optics Express **20**, 9925 (2012).

[172] Z.-G. Chen, X. Ni, Y. Wu, C. He, X.-C. Sun, L.-Y. Zheng, M.-H. Lu, and Y.-F. Chen, "Accidental degeneracy of double Dirac cones in a phononic crystal," Scientific Reports **4**, 4613 (2015).

[173] J. Mei, Z. Chen, and Y. Wu, "Pseudo-time-reversal symmetry and topological edge states in two-dimensional acoustic crystals," Scientific Reports **6**, 32752 (2016).

[174] R. Süsstrunk, P. Zimmermann, and S. D. Huber, "Switchable topological phonon channels," New Journal of Physics **19**, 015013 (2017).

[175] Z. Zhang, Y. Tian, Y. Cheng, Q. Wei, X. Liu, and J. Christensen, "Topological Acoustic Delay Line," Physical Review Applied **9**, 034032 (2018).

[176] J.-P. Xia, D. Jia, H.-X. Sun, S.-Q. Yuan, Y. Ge, Q.-R. Si, and X.-J. Liu, "Programmable Coding Acoustic Topological Insulator," Advanced Materials **30**, 1805002 (2018).

[177] See Supplemental Materials at [url] for the design of a rubber waveguide, a thermoacoustic converter, an expandable base plate, and a lower-power logic gate; calculations of two connected switches at different temperatures; and a discussion of materials selection and the robustness of the edge states.

[178] E. Boatti, N. Vasios, and K. Bertoldi, "Origami Metamaterials for Tunable Thermal Expansion," Advanced Materials **29**, 1700360 (2017).

[179] P. A. Oliveira, R. M. B. Silva, G. C. Morais, A. V. Alvarenga, and R. P. B. C. Félix, "Speed of sound as a function of temperature for ultrasonic propagation in soybean oil," Journal of Physics: Conference Series **733**, 012040 (2016).

[180] S.-Y. Yu, X.-C. Sun, X. Ni, Q. Wang, X.-J. Yan, C. He, X.-P. Liu, L. Feng, M.-H. Lu, and Y.-F. Chen, "Surface phononic graphene," Nature Materials **15**, 1243–1247 (2016).

[181] M. Polini, F. Guinea, M. Lewenstein, H. C. Manoharan, and V. Pellegrini, "Artificial honeycomb lattices for electrons, atoms and photons," Nature Nanotechnology **8**, 625 (2013).

[182] P. Ajayan, P. Kim, and K. Banerjee, "Two-dimensional van der Waals materials," Physics Today **69**, 38–44 (2016).

[183] K. S. Novoselov, A. Mishchenko, A. Carvalho, and A. H. Castro Neto, "2D materials and van der Waals heterostructures," Science **353**, 6298 (2016).

[184] A. K. Geim and I. V. Grigorieva, "Van der Waals heterostructures," Nature **499**, 419–425 (2013).

[185] A. Avsar, I. J. Vera-Marun, J. Y. Tan, K. Watanabe, T. Taniguchi, A. H. Castro Neto, and B. Özyilmaz, "Air-stable transport in graphene-contacted, fully encapsulated ultrathin black phosphorus-based field-effect transistors," ACS Nano **9**, 4138–4145 (2015).

[186] X. Wang, Z. Cheng, K. Xu, H. K. Tsang, and J. B. Xu, "High-responsivity graphene/silicon-heterostructure waveguide photodetectors," Nature Photonics **7**, 888–891 (2013).

[187] F. Withers, O. Del Pozo-Zamudio, S. Schwarz, S. Dufferwiel, P. M. Walker, T. Godde, A. P. Rooney, A. Gholinia, C. R. Woods, P. Blake, S. J. Haigh, K. Watanabe, T. Taniguchi, I. L. Aleiner, A. K. Geim, V. I. Fal'ko, A. I. Tartakovskii, and K. S. Novoselov, "WSe_2 light-emitting tunneling transistors with enhanced brightness at room temperature," Nano Letters **15**, 8223–8228 (2015).

[188] Y. Cao, V. Fatemi, A. Demir, S. Fang, S. L. Tomarken, J. Y. Luo, J. D. Sanchez-Yamagishi, K. Watanabe, T. Taniguchi, E. Kaxiras, R. C. Ashoori, and P. Jarillo-Herrero, "Correlated insulator behaviour at half-filling in magic-angle graphene superlattices," Nature **556**, 80–84 (2018).

[189] Y. Cao, V. Fatemi, S. Fang, K. Watanabe, T. Taniguchi, E. Kaxiras, and P. Jarillo-Herrero, "Unconventional superconductivity in magic-angle graphene superlattices," Nature **556**, 43–50 (2018).

[190] E. Kogan and V. U. Nazarov, "Symmetry classification of energy bands in graphene," Phys. Rev. B **85**, 115418 (2012).

[191] D. Torrent and J. Sánchez-Dehesa, "Acoustic analogue of graphene: Observation of Dirac cones in acoustic surface waves," Phys. Rev. Lett. **108**, 174301 (2012).

[192] D. Torrent, D. Mayou, and J. Sánchez-Dehesa, "Elastic analog of graphene: Dirac cones and edge states for flexural waves in thin plates," Physical Review B **87**, 115143 (2013).

[193] J. Lu, C. Qiu, S. Xu, Y. Ye, M. Ke, and Z. Liu, "Dirac cones in two-dimensional artificial crystals for classical waves," Physical Review B **89**, 134302 (2014).

[194] T. Ochiai and M. Onoda, "Photonic analog of graphene model and its extension: Dirac cone, symmetry, and edge states," Physical Review B **80**, 155103 (2009).

[195] T. Kariyado and Y. Hatsugai, "Manipulation of Dirac cones in mechanical graphene," Scientific Reports **5**, 18107 (2016).

[196] T. Y. Chiang, L. Y. Wu, C. N. Tsai, and L. W. Chen, "A multilayered acoustic hyperlens with acoustic metamaterials," Applied Physics A **103**, 355–359 (2011).

[197] X. Wang, J. Xu, J. Ding, C. Zhao, and Z. Huang, "A compact and low-frequency acoustic energy harvester using layered acoustic metamaterials," Smart Materials and Structures **28**, 025035 (2019).

[198] J. Lu, C. Qiu, W. Deng, X. Huang, F. Li, F. Zhang, S. Chen, and Z. Liu, "Valley topological phases in bilayer sonic crystals," Phys. Rev. Lett. **120**, 116802 (2018).

[199] A. V. Rozhkov, A. O. Sboychakov, A. L. Rakhmanov, and F. Nori, "Electronic properties of graphene-based bilayer systems," Physics Reports **648**, 1–104 (2016).

[200] E. McCann and M. Koshino, "The electronic properties of bilayer graphene," Reports on Progress in Physics **76**, 056503 (2013).

[201] P. L. de Andres, R. Ramírez, and J. A. Vergés, "Strong covalent bonding between two graphene layers," Physical Review B **77**, 045403 (2008).

[202] M. Yankowitz, S. Chen, H. Polshyn, Y. Zhang, K. Watanabe, T. Taniguchi, D. Graf, A. F. Young, and C. R. Dean, "Tuning superconductivity in twisted bilayer graphene," Science **363**, 1059–1064 (2019).

[203] S. Carr, S. Fang, P. Jarillo-Herrero, and E. Kaxiras, "Pressure dependence of the magic twist angle in graphene superlattices," Phys. Rev. B **98**, 085144 (2018).

[204] M. M. van Wijk, A. Schuring, M. I. Katsnelson, and A. Fasolino, "Relaxation of moiré patterns for slightly misaligned identical lattices: graphene on graphite," 2D Materials **2**, 034010 (2015).

[205] H. Yoo, R. Engelke, S. Carr, S. Fang, K. Zhang, P. Cazeaux, S. H. Sung, R. Hovden, A. W. Tsen, T. Taniguchi, K. Watanabe, G.-C. Yi, M. Kim, M. Luskin, E. B. Tadmor, E. Kaxiras, and P. Kim, "Atomic and electronic reconstruction at the van der Waals interface in twisted bilayer graphene," Nature Materials **18**, 448–453 (2019).

[206] G. Tarnopolsky, A. J. Kruchkov, and A. Vishwanath, "Origin of magic angles in twisted bilayer graphene," Phys. Rev. Lett. **122**, 106405 (2019).

[207] C. Bao, W. Yao, E. Wang, C. Chen, J. Avila, M. C. Asensio, and S. Zhou, "Stacking-dependent electronic structure of trilayer graphene resolved by nanospot angle-resolved photoemission spectroscopy," Nano Letters **17**, 1564–1568 (2017).

[208] G. H. Lee, Y. J. Yu, C. Lee, C. Dean, K. L. Shepard, P. Kim, and J. Hone, "Electron tunneling through atomically flat and ultrathin hexagonal boron nitride," Applied Physics Letters **99**, 243114 (2011).

[209] Z. Jia, Y. Chen, H. Yang, and L. Wang, "Designing phononic crystals with wide and robust band gaps," Physical Review Applied **9**, 44021 (2018).

[210] S.-J. Liang, B. Cheng, X. Cui, and F. Miao, "Van der Waals Heterostructures for High-Performance Device Applications: Challenges and Opportunities," Advanced Materials **32**, 1903800 (2020).

[211] S. Carr, D. Massatt, S. Fang, P. Cazeaux, M. Luskin, and E. Kaxiras, "Twistronics: Manipulating the electronic properties of two-dimensional layered structures through their twist angle," Physical Review B **95**, 075420 (2017).

[212] E. C. Regan, D. Wang, C. Jin, M. I. Bakti Utama, B. Gao, X. Wei, S. Zhao, W. Zhao, Z. Zhang, K. Yumigeta, M. Blei, J. D. Carlström, K. Watanabe, T. Taniguchi, S. Tongay, M. Crommie, A. Zettl, and F. Wang, "Mott and generalized Wigner crystal states in WSe_2/WS_2 moiré superlattices," Nature **579**, 359–363 (2020).

[213] C. Jin, E. C. Regan, A. Yan, M. Iqbal Bakti Utama, D. Wang, S. Zhao, Y. Qin, S. Yang, Z. Zheng, S. Shi, K. Watanabe, T. Taniguchi, S. Tongay, A. Zettl, and F. Wang, "Observation of moiré excitons in WSe_2/WS_2 heterostructure superlattices," Nature **567**, 76–80 (2019).

[214] K. L. Seyler, P. Rivera, H. Yu, N. P. Wilson, E. L. Ray, D. G. Mandrus, J. Yan, W. Yao, and X. Xu, "Signatures of moiré-trapped valley excitons in $MoSe_2/WSe_2$ heterobilayers," Nature **567**, 66–70 (2019).

[215] K. Tran, G. Moody, F. Wu, X. Lu, J. Choi, K. Kim, A. Rai, D. A. Sanchez, J. Quan, A. Singh, J. Embley, A. Zepeda, M. Campbell, T. Autry, T. Taniguchi, K. Watanabe, N. Lu, S. K. Banerjee, K. L. Silverman, S. Kim, E. Tutuc, L. Yang, A. H. MacDonald, and X. Li, "Evidence for moiré excitons in van der Waals heterostructures," Nature **567**, 71–75 (2019).

[216] G. Chen, A. L. Sharpe, P. Gallagher, I. T. Rosen, E. J. Fox, L. Jiang, B. Lyu, H. Li, K. Watanabe, T. Taniguchi, J. Jung, Z. Shi, D. Goldhaber-Gordon, Y. Zhang, and F. Wang, "Signatures of tunable superconductivity in a trilayer graphene moiré superlattice," Nature **572**, 215–219 (2019).

[217] H. Ge, M. Yang, C. Ma, M.-H. Lu, Y.-F. Chen, N. Fang, and P. Sheng, "Breaking the barriers: Advances in acoustic functional materials," National Science Review **5**, 159–182 (2018).

[218] V. Peri, M. Serra-Garcia, R. Ilan, and S. D. Huber, "Axial-field-induced chiral channels in an acoustic Weyl system," Nature Physics **15**, 357–361 (2019).

[219] M. Rosendo López, F. Peñaranda, J. Christensen, and P. San-Jose, "Flat bands in magic-angle vibrating plates," Phys. Rev. Lett. **125**, 214301 (2020).

[220] Y. Deng, M. Oudich, N. J. Gerard, J. Ji, M. Lu, and Y. Jing, "Magic-angle bilayer phononic graphene," Phys. Rev. B **102**, 180304 (2020).

[221] P. Wang, Y. Zheng, X. Chen, C. Huang, Y. V. Kartashov, L. Torner, V. V. Konotop, and F. Ye, "Localization and delocalization of light in photonic moiré lattices," Nature **577**, 42–46 (2020).

[222] R. Bistritzer and A. H. MacDonald, "Moiré bands in twisted double-layer graphene," Proc. Natl. Acad. Sci. USA **103**, 12233–12237 (2011).

[223] K. H. Matlack, M. Serra-Garcia, A. Palermo, S. D. Huber, and C. Daraio, "Designing perturbative metamaterials from discrete models," Nature Materials **17**, 323–328 (2018).

[224] S. Shallcross, S. Sharma, E. Kandelaki, and O. A. Pankratov, "Electronic structure of turbostratic graphene," Physical Review B **81**, 165105 (2010).

[225] P. Moon and M. Koshino, "Optical Absorption in Twisted Bilayer Graphene," Physical Review B **87**, 205404 (2013).

[226] E. Suárez Morell, J. D. Correa, P. Vargas, M. Pacheco, and Z. Barticevic, "Flat bands in slightly twisted bilayer graphene: Tight-binding calculations," Physical Review B **82**, 121407(R) (2010).

[227] S. Carr, S. Fang, Z. Zhu, and E. Kaxiras, "Exact continuum model for low-energy electronic states of twisted bilayer graphene," Phys. Rev. Research **1**, 013001 (2019).

[228] K. Kim, A. DaSilva, S. Huang, B. Fallahazad, S. Larentis, T. Taniguchi, K. Watanabe, B. J. LeRoy, A. H. MacDonald, and E. Tutuc, "Tunable moiré bands and strong correlations in small-twist-angle bilayer graphene," Proc. Natl. Acad. Sci. USA **114**, 3364–3369 (2017).

[229] L. Xian, D. M. Kennes, N. Tancogne-Dejean, M. Altarelli, and A. Rubio, "Multiflat bands and strong correlations in twisted bilayer boron nitride: Doping-induced correlated insulator and superconductor," Nano Letters **19**, 4934–4940 (2019).

[230] M. H. Naik and M. Jain, "Ultraflatbands and shear solitons in moiré patterns of twisted bilayer transition metal dichalcogenides," Phys. Rev. Lett. **121**, 266401 (2018).

[231] T. Kariyado and A. Vishwanath, "Flat band in twisted bilayer bravais lattices," Phys. Rev. Research **1**, 033076 (2019).

[232] M. Angeli, D. Mandelli, A. Valli, A. Amaricci, M. Capone, E. Tosatti, and M. Fabrizio, "Emergent D_6 symmetry in fully relaxed magic-angle twisted bilayer graphene," Physical Review B **98**, 235137 (2018).

[233] M. Koshino and Y.-W. Son, "Moiré phonons in twisted bilayer graphene," Physical Review B **100**, 075416 (2019).

[234] M. Lamparski, B. Van Troeye, and V. Meunier, "Soliton signature in the phonon spectrum of twisted bilayer graphene," 2D Materials **7**, 025050 (2020).

[235] Z. Zhu, S. Carr, D. Massatt, M. Luskin, and E. Kaxiras, "Twisted trilayer graphene: A precisely tunable platform for correlated electrons," Phys. Rev. Lett. **125**, 116404 (2020).

[236] S. Fang and E. Kaxiras, "Electronic structure theory of weakly interacting bilayers," Phys. Rev. B **93**, 235153 (2016).